Terrestrial Laser Scanner Noise Analysis, Modelling and Detection

Romain Rombourg

Communauté
UNIVERSITÉ Grenoble Alpes

THÈSE

Pour obtenir le grade de

DOCTEUR DE L'UNIVERSITÉ DE GRENOBLE

Spécialité : **Mathématiques et Informatique**

Arrêté ministériel : 25 mai 2016

Présentée par

Romain Rombourg

Thèse dirigée par **Franck Hétroy-Wheeler**
et codirigée par **Eric Casella**

préparée au sein **du Laboratoire Jean Kuntzmann et du Centre for Sustainable Forestry and Climate Change**
et de **l'école doctorale MSTII : Mathématiques, Sciences et Technologies de l'Information, Informatique**

Analyse, modélisation et détection de bruits pour scanners laser terrestres

Terrestrial Laser Scanner Noise Analysis, Modelling and Detection

Thèse soutenue publiquement le **5 Décembre 2019**,
devant le jury composé de :

Monsieur Franck Hétroy
Professeur, Université de Strasbourg, Directeur de thèse

Madame Julie Digne
Chargée de recherche HDR, CNRS Délégation Rhône Auvergne, Rapporteur

Monsieur Florent Lafarge
Chargé de recherche HDR, Inria Centre S. Antipolis - Méditerranée, Rapporteur

Monsieur Frédéric Baret
INRA Centre Provence-Alpes-Côte-d'Azur, Examinateur

Monsieur Edmond Boyer
Inria Centre de Grenoble Rhône-Alpes, Président

Monsieur Eric Casella
Docteur en Sciences, Forest Research, United Kingdom, Co-Directeur de thèse

Remerciements

Avant de démarrer ce manuscrit, j'aimerais adresser mes remerciements à tous ceux sans qui ce travail n'aurais jamais vu le jour. Pour commencer j'aimerais remercier le Laboratoire Jean Kuntzmann, l'Inria et la Forest Research pour l'aide financiaire et matérielle qu'ils m'ont apporté. Ensuite je tiens à remercier mes superviseurs, Franck Hétroy et Eric Casella pour leurs soutient autant scientifique qu'humain. Vous avez fait énormément de choses pour moi, m'octroyer cette chance bien sûr, mais vous m'avez inculqué le goût du traivail et de la recherche bien faite, vous m'avez aussi supporté lorsque je perdais confiance en mon travail et m'avez permis d'aller au bout, merci.

Je tiens aussi à remercier les rapporteurs de mon jury de thèse, Julie Digne et Florent Lafarge, vos rapports étaient clair, et ont soulevés de nombreuses remarques extrêmement pertinentes sur mon travail, je suis donc honoré que ce rôle vous ait été attribué. Je tiens aussi à remercier mes éxaminateurs, Edmond Boyer et Frédéric Baret pour leurs questions d'une grande pertinence. J'adresse aussi un remerciement supplémentaire à Edmond Boyer pour m'avoir acceuilli au sein de l'équipe Morpheo même après le départ de Franck à Strasbourg.

J'aimerais ensuite remercier mes amis, d'abord au sein (ou ex) de l'équipe Morpheo, Vincent, Asnane, Julien, Matthieu, Victoria, Thomas, Mickaël, Claude et toute l'équipe merci vous m'avez bien fait marrer avec vos ânneries (vous remarquerez le ton light, j'édulcore un peu pour une fois) et si je n'ai qu'une seule chose à ajouter ça serait PAYS DE GALLE INDEPENDAAAAANT!!!!

Je veux aussi remercier tous les permanents de l'équipe Morpheo, Jean-Sébastien, Stéphanie et Nathalie. Et Nathalie je te remercie encore pour ton soutient alors que j'avais quitté l'équipe tu m'as vraiment sauvé la mise.

J'adresse ensuite mes remerciements à mes amis, hors de Morpheo, Clémant (dr.Z), Seb, Thonmas, Biche, merci de continuer à me faire marrer même si je me suis fait assez discret ces derniers temps.

Je veux ensuite dire un grand merci à mes parents, Papa, Maman c'est vous qui m'avez porté ici, du début à la fin, j'aurais rien fait sans vous. Je ne le dis surement pas assez mais je suis non seulement très reconnaissant mais aussi extrêmement fier de vous avoir comme parents, je sais que j'ai une chance que peu d'autres ont. Merci à mes grands parents (côté Papa !), si depuis petit j'ai toujours aimé vos bêtises c'est parce que vous êtes les papi et mamie les plus fous qu'on puisse avoir ! Merci à toi aussi mamie (côté Maman), qui nous a quitté pendant ma deuxième année de thèse mais qui continue de veiller sur nous de là-haut, je le sais, tes pâtes bolo et ton gigot servi à la main me manquent mamie, bisous.

J'aimerais aussi remercier la petite boule de poil qui accompagne mon quotidien depuis maintenant 2 ans, Nasky mon chouchou, qui est collé à moi alors que j'écris ces mots. Tu me fatigues tu sais mon chou mais ne change rien c'est comme ça que je t'aime.

Enfin, à celle qui partage ma vie, à celle qui m'a poussé depuis que je la connais à être un homme meilleur, à celle dont le sourire me remonte toujours le moral et dont les pleurs me glacent le sang, à celle qui a donné un sens à ma vie (désordonnée avant que je la connaisse), à celle qui tel un feu d'artifice peut exploser à tout moment, faire un peu peur au chien mais me laisser béa devant sa beauté. À toi ma chérie, merci je t'aime de tout mon coeur et je souhaite terminer mes jours à tes côtés.

Abstract

In this thesis, we focused on several topics related to noise detection in point clouds generated by Terrestrial Laser Scanners (TLS): first, the projection methods to compute an image from a TLS scan; second, the detection of sky noise, i.e. noise produced when a Amplitude Modulated Continuous Wave TLS measures range only from background radiation; and finally, the detection of mixed point noise, i.e. points acquired when the TLS was receiving return signals from several different surfaces. To tackle these challenges, we first analysed how the TLS samples space and deduced properties on how the local point cloud density evolves with respect to the elevation. This allowed us to show the limits of usual noise detection techniques and oriented our focus on 2D non density based detection techniques. We then defined a theoretical framework to analyse projection methods, unavoidable foundations for 2D detection methods. This framework allowed us to bring to light two fundamental properties that should be satisfied by a projection. Following these properties, we designed a projection algorithm that satisfied them as much as possible. We then defined a way to quantify projection quality and compared our proposed algorithm with the most widely used algorithm and showed that this method is not adapted. Our proposed projection on the contrary showed very good results. Since the sky noise has never been studied in previous works, we formally analysed it to build some theoretical foundations for sky detection. The analysis allowed us to show theoretically and experimentally that the range distribution of sky noise is independent of the underlying properties of the background radiation signal. From our projection and the discovered properties, we designed a sky detector and a mixed point detector. The detectors were tested via an extensive validation in controlled conditions. The results showed that our proposed detectors combined with the proposed projection are able to correctly detect almost all presented noise with few bad detection for the sky detectors and a reasonable amount of them for the mixed point detector.

Résumé

Dans cette thèse, nous nous sommes concentrés sur plusieurs sujets liés à la détection du bruit dans les nuages de points générés par les scanners laser terrestres (TLS) : premièrement, les méthodes de projection pour calculer une image à partir d'un balayage TLS ; deuxièmement, la détection du bruit du ciel, c'est-à-dire le bruit produit lorsqu'une mesure d'un TLS à onde continue modulée en amplitude n'est effectuée que sur du rayonnement ambiant ; et enfin, la détection du bruit de points mixtes, c'est-à-dire les points acquis lorsque le TLS reçoit des signaux de retour de plusieurs surfaces différentes. Pour relever ces défis, nous avons d'abord analysé l'échantillonnage de l'espace du TLS et déduit des propriétés sur la densité locale de points en fonction de l'élévation, ce qui nous a permis de montrer les limites des techniques classiques de détection. Nous avons ensuite défini un cadre théorique pour analyser les méthodes de projection, fondements des méthodes de détection 2D. Ce cadre nous a permis de mettre en évidence deux propriétés fondamentales devant être satisfaites par une projection. En se basant sur ces propriétés, nous avons conçu un algorithme de projection les satisfaisant au mieux. Nous avons ensuite défini une quantification de la qualité d'une projection et comparé notre algorithme avec l'algorithme classique et montré que la méthode classique n'est pas adaptée. La projection proposée a quant à elle donné de très bons résultats. Comme le bruit du ciel n'a jamais été étudié dans de précédents travaux, nous l'avons formellement analysé pour construire des bases théoriques pour la détection du ciel. L'analyse nous a permis de montrer théoriquement et expérimentalement que la distribution de distance du bruit de ciel est indépendante des propriétés sous-jacentes du rayonnement ambiant. À partir de notre projection et des propriétés découvertes, nous avons conçu un détecteur de ciel et un détecteur de points mixtes. Les détecteurs ont été testés via une validation approfondie en conditions contrôlées. Les résultats ont montré que nos détecteurs combinés à notre projection sont capables de détecter correctement presque tout le bruit présenté avec peu de mauvaises détections pour le détecteur de ciel et une quantité raisonnable pour le détecteur de point mixte.

Contents

List of Figures

List of Tables

List of Symbols and Acronyms

Hereafter is the list of symbols and notations introduced in the specified chapters.

General notations

Symbol	Meaning
rad	radians
$^{\circ}$	degrees
π	Ratio of a circle perimeter by its diameter
τ	Ratio of a circle perimeter by its radius ($\tau = 2\pi$)
c	speed of light in a vacuum

Chapter 2

Symbol	Meaning
R	Range
θ	Elevation
φ	Azimuth
I	Intensity
δ	Angular resolution
D	Density augmentation factor
D^*	Limit density augmentation factor
Err	Relative error between D and D^*
sinc	Cardinal sine function, defined as $\mathrm{sinc}(x) = \frac{\sin(x)}{x}$

Chapter 4

Symbol	Meaning
T	Equirectagular projection function
S	Point set acquired from aTLS scan
G	2D grid
P	3D point
p	Pixel
P_i	i^{th} point acquired in a scan
R_i	Range of the i^{th} point acquired in a scan
θ_i	Elevation of the i^{th} point acquired in a scan
φ_i	Azimuth of the i^{th} point acquired in a scan
I_i	Intensity of the i^{th} point acquired in a scan
u	Line coordinate of a pixel
v	Column coordinate of a pixel
t_k	Set of points acquired during the k^{th} eye turn
$R_{threshold}$	Range threshold parameter for the projection algorithm
N_{map}	Number of points in a produced map
N_{scan}	Number of points in a scan
ρ_l	Lossless coefficient
$W_n(p)$	n by n neighbourhood of a pixel p
ρ_c	Coherence coefficient
$\|X\|$	Number of points in the set X

Chapter 5

Symbol	Meaning
λ_{mi}	i^{th} modulation wavelength
ϕ_i	Phase measured with the i^{th} modulation wavelength
n_i	i^{th} phase unwrapping number
$\lfloor x \rfloor$	Closest integer inferior to x
$s(t)$	Sent signal by the TLS
$r(t)$	Received signal by the TLS
$C(x)$	Cross correlation of the sent and received signal
f_X	Probability density function for the random variable X
$E[X]$	Expected value of the random variable X
$\mathrm{var}\,[X]$	Variance of the random variable X
$\mathcal{U}(a, b)$	Uniformly distributed random variable between a and b
ρ_{sky}	Sky coefficient parameter for the sky detection algorithm
$\wedge$	Vector cross product
$\|X\|$	Norm of the vector X
$\beta_{threshold}$	Limit angle parameter for the mixed point detection algorithm
W	Window size parameter for the sky or mixed point detection algorithm

Chapter 6

Symbol	Meaning
w_{exit}	Laser beam radius at the exit of the scanner
w_0	Laser beam radius at the beam waist
R_{w_0}	Distance between the scanner exit and the beam waist
w	Laser beam radius
λ	Light wavelength
X^T	Transpose of the matrix X
$X^\dagger$	Pseudo-inverse of the matrix X
ψ	Unconstrained angular edge loss
ψ_θ	Zenithal angular edge loss
ψ_φ	Azimuthal angular edge loss
δ_φ	Corrected azimuthal resolution
L	Edge loss
TP	Number of true positives
TN	Number of true negatives
FP	Number of false positives
FN	Number of false negatives
tpr	True positive ratio
fpr	False positive ratio
$\overline{tpr}$	Mean true positive ratio
$\overline{fpr}$	Mean false positive ratio

Hereafter the list of acronyms used in this thesis.

Acronym	Meaning
LiDAR	Light Detection And Ranging
tLiDAR	terrestrial Light Detection And Ranging
TLS	Terrestrial Laser Scanner
2D	Two dimensional
3D	Three dimensional
BIM	Building Information Modelling
DTM	Digital Terrain Model
AMCW	Amplitude Modulated Continuous Wave
TOF	Time Of Flight
PCA	Principal Component Analysis
TIN	Triangular Irregular Network
r.v	random variable
ROC	Receiver Operating Characteristic
RMSE	Root Mean Square Error

Chapter 1

Introduction

Contents

1.1 The TLS, an essential tool

The laser scanning tools have been gaining much acceptance in the past decade. The terrestrial laser scanner (TLS) is a tool allowing to take a 3D snapshot of a scene in minutes. It found an essential place in many fields of applications. Some TLS applications are compiled in Table 1.1.

Research field	TLS application	Works
Building surveys	BIM	Bosché et al. [2015], Mukupa et al. [2017]
Civil surveys	Road quality assessment	El-Ashmawy [2016]
Forensics	Crime scene modellisation	Topol et al. [2008]
Archaeology	Site modellisation	Lerma et al. [2010]
Environmental surveys	DTM generation	Jaboyedoff et al. [2012]
Forest management	Tree modelling	Dassot et al. [2011], Liang et al. [2016]

Table 1.1 – Examples of TLS applications

The TLS most popular use is in building surveys where it allows state of the art size measurement as well as fast and accurate BIM (Building Information Modelling) (Bosché et al. [2015], Mukupa et al. [2017], example given Figure 1.1). In the domain of civil surveys, TLS was also used for road quality assessment where it outperformed other road-mapping methods as shown by El-Ashmawy [2016]. Laser scanners also found an interesting use in forensics (Topol et al. [2008]) where their precision, sampling capacities and fundamentally remote sensing abilities have proven to be a great help in crime scene modelling.

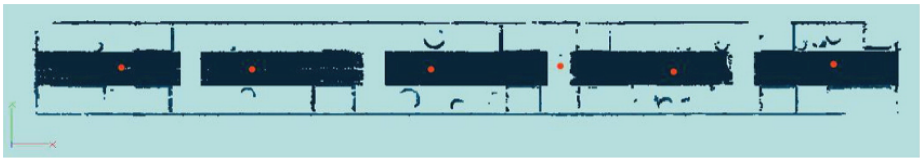

Figure 1.1 – Example of a building TLS scan (source Bosché et al. [2015])

In archaeological studies and archaeological preservation, TLS was used to model important or fragile sites for further study or conservation, e.g. the Palaeolithic caves of Parpalló Lerma et al. [2010] (Figure 1.2). Another domain affected by TLS is the study of natural disasters such as floods, avalanches or landslides, namely environmental surveys. As shown by Jaboyedoff et al. [2012], if precision is the main concern, TLS is often the best solution for DTM (Digital Terrain Model) generation.

Figure 1.2 – Merged TLS scans of the Parpalló caves (source Lerma et al. [2010])

Finally, in forest management, TLS proved to yield stunning results compared to other methods (Example given Figure 1.3. Dassot et al. [2011] and Liang et al. [2016] compiled the TLS main applications in forestry. These applications include tree volume and biomass estimations, gap fraction estimation, wood quality assessment and phenotyping for small crops.

The TLS is a formidable and versatile tool, and we are still discovering new uses. TLS allows never achieved precision, or even previously im-

(a) Before reconstruction (b) After reconstruction

Figure 1.3 – Example of a topologically consistent tree structure derived from TLS point cloud data. This example is given for a ca. 19 m tall and 5 m3 oak tree before (Left) and after (Right) its surface reconstruction. (source Casella, Rombourg et al. [2019], unpublished data).

possible or impractical measurement of some data such as tree leaf area distribution (Béland et al. [2011]).

1.2 TLS advantages and limitations

Most TLS applications exploit its ability to directly output a 3D representation of the scene along with its precision and dense sampling capacities. Also, being an active acquisition method, its output is much more robust to scene illumination conditions than passive methods (e.g. photogrammetry). Obviously all these advantages come with some limitations. For example the TLS takes a few minutes to scan the scene, meaning that any moving target will create incoherent series of points (e.g. moving tree branches due to wind or a car moving in the street). As pointed out by Lafarge [2015], noise and outlier removal is a common and crucial problem for any point cloud based procedure like 3D modelling of urban scenes or tree modelling. In TLS acquired point clouds, outliers

(hereafter called noise since we will not be interested in the surface noise problematic in this thesis) can be produced by several physical processes and we will focus on the two main causes.

The mixed point challenge

A renown and important problem are the mixed points or mixed pixels. They occur at the edge of every object visible from the TLS point of view. They are caused by the fact that the laser beam used to acquire the distance measurements is not a perfect mathematical line (thus with no volume or surface). This implies that, when the laser is partially projected on two or more surfaces, their measurement will get mixed resulting in a point that does not have any physical reality. This noise can take several forms depending on the acquisition technology and the properties of the surfaces that created it. On top of creating noisy points, this phenomenon creates an edge loss, meaning a zone on the edge of every object where points are uncertain. Filtering the uncertain points leads to a loss in the object dimensions, the aforementioned edge loss. In modelling applications the noisy points lead to erroneous models and in measuring applications edge loss drastically reduces the possible precision. Thats why the detection of mixed points have been of great interest in the literature. According to Huber et al. [2010], this problem is still not properly solved.

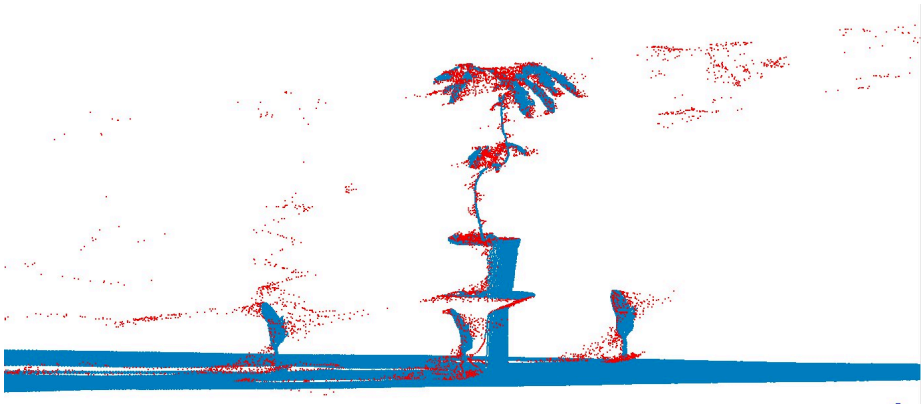

Figure 1.4 – Example of mixed point noise, in blue the valid points, in red the mixed points

The sky point problem

Mixed points are not the only type of noisy points that can be found in a TLS scan. Another noise, in this document called sky points, arises in scans taken with the AMCW (Amplitude Modulated Continuous Wave) technology. This technology, the fastest, most precise and cheapest, cannot easily differentiate a real laser return from a lost return (e.g. laser shot towards the sky or a surface very far away). This leads to random points whenever the scanner does not get a return. Sky points are poorly detected by commercial software. Although the remaining spurious points can be easily detected, this inconstant procedure leads to irregular edge loss, impairing applications like gap fraction estimation in forestry.

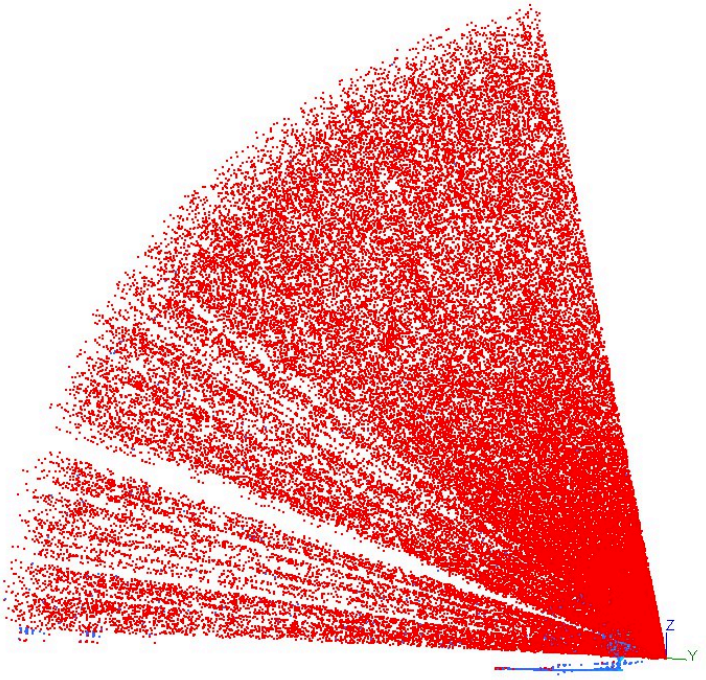

Figure 1.5 – Example of sky noise, in blue the valid points, in red the sky points

A fragile base : the equirectangular projection

Most state of the art noise filters rely on a projection of the 3D scan onto a 2D image (Cai et al. [2005], Tang et al. [2007], Cifuentes et al. [2014],

Eysn et al. [2013] etc ...). This approach, is also used in the literature for other applications (Houshiar et al. [2013], Houshiar and Nüchter [2015], Käshammer and Nüchter [2015] etc ...). Since equirectangular mapping uses scanning directions to compute image positions, the sampling precision will have a direct impact on this class of methods. Unfortunately, sampling directions are affected by a jitter type noise (sampling time errors) and numerical instabilities brought by the spherical change of coordinates. These errors makes the output of a classic equirectangular projection inconsistent. Especially, as Käshammer and Nüchter [2015] noted, errors can induce point losses and displacement in the resulting image. The displacement themselves lead to erroneous computation for any method based on local neighbourhood analysis.

Contributions

In this thesis we tackle the equirectangular projection problem, the detection of sky point and mixed points.

On the equirectangular projection we propose a new algorithm for equirectangular mapping of TLS scans able to deal with the sampling anomalies. To do so the formalism of equirectangular projection is investigated and adapted for spherical TLS scanning. Generated maps by our algorithm are compared with those generated by the mainly used projection algorithm (as defined by Marinus of Tyre in 100 A.C). The mapping quality is analysed using two properties that we formally define : the point loss as a result of the projection and the neighbourhood coherence, indicating the correctness of a local neighborhood.

To tackle the sky noise detection problem we analyse the physical phenomenon producing it. The analysis allows us to find a core property of the sky noise. The property is theoretically and experimentally proved. Based on the newly defined equirectangular projection methods we develop two new independent noise detection methods. The first is aimed at detecting sky noise only. Thanks to the found sky property we designe it to be robust against differences in sky illumination conditions between scans. It is also made configurable to have optimal performances for all albedos. The second is designed for mixed point filtering.

These filters are backed with an analysis on the filter edge loss and its capacity to correctly label noise points in controlled conditions, mimicking forestry and civil applications. Reference point cloud labelling is done

without expert intervention and using a newly and presented edge loss model taking into account the real shape of the beam and the discrete nature of TLS sampling.

1.3 Outline of the thesis

We give in this section the outline of the thesis. In chapter 2 we will present the background theory needed for this study. This includes the TLS measurement principles and an analysis of TLS point cloud density.

We then present 3 a literature review of TLS noise filtering techniques and equirectangular image projections.

After this, in chapter 4 we will formally define the equirectangular projection for discrete point clouds. This formalism will then be adapted for LiDAR acquired data and, based on this formalism, a new equirectangular projection algorithm was derived to satisfy two fundamental properties introduced in the formalism : the lossless property (as few point as possible should be lost due to the projection algorithm) and the coherence property (local visual neighbourhood should be conserved in the projection). Finally the proposed algorithm was evaluated against the classical projection method using two new metric based on the lossless and coherence properties.

In chapter 5 will be presented two new filtering methods using the projection algorithm presented in chapter 4. The first will be aimed at detecting sky points. The proposed method was designed to be robust against changes in sky illumination changes from scan to scan. The aim of this filter is to capture sky point while leaving the mixed points undetected. Secondly we will introduce a new mixed point filtering scheme, the filter was designed to be plastic in term of its trade-off between resolution power (smallest object it can resolve) and filtering consistency (capacity to correctly recognise all noise). Based on the problems raised in 4 the equations it uses were made insensitive to azimuth coordinates drift near the scanning poles.

Then in chapter 6 we will present the experimental procedure used for filter evaluation in controlled conditions. We first present the general procedure and material used for the experiments. Then we devise a framework for reference noise-labelled point cloud creation where the focus is

to have an automated, model based, reference labelling and avoid expert based modelling (in an attempt to be as objective as possible). In this framework we first semi automatically reconstructed the scanned objects in every scan, then, based on a new edge loss model, we automatically labelled the point clouds. The results using the filters proposed in chapter 5 and the previously defined experimental framework are then presented and discussed.

We finish in Chapter 7 by presenting a summary of our contributions, an analysis of the limitations of this works and we open some perspectives and possible future works. Part of this work has been presented in the International Conference on Functional-Structural Plant Growth Modeling, Simulation, Visualization and Applications (Qingdao, China, 2016) and the "6^{ieme} édition de l'atelier T-LiDAR pour la communauté francophone" workshop (Avignon, France, 2016). More details can be found in Appendix B

Chapter 2

Terrestrial Laser Scanners : scanning principles

Contents

In this chapter we will present the theoretical concepts surrounding laser scanning and Terrestrial laser scanners. We also present here a detailed analysis of the sampling pattern used by Terrestrial laser scanner and its properties.

2.1 Distance measurement

The TLS is part of the laser scanning technologies. Laser scanning sensors send a laser towards the target and analyse the reflected light to measure the distance between the sensor and the target. We will now review the three main distance measurement technologies used in laser scanning.

Triangulation

Triangulation based distance measurement uses the offset between the emitting source (the laser) and the receiving device (usually an optical position sensor) to determine the distance to the object. As seen in figure 2.1, knowing the offset between the laser and the detector and the distance between the lens and the detector (which are all chosen during the conception, thus known), the distance to the object is proportional to the dot position on the detector. Although very precise, this technology only allows for short distance measurement due to its measurement principle.

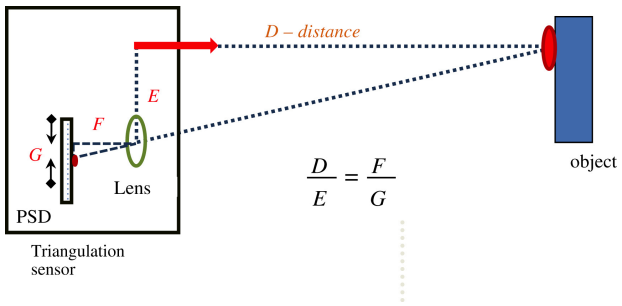

Figure 2.1 – Triangulation LiDAR principle

Pulse based

Pulse based distance measurement, is part of the TOF (Time Of Flight) methods. It uses the time needed for the light to go from the laser source to

the object, then back to the detector. As their name suggests, pulse based LiDAR emits a short duration pulse (in the tenth of nanoseconds), records the exact time of emission $t_{emission}$. When an energy peak is recorded on the sensor (normally caused by the laser being reflected and captured by the sensor), the exact time $t_{reception}$ is recorded and the range (or distance) R is computed by :

$$R = c(t_{reception} - t_{emission}) \tag{2.1}$$

where c is the speed of light in the air ($299,710,559\ m/s$ at $1550\ nm$ or $299,709,708\ m/s$ at $670\ nm$).

To achieve millimeter precision, the time circuits need to have a precision of 10ps or less, making these LiDAR expensive and limited in precision. However this measurement principle allows for the highest maximum distance measurement (which is only limited by the time the LiDAR waits for a return and the energy of the emitted pulse). For better precision scanners using this technology make several measurement, making them slow in comparison to the others.

Phase-shift based

Phase based (or AMCW, Amplitude Modulated Continuous Wave) sensors illuminate the object with a continuous light wave modulated in amplitude. The phase shift between the outgoing and incoming waves is then proportional to the light time of flight. Range is obtained by :

$$R = \frac{\lambda_m}{2}\frac{\Delta\phi}{\tau} \tag{2.2}$$

where $\lambda_m = c/f_m$ is the modulation wavelength, f_m, the modulation frequency and $\Delta\phi$ the phase shift between the outgoing and the incoming waves.

Measurement precision is then entirely defined by the modulation wavelength and the phase measurement precision. Since phase measures are very precise, precision is usually limited by λ_m. Modulation wavelength also determines the maximum measurable distance R_{max} due to the ambiguity on the phase :

$$R_{max} = \frac{\lambda_m}{2} \tag{2.3}$$

To augment the maximum measurable distance, phase shift lidars commonly use 3 or more modulation wavelengths were, the longer wavelengths solve the ambiguity on the shortest, allowing reasonable maximum distances and good precision. The phase measurement being very fast, phase shift LiDAR are the fastest on the market.

2.2 Sampling principle

Several sampling techniques can be found among the different laser scanners. Diffenrent sampling techniques will produce different point cloud properties. The sampling can be manual, planar, or spherical. We will focus here on the most common sampling paradigm among the Terrestrial laser scanners, the spherical sampling.

Sampling description

A TLS is a stationary scanner that samples distances in every direction in the scene from its point of view. Even if it can be mounted on a mobile platform (e.g. car, drone) the works in this thesis are limited to static TLS. To efficiently sample the scene most scanners use a rotating mirror mounted on a rotating head to deflect a pulsed or continuous laser beam in every direction (figure 2.2), it is this sampling that we call a spherical sampling.

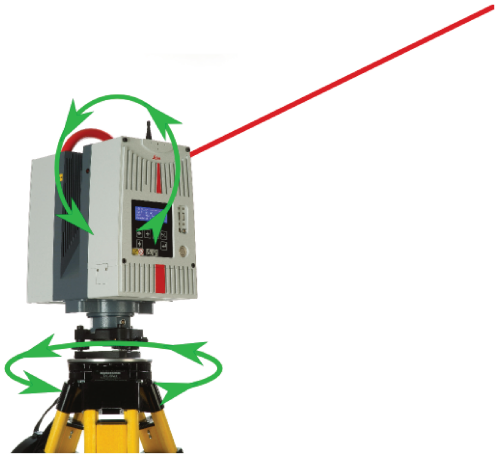

Figure 2.2 – TLS sampling principle, in green the rotation of the azimuthal and zenithal motors

The reflected laser beam from a hit is then used to compute the distance to the nearest object in a given direction. We will call the rotating mirror the eye of the scanner and the rotating head the head of the scanner (figure 2.3).

Figure 2.3 – Scanner description

To digitise a scene into a point cloud a scanner has the laser swipe through the scene using its rotating mirror. It takes a distance measurement at every fixed angular step, we call this step the angular resolution δ. After each turn of the rotating mirror the scanner head turns by a fixed amount (usually δ). Considering the sampling pattern it is more natural to express the point coordinates in a spherical basis. Well then use the spherical coordinate system associated with the Cartesian basis $(O, \vec{ex}, \vec{ey}, \vec{ez})$ to express point coordinates. O is the coordinate system origin, here the eye of the scanner, $\vec{ex}$ (resp. $\vec{ey}$, $\vec{ez}$) is the vector pointing in the x (resp. y, z). The spherical coordinate system describes a point P with a triplet : (R, θ, φ) with R the range, the distance $\left\|\overrightarrow{OP}\right\|$; θ, the elevation, the angle between the xy-plane and $\overrightarrow{OP}$; φ, the azimuth, the angle between the projection of $\overrightarrow{OP}$ on the xy-plane and the x-axis (see figure 2.4)

Spherical coordinates are computed by :

$$R = \sqrt{x^2 + y^2 + z^2} \tag{2.4}$$

$$\theta = \arctan\left(\frac{z}{\sqrt{x^2 + y^2}}\right) \tag{2.5}$$

$$\varphi = \text{atan2}(y, x) \tag{2.6}$$

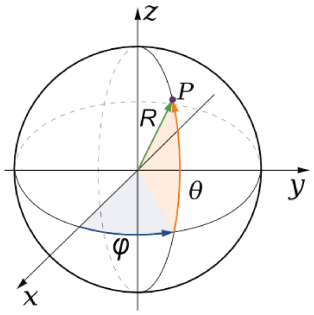

Figure 2.4 – Spherical coordinate system

Spherical sampling analysis

This spherical sampling pattern implies a non uniform point density with the minimal density at the horizon ($\theta = 0$) and maximal at the zenith ($\theta = +\frac{\tau}{4}$) and nadir ($\theta = -\frac{\tau}{4}$)

Although often considered to be a problem, this non uniform density is a real advantage in modelling applications where small elements are positioned in the high density regions (e.g. branches and leaves in tree modelling, stalactites in cave modelling, architectural details in historical building conservation ...). To assess the density change first consider a cone with an aperture angle α and an axis defined by $\overrightarrow{OP}$, $P = (R, \theta, \varphi)$. For small enough α we can prove (the proofs are given in Appendix A.1) that the *density augmentation factor* $D(\delta, \theta)$ i.e. the factor by which the number of points at the horizon is multiplied at an elevation θ for a resolution δ is given by :

$$D(\delta, \theta) = \frac{\delta}{\arccos\left(\cos(\delta)\cos(\theta)^2 + \sin(\theta)^2\right)} \tag{2.7}$$

For small enough δ, $D(\delta, \theta)$ is well approximated by $D^*(\theta)$

$$D^*(\theta) = \frac{1}{\cos(\theta)} \tag{2.8}$$

Let $Err(\delta, \theta)$ be the relative error between $D(\delta, \theta)$ and $D^*(\theta)$:

$$Err(\delta, \theta) = \frac{D(\delta, \theta) - D^*(\theta)}{D(\delta, \theta)} \tag{2.9}$$

We prove in Appendix A.1 that :

Theorem 1. ***Density bounds theorem***

$$\forall \delta \in \left[0, \frac{\tau}{2}\right], \forall \theta,\ D^*(\theta) \leq D(\delta, \theta) \leq \frac{D^*(\theta)}{\mathrm{sinc}\left(\frac{\delta}{2}\right)}$$

Theorem 2. ***Density approximation theorem***

$$\forall \varepsilon > 0, \exists \delta_{lim} \geq \sqrt{24\varepsilon}\ s.t.\ \forall \delta \leq \delta_{lim}, \forall \theta, Err(\delta, \theta) \leq \varepsilon$$

As shown in table 2.1 density augmentation is negligible for $0 \leq \theta \leq \frac{2\tau}{36}$. Rises above 1.1 ($10\%$ augmentation) for $\theta > \frac{3\tau}{36}$ and above 2 (100% augmentation) for $\theta > \frac{6\tau}{36}$.

For resolutions under $\frac{\tau}{100}$, i.e. more than 100 points per turn, the relative error between $D(\delta, \theta)$ and $D^*(\theta)$ is inferior to $1.6\ 10^{-4}$. The error is even more negligible for usual resolution values. For resolutions of more than 10000 points per turn, the maximal error is in the 10^{-8} order thus fully negligible.

$\theta(rad)$	$\theta(°)$	$D^*(\theta)$
0	0	1
$\frac{\tau}{36}$	10	1.02
$\frac{2\tau}{36}$	20	1.06
$\frac{3\tau}{36}$	30	1.15
$\frac{4\tau}{36}$	40	1.31
$\frac{5\tau}{36}$	50	1.56
$\frac{6\tau}{36}$	60	2
$\frac{7\tau}{36}$	70	2.92
$\frac{8\tau}{36}$	80	5.76
$\frac{\tau}{4}$	90	∞

Table 2.1 – Density augmentation factor values for different elevations

$\delta(rad)$	$\delta(^\circ)$	Points per turn	$\max_\theta(Err(\delta,\theta))$
$\frac{\tau}{40000}$	0.009	40000	10^{-9}
$\frac{\tau}{20000}$	0.018	20000	$4.1\ 10^{-9}$
$\frac{\tau}{10000}$	0.036	10000	$1.6\ 10^{-8}$
$\frac{\tau}{5000}$	0.072	5000	$6.6\ 10^{-8}$
$\frac{\tau}{1000}$	0.36	1000	$1.6\ 10^{-6}$
$\frac{\tau}{100}$	3.6	100	$1.6\ 10^{-4}$

Table 2.2 – Relative error values for different resolutions

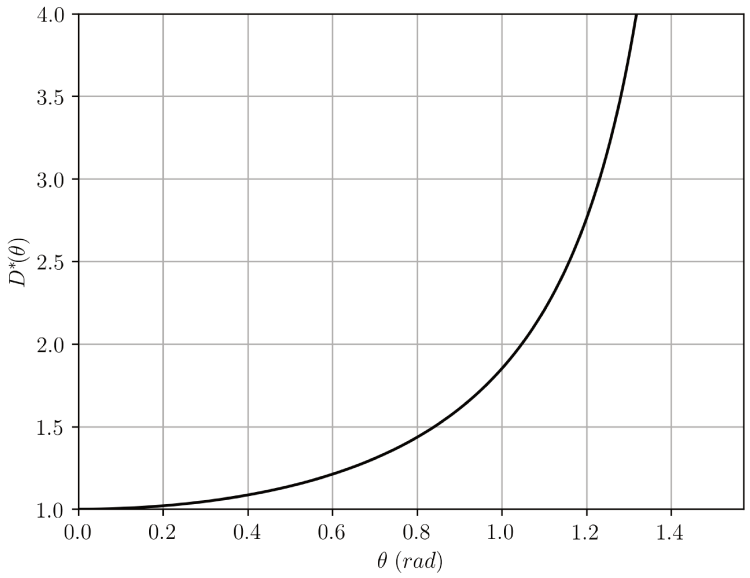

Figure 2.5 – Limit Density augmentation factor D^* for $\theta \in \left[0, \frac{\tau}{4}\right]$.

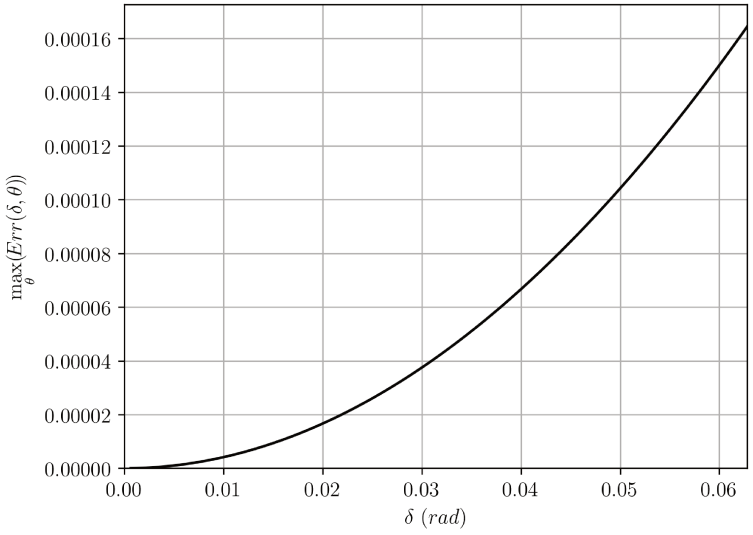

Figure 2.6 – Relative error between $D(\delta, \theta)$ and $D^*(\theta)$ for $\delta \in \left[0, \frac{\tau}{100}\right]$.

2.3 Laser beam and edge loss model

Laser beam model

A laser beam is a spatially coherent (i.e it does not destructively interfere with itself) electromagnetic wave, usually almost monochromatic (with a very narrow spectrum), emitted by a laser device. This wave has the property to have a small focus and a small divergence. The Helmholtz equations in paraxial approximation yields that the intensity as a function of the distance along the beam axis and the radial distance from the beam axis is described by Equation (2.10) (see e.g. Milonni and Eberly [2010]) :

$$I(r,R) = I_0\left(\frac{w_0}{w(R)}\right)\exp\left(-2\frac{r^2}{w(R)^2}\right) \tag{2.10}$$

$$w(R) = w_0\sqrt{1+\left(\frac{\lambda\left(R-R_{w_0}\right)}{\pi {w_0}^2}\right)^2} \tag{2.11}$$

with :

- I the laser intensity (Watt/m^2)
- r the radial distance from the beam axis (m)
- R the axial distance from the laser exit (m)
- λ the light wavelength (m)
- R_{w_0} the axial distance where the beam is at maximum focus
- w_0 radial distance at which the intensity drop under $1/e^2$ at $R = R_{w_0}$
- I_0 the maximum beam intensity (at $R = R_{w_0}$ and $r = 0$)

The Equation (2.10) shows that the intensity profile along a beam diameter in a plane perpendicular to the beam direction of propagation at a distance R will follow a Gaussian g :

$$g(r) = A\exp\left(-2\frac{r^2}{w(R)^2}\right) \tag{2.12}$$

where A is the maximum intensity along the diameter. An example of an intensity profile is given figure 2.7.

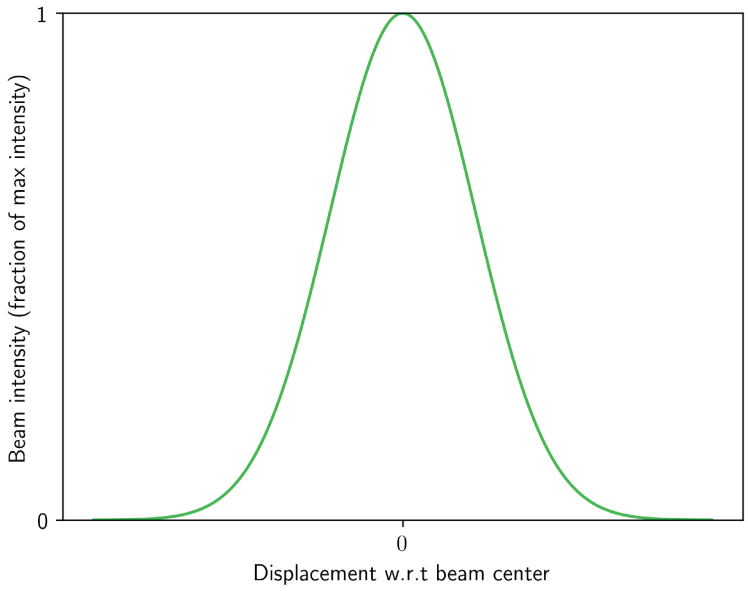

Figure 2.7 – Example of a Gaussian intensity profile

Beam diameter definitions

We defined in the previous section how a Gaussian beam intensity evolves as the beam propagates through space. As shown in Equation (2.12) at any distance the laser beam has a Gaussian intensity profile which never attains zero. Since a laser does not have a proper edge (i.e. a position where no power is received from the laser) conventions were created to define a laser radius.

$1/e^2$ convention

The most classic convention and most used in research is the $1/e^2$ convention. The convention defines the beam radius as the distance between the beam axis and the radial position were the intensity falls under Ae^{-2} where A is the maximum intensity along the diameter and e Euler's number. We can derive from Equation (2.12) the expression of the beam radius $w_{1/e^2}(R)$ as a function of the distance to the source R :

$$w_{1/e^2}(R) = w_0 \sqrt{1 + \left(\frac{\lambda \left(R - R_{w_0} \right)}{\pi {w_0}^2} \right)^2} \tag{2.13}$$

$1/e$ convention

This convention is similar to the $1/e^2$ convention except that the beam radius is defined as the distance between the beam axis and the radial position were the intensity falls under Ae^{-1} where A is the maximum intensity along the diameter. Deriving its expression from Equation (2.12) yields :

$$w_{1/e}(R) = \frac{\sqrt{2}w_0}{2}\sqrt{1+\left(\frac{\lambda\left(R-R_{w_0}\right)}{\pi {w_0}^2}\right)^2} \tag{2.14}$$

FWHM convention

The FWHM convention stands for Full Width at Half Maximum convention. As its name states, the beam radius is defined as the distance between the beam axis and the radial position were the intensity falls under $\frac{A}{2}$ where A is the maximum intensity along the diameter. Deriving its expression from Equation (2.12) yields :

$$w_{FWHM}(R) = \sqrt{\frac{\ln 2}{2}}w_0\sqrt{1+\left(\frac{\lambda\left(R-R_{w_0}\right)}{\pi {w_0}^2}\right)^2} \tag{2.15}$$

where $\ln(x)$ denotes the natural logarithm of x.

Other conventions exists, especially for non gaussian beams, but we will focus on the three presented here. Also, if not specified, the $1/e^2$ convention is used in this document.

The conversions from the $1/e$ and the FWHM to the $1/e^2$ conventions are given Equations (2.16) and (2.17) :

$$w_{1/e^2}(R) = \sqrt{2}\, w_{1/e}(R) \tag{2.16}$$

$$w_{1/e^2}(R) = \sqrt{\frac{2}{\ln 2}}\, w_{FWHM}(R) \tag{2.17}$$

Figure 2.8 shows how the different conventions are defined with respect to the gaussian intensity profile.

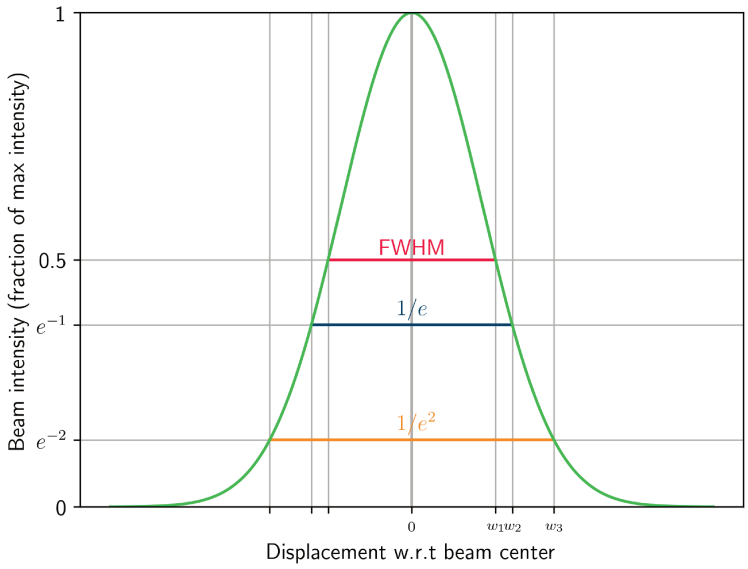

Figure 2.8 – Beam diameter definitions based on the gaussian beam. In green is the intensity profile along a beam diameter at an arbitrary distance. In red blue and yellow the different diameter conventions.

Beam divergence definition

The beam divergence is defined from the property of the beam diameter when $R \gg R_{w_0}$. As R grows the beam diameter tends to grow linearly. Indeed Equation (2.13) shows that :

$$R \gg R_{w_0} + \frac{\pi {w_0}^2}{\lambda} \implies w(R) \approx \frac{\lambda}{\pi w_0} R \tag{2.18}$$

That linear behaviour can be interpreted as the beam being an equivalent cone with an apex on the beam axis at $R = R_{w_0}$ and aperture angle θ with :

$$\theta = \arctan\left(\frac{\lambda}{\pi w_0}\right) \tag{2.19}$$

The beam divergence Θ is finally defined as the total cone angle, i.e. $\Theta = 2\theta$. Since the beam divergence definition is based on the beam diameter, it is influenced by the diameter convention. The following conversion formulae can be used :

$$\Theta_{1/e^2} = \sqrt{2}\,\Theta_{1/e} \tag{2.20}$$

$$\Theta_{1/e^2} = \sqrt{\frac{2}{\ln 2}}\,\Theta_{FWHM} \tag{2.21}$$

Footprint models

To derive a footprint model, i.e. using the gaussian beam model, one must estimate the beam parameters λ, w_0 and R_{w_0}. In TLS datasheets, these information are unfortunately rarely available. As an example we will now derive the footprint models for 3 TLS of 3 different TLS brands :

- Leica P-50 (Leica Geosystems)
- FARO Focus S350 (FARO Technologies Inc.)
- RIEGL VZ-400i (RIEGL Laser Measurement Systems)

In the manufacturers datasheets (Leica Geosystems, FARO Technologies Inc., RIEGL Laser Measurement Systems) three parameters are usually provided, the wavelength λ, the beam diameter at exit $w(0)$, the beam divergence Θ and the beam diameter convention. The given parameters are summed up in Table 2.3.

	Leica P-50	FARO FOCUS S350	RIEGL VZ-400i
Wavelength λ (nm)	1550	1550	1550
Announced divergence (mrad)	0.23	0.3	0.35
Announced beam diameter at exit (mm)	3.5	2.12	7
Used convention for beam diameter	FWHM	$1/e$	$1/e^2$

Table 2.3 – Provided laser parameters in datasheets for the Leica P-50, the FARO FOCUS S350 and the RIEGL VZ-400i

The given parameters must then be converted to the $1/e^2$ convention and the waist size w_0 and the focus distance R_{w_0} can be computed using Equations (2.22) and (2.23).

$$w_0 = \frac{\lambda}{\pi \tan(\Theta)} \tag{2.22}$$

$$R_{w_0} = \frac{1}{\tan(\Theta)} \sqrt{w(0)^2 - {w_0}^2} \tag{2.23}$$

We give Table 2.4 the computed parameters. One must note that the values given by FARO are impossible for a real beam, indeed the beam diameter given is too small for the given divergence. The smallest possible diameter was then taken as the beam diameter at exit.

	LEICA P-50	FARO Focus S350	Riegl VZ-400i
Wavelength (nm)	1550	1550	1550
Announced divergence (mrad)	0.23	0.3	0.35
Announced beam diameter at exit (mm)	3.5	2.12	7
Used convention for beam width	FWHM	$1/e$	$1/e^2$
$1/e^2$ divergence (mrad)	0.39	0.42	0.35
$1/e^2$ beam diameter at exit (mm)	5.94	3^*	7
Computed $1/e^2$ waist size (mm)	5.05	4.65	5.63
Computed focus distance (m)	8	0^*	11.8

Table 2.4 – Provided and computed laser parameters in datasheets for the Leica P-50, the FARO FOCUS S350 and the RIEGL VZ-400i. The * marked value are values incompatible with a real laser, i.e. this case the given diameter is too small for the given divergence. We then took the smallest compatible value.

Using the computed parameters we give Figure 2.9 the beam profiles.

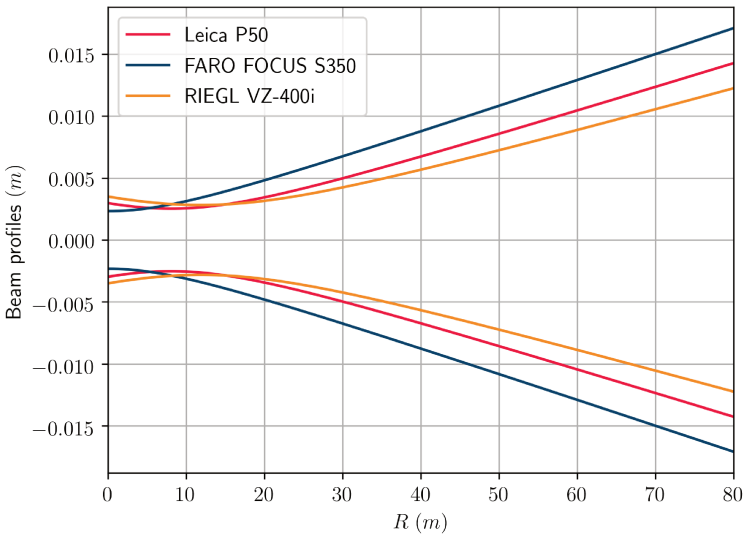

Figure 2.9 – Computed beam profiles for the Leica P50, FARO FOCUS 350S and the RIEGL VZ-400i.

Chapter 3

Previous works

Contents

In this chapter we analyse previous works on TLS scans noise detection, listing their strengths and weaknesses. Note that these points are sometimes called outliers depending on the community. Here we will not address the surface noise filtering problematic (Digne and De Franchis [2017]) i.e. the correction of small deviations around the real surface.

3.1 3D based methods

The methods presented here operate directly on the scan, processing the 3D points without projecting or transforming them first.

Density based methods

In Raumonen et al. [2013], a sphere of a set radius (here 1.5cm) was defined at each point, if the sphere contained too little points (here 3 points) the associated point was filtered. Additionally, a partition of the point cloud was used to filter the point cloud using its connectivity. The partition is a set of small patches covering the point cloud and each point belongs to one and only one patch. The point cloud was covered with larger spheres (3cm radius) and each patch covered by less than three balls are considered not connected to the rest of the point cloud and filtered.

- Pros : This method should not over-filter for the highest scanner resolution, it is fast and works on co-registered point clouds (point clouds of a given object taken from different points of view registered in a single basis)
- Cons : This method is sensible to the varying point density in the point cloud and it will have trouble filtering noise points close to a non-noisy surface. Series of points extending from a surface to another (case of mixed points generated by two surfaces close to one another, well known phenomena, reported for example in Adams and Probert [1996] or Tuley et al. [2005]) will also be problematic since their density and connectivity to the rest of the scan will still be high. Also since the filtering is performed on the registered scans, the methods may collapse in the presence of sky noise. Finally, this method is influenced by a lot of parameters (4 filter parameters, 2 partition parameters), they are not easy to tune and dependant on the object to be filtered geometry and scanner parameters (resolution, number of co-registered positions).

Hackenberg et al. [2015] proposed a method where a random point was chosen in the scan and a cluster was created. All the neighbours closer than d (d a distance threshold, $d = 5mm$ was used in this paper) were added to the cluster. This operation was iterated until no new point could be added to the cluster, a new random point was chosen and a new cluster was created, these steps were repeated until every point belonged to a cluster. Noise is finally filtered by removing all clusters containing only one point.

- Pros : The filtering is dependant on only one parameter. This method may allow the retrieval of small components (at the cost of not filtering points close to the actual surfaces). It works on co-registered scans
- Cons : Similar problems to Raumonen et al. [2013], This method may yield different filtering quality depending on the elevation angle (due increase in point density) and resolution (at constant d parameter). This method will have difficulties detecting the noise close to actual surfaces.

Angle based method

In Tuley et al. [2005] for each scan point, a box was generated behind it. The box is oriented along the viewing direction and positioned so that the interest point is at the center of the front face (face perpendicular to the viewing direction with the lowest depth). The box size and orientation is user defined by 4 parameters : its depth (dimension along the viewing direction), width, height (dimensions orthogonal to the viewing direction) and roll angle (rotation angle around the viewing direction). A PCA was performed on the points in the box (points of interest included). Based on this, two different features (surfaceness and surface normal) and 6 labelling schemes were explored. If a certain criterion was met on the considered feature(its value was above a user defined threshold)then the chosen labelling scheme was applied. The surfaceness feature is defined with the PCA coefficients and describes if the point sample is mostly 2D. The surface normal is the angle between the eigenvector with the lowest eigenvalue and the viewing direction. The labelling schemes tested were : naive (marked the interest point only), aggressive (marked all points in the box), accumulator (the number of time a point should be marked with the

aggressive scheme was recorded and it was labelled as noise is it exceeds a user defined threshold), exclusive (marked like aggressive except for the interest point), blind window (marked like aggressive except for a depth near the interest point) and blind exclusive window (marked like aggressive except for a depth near the interest point and the interest point). All marked points were filtered.

- Pros : -
- Cons : This method depends on many parameters (box size, orientation, various thresholds) which themselves depend on the scene geometry. It exhibited poor performances (high false positive rates for acceptable true positive rates) and is computationally heavy.

Learning based method

Rakotosaona et al. [2019] proposed a deep learning based method to detect and remove outliers (e.g. outliers points obtained after a stereo reconstruction, possibly mixed point noise and sky noise) and mitigate surface noise (small variations around the real surface). They use two different networks trained for two different purposes. The first network is trained to detect and remove outliers and the second to correct variation due to surface noise and biases. We will focus on the first network since it is the one performing the task we are interested in. The network takes as an input a small subset of points centered around a given point, it then outputs the probability that that point is an outlier. The training is done via synthetic data artificially corrupted or scans of higher quality. The outliers were generated as a Gaussian noise with a deviation equal to 20% of the object.

- Pros : Very good performances
- Cons : Needs properly labelled scan parts with different object shapes for training. Although it is an obvious prerequisite for a learning method, several problems may arise when applying this technique to TLS scans. For good performances the training examples must closely represent noise distribution. However the noise range distribution of the mixed point noise is very sensitive to the distances of the involved surfaces (Wang et al. [2016]). Also the network is designed for point cloud with uniform density, and as we have proved in Chapter 2 the point density varies greatly in a given TLS scan.

3.2 2D based methods

The methods presented in this section operate on scans projected in 2D. Thus they process a different neighborhood and require a scan-to-image projection method.

Density based method

Cifuentes et al. [2014] projected the scan as an equirectangular range image, and, for each point, its neighbourhood in a 3 by 3 window was analysed. If less than $a\%$ (the allocation threshold) of the points contained in the window had an absolute distance difference lower than a distance threshold d then the centre point of the window was classified as noise.

- Pros : The output of this method is dependant on only two parameters (maybe 3 if the window size is considered, which was not done in the article)
- Cons : The output is highly dependent on local density of points, which for noisy points can be influenced by the distance to the target and its elevation angle, the distance between the foreground and background object for mixed points and the scanner resolution. For valid points scanner resolution, distance to the target, elevation angle and incidence angle may induce false detection. This lead to many different parameter combinations depending on the situation (as shown in Table 4 of the article).

TIN based methods

Three variants of the TIN (Triangular Irregular Network) based method were analysed by Tang et al. [2007] :

Variant 1 : Discontinuity triangles

First a triangular irregular network (TIN) is computed : on the equirectangular projection neighbours in the 4-neighbouring (up-down-left-right) are connected and for each square the two point on the shortest diagonal in 3D are connected. Discontinuity triangles are detected as all triangles

with one of their edge longer than a specified threshold. Every triangle adjacent to a previously detected discontinuity triangle is also labelled as a discontinuity triangle. All discontinuity triangle edges are removed and every unconnected point is detected as noise.

- Pros : The result of this method is only dependant on one parameter
- Cons : This method will have trouble detecting noise points close to the real surface (especially for mixed points generated by surfaces close to one another at high resolution or elevation angle).

Variant 2 : Triangle normals

For each triangle of the TIN the angle between the viewing direction at the triangle centroid was computed. Every triangle with an angle superior to a user defined threshold, or adjacent to such a triangle were marked as discontinuity triangles. All edges belonging to a discontinuity triangle were removed and all unconnected points were labelled as noise

- Pros : This method is robust against density changes, uses the most relevant neighbouring relations, depends on only one parameter and showed the best performances overall between all the tested filters in Tang et al. [2007]. This filter was used in Larkins et al. [2009].
- Cons : The authors showed that it is hard to find a compromise on the angle parameter to detect points close to the real surface and keep a low false positive rate (false positive detection caused by surface noise). Also the method being extremely local (only the immediate neighbours are considered) and influenced by the triangulation method (here the smallest diagonals are connected, thus some triangles are ignored) it may be highly impacted by surface noise.

Variant 3 : Cone

Using the equirectangular projection, the 8-neighbourhood (same than a 3 by 3 window) around each point was analysed. For each point a cone directed by the viewing direction and of an user defined angle was casted at each point. If more than a user defined number of points in the 8-neighbourhood was inside the cone then the point was labelled as noise.

- Pros : The filtering quality depends only on two parameters. Gives some of the best overall performances among the filters tested in Tang et al. [2007].
- Cons : On every case tested in Tang et al. [2007] the normal filter performed better, especially on scenes presenting small edges (small distances between the foreground and background), also the normal filter result depends only on one parameter.

3.3 TLS scans projections

To apply a 2D filtering method, the 3D point cloud needs to be projected on a 2D grid i.e. an image. The acquisition process of the TLS being spherical, the projection of the 3D point cloud is similar to the problem of projecting the earth surface onto a flat map. This mapping problem has been extensively studied since the antiquity and multiple projecting schemes were developed. The projections were developed in the context of navigation and cartography and, in this application, the main preoccupations were distance conservation (equidistant), shape preservation (conformal) and local area conservation (equiarea). One or several of these properties were were achieved at the price of massive distortions and/or un-mappable portions of the globe. Although, in the context of TLS scans projections the conformal, equidistant and equiarea properties are of little interest. The aforementioned filtering techniques are all based on the visual neighborhood i.e. close scanning directions should stay close in the resulting projection. A simple and very commonly used projection is the equirectangular projection. In this projection the horizontal (resp. vertical) position on the map is a linear function of the azimuth (resp. elevation). Contrary to the usual mapping of the earth surface (thus a continuous surface) to a map, new constrains and paradigms emerges when mapping a 3D scan i.e. a discrete object to a map. Indeed several pixels can be mapped to a single pixel, making the projection constrains lighter but as Houshiar et al. [2015] reports better results are achieved in most applications with finer image resolution. Also, since a TLS scans surrounding space with a regular angular step, a one to one correspondence between a scan and an image, with no point loss and good neighbourhood properties should exist (Houshiar and Nüchter [2015]). In practice, as Käshammer and Nüchter [2015] reported, scanning process and scene irregularities induce point losses and pixels displacement. This problem was partially avoided by Eysn et al. [2013] by interpolating scan coordinates before storing them in the image pixels. This method allows to get

back to the less constrained continuous case but has several drawbacks. First since the coordinates are interpolated, the original scan data is lost (which is a problem in a application where the scan data must only be ”translated” in a 2D format such as compression in Houshiar and Nüchter [2015]). Second interpolated will still produce neighbourhood errors if the coordinates were altered by some scene or scanning process irregularities.

3.4 Conclusions

As we have seen during this chapter the mixed point noise detection problem as been widely studied and many techniques were explored. Although most techniques are not well suited for TLS point cloud processing. Indeed most techniques are sensitive to density variations in the scan which are prominent in TLS scans. The best suited techniques are the 2D angle based methods. Indeed, the use of a local processing in the equirectangular projection allows a method to implicitly be adaptive to density augmentation with the elevation. Also the angle feature is robust against density augmentation. However the method proposed by Tang et al. [2007] is based on a TIN, a structure only allowing for very local information processing, making the method lack in robustness. In Chapter 5 we will propose a detection method trying to overcome these problems.

To the best of our knowledge the sky noise problematic was not discussed in the literature. We thus propose in Chapter 5 to analyse the phenomenon and develop a detection method specialised to capture only this kind of noise.

The equirectangular projection is a common and well know projection and lots of applications rely on its properties. Käshammer and Nüchter [2015] reports several inconsistencies when applying this projection to TLS scans. We propose in Chapter 4 to investigate, quantify and solve these problems.

Chapter 4

Equirectangular projection

Contents

State of the art filtering methods often rely on an equirectangular projection of the scan (e.g. Tang et al. [2007], Xiong et al. [2013], Larkins et al. [2009], Cifuentes et al. [2014] etc). We propose in this chapter both an analysis of that procedure to show that its original formulation is ill-defined for LiDAR scan processing and a new procedure, solving this issue.

4.1 Equirectangular projection formal definition

We first need to lay the basis of discrete equirectangular projection. In this section we formally define a discrete equirectangular projection and its key properties for local image-based processing.

General formulation

An equirectangular projection T for LiDAR scans assigns, to every point P in the set of points S acquired during a scan, a 2D coordinate (pixel) p on a 2D coordinate grid G. Also, in the equirectangular projection, scan points acquired from two neighbouring directions must be mapped to neighbouring pixels in G. For the sake of simplicity, points location in 3D will be exclusively given in spherical coordinates.

For every point P_i acquired during a scan we will consider the following properties : its location, $(R_i, \theta_i, \varphi_i)$, its return intensity I_i and its acquisition number i. The i^{th} point acquired has the acquisition number i.

We can obtain a map (for example a range map R_{map}) by assigning a given point property (range, return intensity etc) to the 2D position given by the equirectangular projection.

In a map, point azimuth is usually represented by the column position and the elevation by the line position (see figure 4.1).

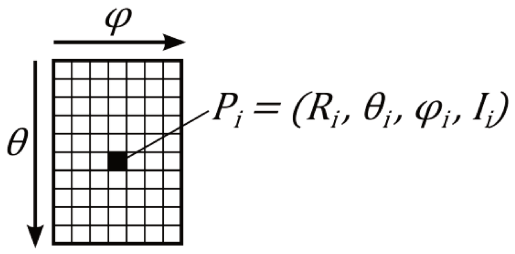

Figure 4.1 – Equirectangular image principle.

For a pixel p in G with coordinates (u, v) (u the line index and v the column index), let T map the 3D direction (θ, φ) to (u, v). A neighbour of p, p_1 at coordinates $(u+1, v+1)$ then represents a direction $(\theta+\delta_{r\theta}, \varphi+\delta_{r\varphi})$

where $\delta_{r\theta}$ and $\delta_{r\varphi}$ define the angular steps. Thus a 3D point P_i is mapped to (u, v) if and only if :

$$\theta - \frac{\delta_{r\theta}}{2} < \theta_i \leq \theta + \frac{\delta_{r\theta}}{2} \tag{4.1}$$

$$\varphi - \frac{\delta_{r\varphi}}{2} < \varphi_i \leq \varphi + \frac{\delta_{r\varphi}}{2} \tag{4.2}$$

A natural choice for equirectangular projection of TLS scans is :

$$\delta_{r\theta} = \delta_{r\varphi} = \delta \tag{4.3}$$

where δ is the scan angular resolution.

From this we can write the following two properties, defining the neighbourhood coherence, for the projection T :

$$\begin{aligned} T : S &\to \mathbb{N}^{*2} \\ P &\mapsto (u, v) \end{aligned}$$

Property 1 (Line coherence)**.**

$$\forall (P_i, P_j) \in S^2, |\theta_i - \theta_j| < \delta \iff \begin{cases} T(P_i) = (u_k, v_i) \\ T(P_j) = (u_k, v_j) \end{cases}$$

Meaning that for any pair of points in the scan, the projection T must map these points to the same line u_k, if and only if they have a close enough elevation (a difference lower than the angular resolution).

Property 2 (Column coherence)**.**

$$\forall (P_i, P_j) \in S^2, |\varphi_i - \varphi_j| < \delta \iff \begin{cases} T(P_i) = (u_i, v_k) \\ T(P_j) = (u_j, v_k) \end{cases}$$

Meaning that for any pair of point in the scan, the projection T must map these points to the same column v_k, if and only if they have a close enough azimuth (a difference lower than the angular resolution).

Neighbourhood coherence is central in assuring that a local method applied on an equirectangular image (e.g. Cai et al. [2005], Tang et al. [2007], Cifuentes et al. [2014]) uses meaningful groups of pixel for each computation.

A laser scanner with no mechanical or numerical imperfection should sample every direction it has access to only once. Then every point in S should be mapped to a unique map position (or pixel). We can thus add the following desired property to T :

Property 3 (Lossless)**.**

$$\forall (P_i, P_j) \in S^2, P_i \neq P_j \iff T(P_i) \neq T(P_j)$$
$$\forall P_i \in S, \exists (u, v) \in \mathbb{N}^{*2}, T(P_i) = (u, v)$$

Meaning that two distinct points must be mapped to two distinct pixels, and every point must be mapped to a pixel.

An equirectangular projection function T satisfying all three properties is called a perfect projection.

We will now see that this formulation is not adapted for LiDAR data and how classical equirectangular approaches fail to yield coherent results.

Adaptation for TLS data

A classical but naive approach to define a projection fulfilling properties 1, 2 and 3 (section 4.1) is to define a set grid G and to compute a pixel position directly from the point coordinates. For example, the grid can be defined by a δ angular step and the association of $(\max_S(\theta), \max_S(\varphi))$ to the grid position $(1, 1)$. Then the map coordinates (u_i, v_i) of a point P_i are given by :

$$u_i = 1 + \text{round}\left(\frac{\max_S(\theta) - \theta_i}{\delta}\right) \tag{4.4}$$

$$v_i = 1 + \text{round}\left(\frac{\max_S(\varphi) - \varphi_i}{\delta}\right) \tag{4.5}$$

In practice this naive approach satisfies none of the three properties stated above because of rounding approximations and mechanical errors.

Especially numerical instabilities in the spherical base make the azimuth inconsistent for map coordinates calculation (figure 4.2), assigning inconsistent column indices for extreme elevations (close to the zenith or nadir).

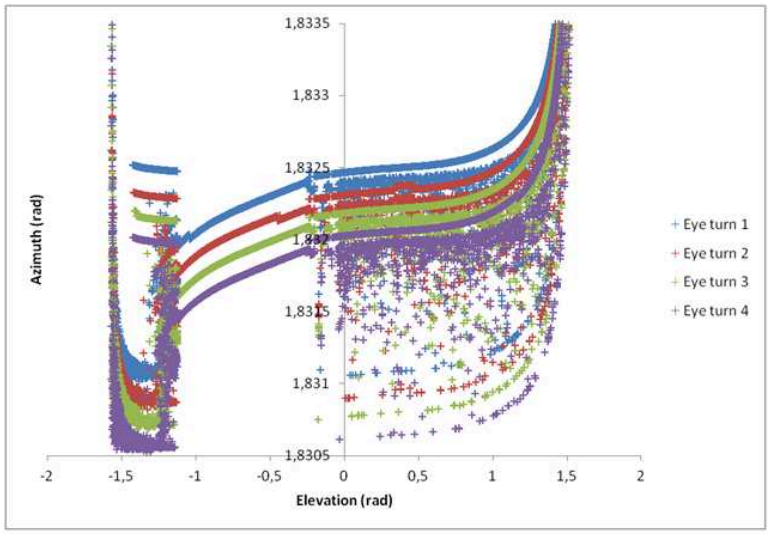

Figure 4.2 – Recorded azimuth versus recorded elevation for a scan in ultra resolution ($\frac{\tau}{4}10^{-4}$). In blue green red and purple are the values of azimuth versus elevation for four consecutive scanner eye turns (each color corresponds to the points acquired during a specific turn)

To overcome this issue we modify the properties desired for the equirectangular projection based on how the scanner operates. The k^{th} column in the equirectangular map is now defined as all the points acquired during the k^{th} turn of the scanner eye. Property 2 becomes :

Property 4 (Column coherence adapted for LiDAR)**.**

$$\forall (P_i, P_j) \in S^2, (P_i, P_j) \in t_k \iff \begin{cases} T(P_i) = (u_i, v_k) \\ T(P_j) = (u_j, v_k) \end{cases}$$

with t_k the set of points acquired during the k^{th} turn of the scanner eye.

Note that this description implies that for a full scan of τ in elevation by $\frac{\tau}{2}$ in azimuth (full sphere) the columns will describe a span of $\frac{\tau}{2}$ (instead of the usual τ) and the lines a span of τ (instead of $\frac{\tau}{2}$).

4.2 Equirectangular projection algorithm

In this section we present a new equirectangular projection algorithm for LiDAR scans based on the properties presented in section 4.1. The algorithm steps and workflow is summarised in figure 4.3.

Preparing the data

In this section we will describe the first three steps of our projection algorithm :

- Conversion to spherical coordinates
- Elevation regularisation and Resolution estimation
- Filtering of numerical instabilities

Conversion to spherical coordinates

The equirectangular projection maps directions (represented by a couple (θ, φ)) to pixel positions. The first step for such a projection is to convert the Cartesian coordinates into spherical coordinates, where the directions appear explicitly. To do so we used the spherical base equations presented in section 2.1, where :

$$R = \sqrt{x^2 + y^2 + z^2} \tag{4.6}$$

$$\theta = \arctan\left(\frac{z}{\sqrt{x^2 + y^2}}\right) \tag{4.7}$$

$$\varphi = \text{atan2}(y, x) \tag{4.8}$$

Elevation regularisation and resolution estimation

As previously stated, the line indices must describe a τ span. Elevations were recomputed to satisfy a τ span. Since S is sorted in acquisition order, the elevation of points acquired during the same eye turn have :

- A positive forward difference if they were acquired during the "rising" phase (from nadir, i.e. $\theta = -\frac{\tau}{4}$, to zenith, i.e. $\theta = \frac{\tau}{4}$)
- A negative forward difference if they were acquired during the "falling" phase (from zenith to nadir)

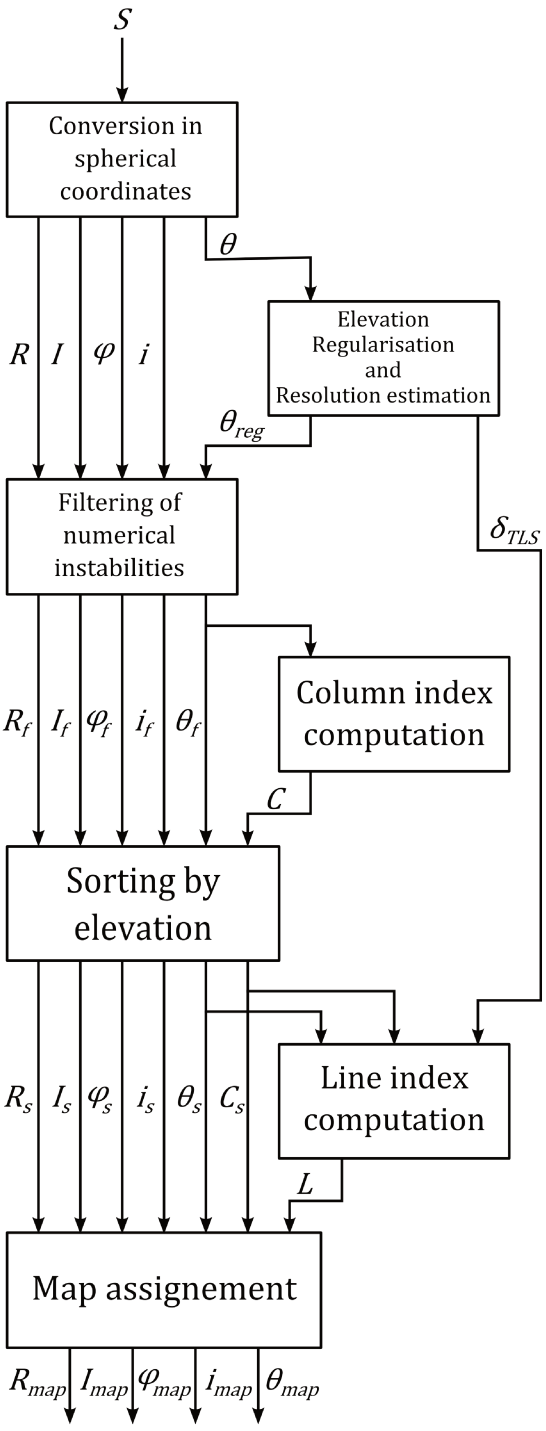

Figure 4.3 – General principle of the equirectangular projection algorithm

where the forward difference of an elevation value θ_i is defined as $\theta_{i+1} - \theta_i$. Elevations can be regularised by assigning the interval $\left[0; \frac{\tau}{2}\right]$ to the elevations of points acquired in "rising" phase and the interval $\left[\frac{\tau}{2}; \tau\right]$ for the elevations of points acquired in "falling" phase. Note that a rising phase and a falling phase are necessarily separated by a local extremum in elevation. Also note that the spherical basis equations are not redefined to yield regular elevations. Indeed if one chooses to define the elevation as in equation (4.9) :

$$\theta = \operatorname{atan2}\left(z, \operatorname{sign}(y)\sqrt{x^2 + y^2}\right) \tag{4.9}$$

the elevations would directly have a τ span but would be highly unstable for small y values. For numerical stability we decided to keep the original and highly stable elevation formulation and to regularise it afterwards.

To regularise elevation, the median of the elevation forward differences between two local extrema were computed for every consecutive extrema pairs. If the median was positive then the elevation section was considered to be in a "rising" phase, otherwise it was considered to be in a "falling" phase. Note that since we use all local extrema, all forward differences signs must be identical in an elevation section. The medians were stored in a list $\delta List$ to estimate the resolution. Indeed, in a normally working scanner, most consecutive elevation points will be spaced by a δ interval (with some zero mean noise). Then a good estimator for δ is :

$$\widehat{\delta_{TLS}} = \operatorname{median}(\delta List) \tag{4.10}$$

Algorithm 1 shows the carried procedure to regularise the elevation and estimate the resolution.

Algorithm 1 Elevation regularisation and resolution estimation

Input θ : Elevation list for the scan S
Output $Reg\theta$: Regularised elevation list ; δ : Estimated resolution

$extremaList \leftarrow$ the list of index for the local extrema in θ
$N_{extrema} \leftarrow$ length of $extremaList$
$\delta List \leftarrow \{\}$
$\theta_{reg} \leftarrow \{\}$
for each i in $[1, N_{extrema} - 1]$ **do**
  $start \leftarrow extremaList(i) + 1$
  $stop \leftarrow extremaList(i + 1) - 1$
  $\theta List \leftarrow$ All θ_j values for $j \in [start, stop]$
  $d\theta List \leftarrow$ All forward difference values for $\theta List$
  $r \leftarrow \text{median}\,(d\theta List)$
  add $|r|$ to $\delta List$
  if $r > 0$ **then**
    $\theta List \leftarrow \frac{\tau}{4} + \theta List$
  else
    $\theta List \leftarrow \frac{3\tau}{4} - \theta List$
  end if
  add $\theta List$ to $Reg\theta$
end for
$\delta \leftarrow \text{median}\,(\delta List)$

An example of regularised elevation for the first 80000 points of a scan taken with a 0.009 ° angular resolution is given Figure 4.4.

Filtering of numerical instabilities

To insure robustness in the following procedures, numerically unstable elevation values need to be filtered. Analysing equation (4.7) reveals that θ is unstable (meaning that small changes in x, y or z lead to meaningful changes in θ) only if $z \to 0$ **and** $\sqrt{x^2 + y^2} \to 0$, thus if $R \to 0$. Then points with a range lower than a threshold $R_{threshold}$ were discarded to account for numerical instabilities. This partly breaks the lossless property, but as we will see this method allows us in practice to get much closer to being lossless than the naive method. Also the loss is in a perfectly defined and usually uninteresting area, i.e. a few centimeters from the exit of the laser.

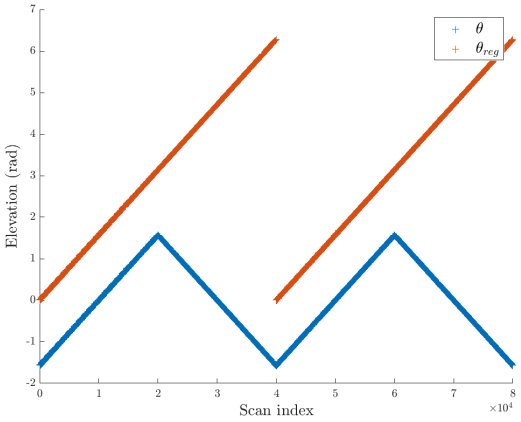

Figure 4.4 – Elevation regularisation, In blue the original Elevation values, in orange the regularised values.

Column indices computation

Our equirectangular mapping method uses the acquisition order (usual order of a raw scan : point order in the scan file follows the order in which points were acquired) instead of the azimuth for column indexing. A full turn of the scanner eye can be identified as all points between two local minima in elevation. We can compute the column indices by assigning the index 1 to all the points acquired between the first scan point and the next local minimum (excluded), the index 2 to all the points acquired between the first local minimum (included) and the third (excluded) etc...Finally any point will have a column index equal to the number of local minima that precedes it plus one (included itself if it is a local minimum). Figure 4.5 shows an example of column index computation for the first 80000 points of a scan taken with a 0.009 ° angular resolution.

Algorithm 2 Column index computation

Input $Reg\theta$: Regularised elevation list for the scan S
Output C : Column index list

1: $minimumInd \leftarrow$ the indicator for the local minima in $Reg\theta$ (i.e. $minimumInd_i = 1$ if $Reg\theta_i$ is a local minima and $minimumInd_i = 0$ otherwise)
2: $l \leftarrow$ the length of $Reg\theta$
3: **for each** i in $[1, l]$ **do**
4: $\quad C_i \leftarrow \sum_{j \leq i} minimumInd_j$
5: **end for**
6: $C \leftarrow C - C_1 + 1$

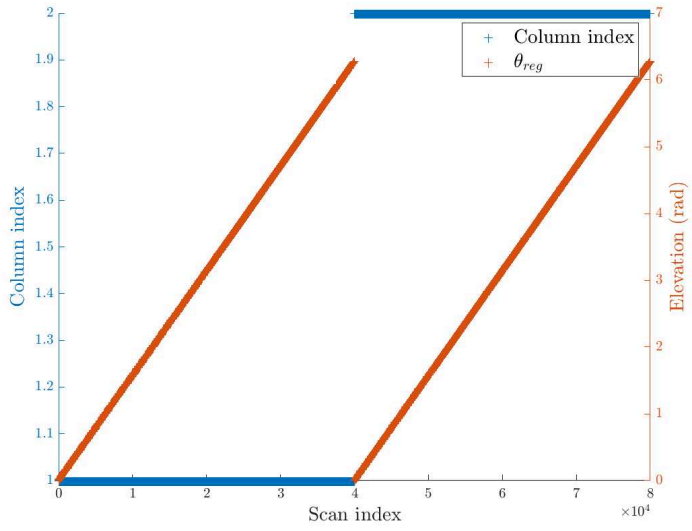

Figure 4.5 – Column index computation.

Line indices computation

Elevation jump detection

Line indices were computed by finding sets of points with almost constant elevation. Sets of points with almost constant elevation were detected by sorting the points elevation in ascending order and looking for "plateaus" (see Figure 4.6 for an example of a part of a scans elevation

sorted in ascending order). Note that we applied the sorting permutation to the point list and the column index list for the final image index assignment. In practice, sampling irregularities and column misalignment (when the sampling of two consecutive column did not start at the exact same elevation), may cause the elevation jump value to vary. In the example given Figure 4.7, δ would not be a good choice for jump detection since it would miss all jumps.

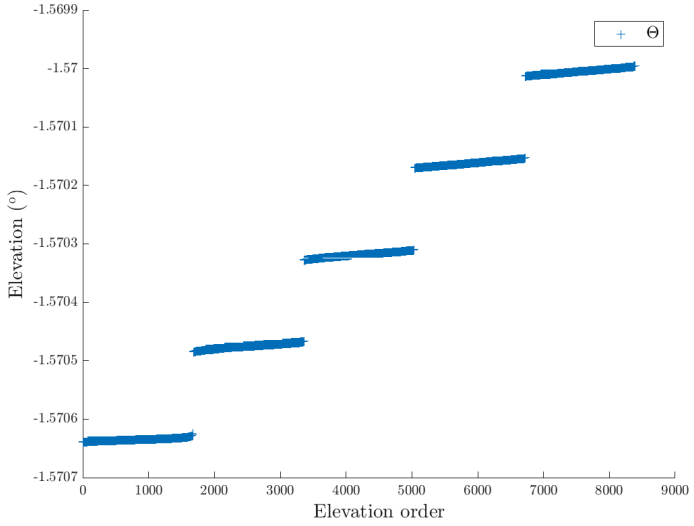

Figure 4.6 – Sorted elevation values.

The jump value $\theta_{threshold}$ was initialized as $\theta_{threshold} = \delta$ and a jump was detected at the k^{th} position if :

$$\Theta_{k+1} - \Theta_k \geq \theta_{threshold} \tag{4.11}$$

Where Θ denotes the sorted elevation list. $\theta_{threshold}$ was then a fitting jump value if it detected at least all the real jumps in the scan, thus if each line (sets of points between two jumps) contained less than N_{column} points, with N_{column} the number of columns (otherwise it could be split). The jump detection procedure was performed with lower and lower $\theta_{threshold}$ values until this condition was met ($\frac{\delta}{10}$ was subtracted to $\theta_{threshold}$ at each unsuccessful iteration). Note that if $\theta_{threshold} = 0$ the procedure cannot fail and will consider that a jump is present between each point.

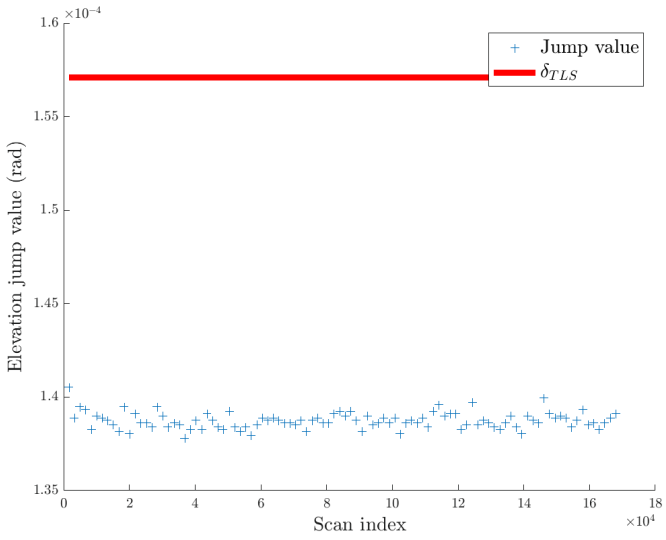

Figure 4.7 – Elevation jump values.

Algorithm 3 Line index computation

Input Θ : Regularised and sorted elevation list for the scan S ; C Column index list ; δ : Estimated scan resolution
Output $jumpIdx$: Elevation jump index list

$N_{column} \leftarrow \max(C)$
$N_{columnMax} \leftarrow N_{column} + 1$
$d\Theta \leftarrow$ all forward difference values for Θ
$frac \leftarrow 1$
while $N_{columnMax} > N_{column}$ **do**
    $\theta_{threshold} \leftarrow frac\,\delta$
    $jumpIdx \leftarrow$ all indices i where $d\Theta_i \geq \theta_{threshold}$
    $djumpIdx \leftarrow$ all forward difference values for $jumpIdx$
    $N_{columnMax} \leftarrow \max(djumpIdx)$
    $frac \leftarrow frac - 0.1$
end while
$K \leftarrow$ the length of $jumpIdx$
$N \leftarrow$ the length of Θ
if $jumpIdx_K \neq N$ **then**
    Add N to $jumpIdx$
end if
Add 0 at the beginning of $jumpIdx$

Line correction

At this stage we have no guarantee that only real jumps were detected. Consequently a line merging procedure was then carried. If a false jump detection exists, then at least one of the two lines it delimits are at least half empty (it contains less than $\frac{N_{column}}{2}$ points). For each potential false jump, neighbouring lines were verified to check if the current line and an adjacent line could be merged. Lines can be merged if they do not have any column index in common and if the elevation differences stay within the angular resolution interval. Finally, lines were merged by ignoring the detected jump that separates them. After verifying every potential false jump, a new detection was performed and the full line merging process was repeated until no new or no potential false jump were detected. The line correction procedure is given with more details in algorithms 4, 5 and 6. Every point from the first point in the sorted list to the first jump (included) were assigned the index 1, every point from the first jump (excluded) to the second (included) were assigned the index 2, etc. A point line index is then equal to 1 plus the number of jumps that precedes it (itself excluded). Finally each point was assigned to the coordinates given by its line and column index. Note than a range (resp. intensity) map is obtained by considering only the range (resp. intensity) for each point. In the rest of this thesis we will refer to map coordinates as **pixels** and to 3D coordinates + return intensity as **points**.

Algorithm 5 Line correction (merge checking function)

Input Θ : Regularised and sorted elevation list for the scan S ; C Column index list ; δ : Estimated scan resolution ; $jumpIdx$: Elevation jump index list

Output $mergePrev$: Boolean value indicating if the lines i and $i-1$ can be merged, $mergeNext$: Boolean value indicating if the lines i and $i+1$ can be merged

function CHECKMERGE($\Theta, C, jumpIdx, i$)
  $mergePrev \leftarrow false$
  $mergeNext \leftarrow false$
  $(\theta_{line}, C_{line}) \leftarrow$ GetLine($\Theta, C, jumpIdx, i$)
  if $i - 1 > 0$ **then**
    $(\theta_{Prev}, C_{Prev}) \leftarrow$ GetLine($\Theta, C, jumpIdx, i-1$)
    $max\theta_{Prev} \leftarrow \max(\max(\theta_{line}), \max(\theta_{Prev}))$
    $min\theta_{Prev} \leftarrow \min(\min(\theta_{line}), \min(\theta_{Prev}))$
    if no element of C_{line} is in C_{Prev} **then**
      $colOk \leftarrow true$
    else
      $colOk \leftarrow false$
    end if
    if $max\theta_{Prev} - min\theta_{Prev} \leq \delta$ **and** $colOk$ **then**
      $mergePrev \leftarrow true$
    end if
  end if
  $n_{jump} \leftarrow$ the length of $jumpIdx$
  if $i + 2 < n_{jump}$ **and then**
    $(\theta_{Next}, C_{Next}) \leftarrow$ GetLine($\Theta, C, jumpIdx, i+1$)
    $max\theta_{Next} \leftarrow \max(\max(\theta_{line}), \max(\theta_{Next}))$
    $min\theta_{Next} \leftarrow \min(\min(\theta_{line}), \min(\theta_{Next}))$
    if no element of C_{line} is in C_{Next} **then**
      $colOk \leftarrow true$
    else
      $colOk \leftarrow false$
    end if
    if $max\theta_{Next} - min\theta_{Next} \leq \delta$ **and** $colOk$ **then**
      $mergeNext \leftarrow true$
    end if
  end if
  return $(mergePrev, mergeNext)$
end function

Algorithm 4 Line correction

Input Θ : Regularised and sorted elevation list for the scan S ; C Column index list ; δ : Estimated scan resolution ; $jumpIdx$: Elevation jump index list

Output L : Line index list

function LINEINDEX(Θ, C, $jumpIdx$, δ)
  $N_{column} \leftarrow \max(C)$
  $dJump \leftarrow$ all forward difference values for $jumpIdx$
  $falseJumps \leftarrow$ all indices i where $dJump_i \leq \frac{N_{column}}{2}$
  $falseJumpsPrev \leftarrow \{\}$
  $n_{false} \leftarrow$ the length of $falseJumps$
  while $n_{false} > 0$ **and** $falseJumpsPrev \neq falseJumps$ **do**
    for each $i \in [1, n_{false}]$ **do**
      $j \leftarrow$ the i^{th} element of $falseJump$
      $(mergeP, mergeN) \leftarrow$CheckMerge $(\Theta, C, jumpIdx, j)$
      if $mergeP$ **and** $mergeN$ **then**
        $(\theta_{line}, C_{line}) \leftarrow$ GetLine$(\Theta, C, jumpIdx, j)$
        $(\theta_{Prev}, C_{Prev}) \leftarrow$ GetLine$(\Theta, C, jumpIdx, j-1)$
        $(\theta_{Next}, C_{Next}) \leftarrow$ GetLine$(\Theta, C, jumpIdx, j+1)$
        if $|\text{median}(\theta_{line}) - \text{median}(\theta_{Prev})| \leq |\text{median}(\theta_{line}) - \text{median}(\theta_{Next})|$ **then**
          remove the j^{th} element of $jumpIdx$
        else
          remove the $j + 1^{th}$ element of $jumpIdx$
        end if
      else if $mergeP$ **then**
        remove the j^{th} element of $jumpIdx$
      else if $mergeN$ **then**
        remove the $j + 1^{th}$ element of $jumpIdx$
      end if
    end for
    $falseJumpsPrev \leftarrow falseJumps$
    $dJump \leftarrow$ all forward difference values for $jumpIdx$
    $falseJumps \leftarrow$ all indices i where $dJump_i \leq \frac{N_{column}}{2}$
  end while
  $jumpInd \leftarrow$ the jump indicator (i.e. $jumpInd_i = 1$ if $i \in jumpIdx$ and $jumpInd_i = 0$ otherwise)
  $l \leftarrow$ the length of Θ
  for each $i \in [1, l]$ **do**
    $L_i \leftarrow \sum_{j \leq i} jumpInd_j$
  end for
  $L \leftarrow L - L_1 + 1$
  return L
end function

Algorithm 6 Line correction (get line function)

Input Θ : Regularised and sorted elevation list for the scan S ; C Column index list ; $jumpIdx$: Elevation jump index list ; i Line number
Output θ_{line} Elevation list for line i ; C_{line} Column index list for line i

1: **function** GETLINE(Θ, C, $jumpIdx$, i)
2: $start \leftarrow jumpIdx_i$
3: $stop \leftarrow jumpIdx_{i+1}$
4: $\theta_{line} \leftarrow$ all Θ_i values for $i \in [start, stop - 1]$
5: $C_{line} \leftarrow$ all C_i values for $i \in [start, stop - 1]$
6: **return** (θ_{line}, C_{line})
7: **end function**

An example of range map and intensity map obtained through this method is given figure 4.8.

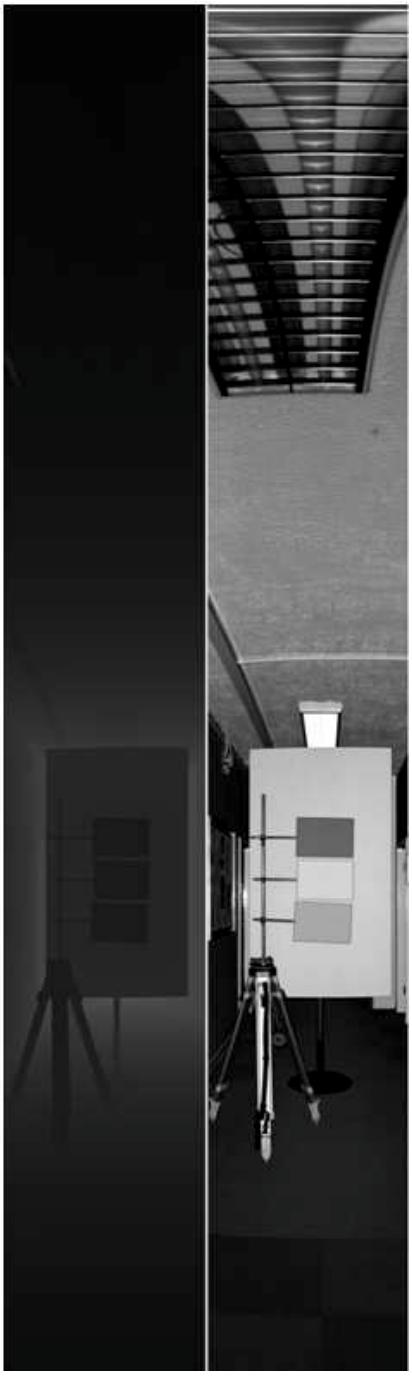

Figure 4.8 – Equirectangular Range image (left) and intensity image (right). Values displayed as grayscaled, lowest black, highest white.

4.3 Projection evaluation

We will now define a framework, based on the formalism proposed in section 4.1, to quantitatively evaluate the quality of a given equirectangular projection.

Evaluation principle

Three properties are expected from an equirectangular projection :

- **Line coherence** (Property 1)
- **Column coherence** (Property 4)
- **Lossless transformation** (Property 3)

Lossless evaluation : Lossless property can easily be evaluated by computing, for a given projection T applied on a given scan S, the fraction of scan points assigned to a pixel in the produced map $\rho_l(T, S)$:

$$\rho_l(T, S) = \frac{N_{map}}{N_{scan}} \tag{4.12}$$

with N_{map} the number of assigned pixels in the produced map and N_{scan} the original number of point in the scan.

Coherence evaluation : The coherence properties were evaluated by quantifying the fraction of pixels in the produced map with a perfectly correct neighbourhood (meaning that all neighbours are correctly placed). A neighbourhood of a pixel p of size n, $W_n(p)$, is defined as the set of pixels in a n by n pixels window centered on p. To make sense the following evaluation needs to be carried on *continuous scans*, meaning scans where all directions accessible to the scanner are sampled (meaning all directions between the set azimuth and elevation boundaries). In such scans, neighbourhood correctness can be computed from the acquisition number of each pixel.

In a continuous scan S, consider two points, P_i and P_{i+j} ($j \in \mathbb{Z}$) acquired during the same eye turn t. Considering property 4 these points should be mapped to the same column v. Remember that P_i and P_{i+j} have acquisition numbers i and $i+j$. Following this, the mapping of P_i and P_{i+j}

by T is coherent if and only if $T(P_i) = (u, v)$ and $T(P_{i+j}) = (u+j, v)$, since we are in a continuous scan. Finally, if i_{map} denotes the acquisition number map produced with a transformation T on S (thus $i_{map}(T(P_i)) = i$), any pair of pixels at positions (u, v) and $(u + j, v)$ are coherent if and only if :

$$i_{map}(u + j, v) - i_{map}(u, v) = j \tag{4.13}$$

For a continuous scan, the number of points per eye turn N_{turn} is :

$$N_{turn} = \left\lfloor \frac{\theta_{span}}{\delta} \right\rfloor \tag{4.14}$$

with θ_{span} the elevation span of the scan i.e. the difference between the set elevation boundaries.

Consider two points P_i and $P_{i+kN_{turn}}$ ($k \in \mathbb{Z}$). Since k full eye turns were performed between the acquisition of P_i and $P_{i+kN_{turn}}$ they will be sampled at the same elevation. From property 1, P_i and $P_{i+kN_{turn}}$ should be mapped to the same line u. Then the mapping of P_i and $P_{i+kN_{turn}}$ by T is coherent if and only if $T(P_i) = (u, v)$ and $T(P_{i+kN_{turn}}) = (u, v + k)$. Finally any pair of pixels at positions (u, v) and $(u, v + k)$ are coherent if and only if :

$$i_{map}(u, v + k) - i_{map}(u, v) = kN_{turn} \tag{4.15}$$

Then a pixel p at position (u, v) is coherent for its neighbourhood $W_n(p)$ if and only if it is coherent with all other pixels in $W_n(p)$. If $C(T, S; W_n)$ denotes the set of all coherent pixels produced by T on S for a neighbourhood W_n we have from equations 4.13 and 4.15 :

$$\begin{aligned} C(T, S; W_n) = \{p, p \text{ at } (u, v) \mid \forall j\, \forall k, (u + j, v + k) \in W_n(p), \\ i_{map}(u + j, v + k) - i_{map}(u, v) = kN_{turn} + j\} \end{aligned} \tag{4.16}$$

And the coherence of a projection T on a scan S for a neighbourhood W_n, $\rho_c(T, S; W_n)$ is :

$$\rho_c(T, S; W_n) = \frac{|C(T, S; W_n)|}{N_{map}} \tag{4.17}$$

where $|X|$ is the number of elements in the set X.

This methodology could be used to evaluate any neighbourhood. Experimentally, the analysis was carried on the most common neighbourhoods, W_3, W_5 and W_7. Also note that any "bigger" neighbourhood (i.e. involving more pixels) than W_7 will necessarily have worse coherence since the coherence on W_7 would also have to be satisfied. Indeed since for any neighbourhood we have :

Property 5. $\forall p \, \forall n \, \forall m, \; n < m \implies W_n(p) \subseteq W_m(p)$

we can deduce :

Property 6. $\forall T \, \forall S, \; n < m \implies |C(T, S; W_n)| \geq |C(T, S; W_m)|$

and finally :

Property 7. $\forall T \, \forall S, \; n < m \implies \rho_c(T, S; W_n) \geq \rho_c(T, S; W_m)$

To quantify the loss of coherence with the elevation or the azimuth, we can look at local coherence values, i.e. the ratio of coherent pixels per line or per column. We define the zenithal coherence $c_\theta(T, S; W_n; \theta_i)$ and the azimuthal coherence $c_\varphi(T, S; W_n; \varphi_i)$ as :

$$c_\theta(T, S; W_n; \theta_{L_i}) = \frac{|C(T, S; W_n; L_i)|}{|L_i|} \tag{4.18}$$

$$c_\varphi(T, S; W_n; \varphi_{C_i}) = \frac{|C(T, S; W_n; C_i)|}{|C_i|} \tag{4.19}$$

with :

$$\theta_{L_i} = \underset{k, P_k \in L_i}{\text{median}} \, (\theta_k) \tag{4.20}$$

$$\varphi_{C_i} = \underset{k, P_k \in C_i}{\text{median}} \, (\varphi_k) \tag{4.21}$$

Experimental setup

Projection evaluation was done on four different scans highlighting different scanning conditions :

- Indoor scanning : Few "sky points", making the point sampling more regular.

- Outdoor scanning : Lots of "sky points", which are numerically unstable, and thus hard to map correctly (because more unstable).
- Ultra High angular resolution : The highest angular resolution reachable by our scanner ($\frac{\tau}{4}10^{-4}$), with 40000 points acquired per eye turn.
- High angular resolution : Lower resolution than the Ultra one ($\frac{\tau}{2}10^{-4}$), with 20000 points acquired per eye turn.

Table 4.1 summarises the parameters of each of the four used scans for the evaluation.

Scan	δ_{TLS} (rad)	Scan condition	θ_{span} (rad)	φ_{span} (rad)
S_1	Ultra : $\frac{\tau}{4}10^{-4}$	Indoor	τ	0.28
S_2	Ultra : $\frac{\tau}{4}10^{-4}$	Outdoor	τ	0.26
S_3	High : $\frac{\tau}{2}10^{-4}$	Indoor	$\frac{\tau}{4}$	0.35
S_4	High : $\frac{\tau}{2}10^{-4}$	Outdoor	τ	$\frac{\tau}{2}$

Table 4.1 – Scans setups.

For each scan and neighbourhood size, the lossless coefficient ρ_l and coherence ρ_c were computed for the naive transformation T_{naive} and the proposed transformation T_{order}.

For fair and meaningful comparison, T_{naive} was redefined with equation 4.22 and 4.23 to have a full eye turn per column :

$$u_i = 1 + \text{round}\left(\frac{\theta_i - \min_S(\theta_{reg})}{\delta}\right) \tag{4.22}$$

$$v_i = 1 + \text{round}\left(\frac{\max_S(|\varphi|) - |\varphi_i|}{\delta}\right) \tag{4.23}$$

where θ_{reg} are the regularised elevation values.

Projection comparison results

Table 4.2 presents the results of the proposed evaluation. Here we can see that in all scans around 10% of the points are lost with the naive transformation due to rounding errors and sampling irregularities, except in the trivial narrox panorama, indoor case of S_3. The proposed transformation consistently loose around 0.1% on all scans. Coherence results

show that the naive transformation is highly impacted by sky points, especially for higher resolutions and wider neighbourhood. The proposed transformation shows almost no impact on coherence even on the widest neighbourhood tested.

		T_{naive}		T_{order}	
		ρ_l	ρ_c	ρ_l	ρ_c
W_3	S_1	0.906	0.731	1	0.999
	S_2	0.881	0.532	0.999	0.997
	S_3	0.997	0.988	0.999	0.997
	S_4	0.905	0.654	0.999	0.999
W_5	S_1	0.906	0.666	1	0.997
	S_2	0.881	0.344	0.999	0.992
	S_3	0.997	0.980	0.999	0.995
	S_4	0.905	0.554	0.999	0.996
W_7	S_1	0.906	0.627	1	0.995
	S_2	0.881	0.283	0.999	0.987
	S_3	0.997	0.973	0.999	0.993
	S_4	0.905	0.504	0.999	0.993

Table 4.2 – Projection results for W_3, W_5 and W_7 neighbourhoods.

Figures 4.9 to 4.12 show azimuthal and zenithal coherence results for each scan, neighbourhood and transformation. We can see that the zenithal coherence consistently drops when the elevation approaches the zenith ($\frac{\tau}{2}$ rad) or the nadir (0 or τ rad) on the naive transformation. As stated in section 4.1 this may be caused by numerical instabilities in azimuth at these extremes elevations. The zenithal coherence of the proposed method shows no significant discrepancy, except for elevations close to the nadir. This is probably the consequence of mixed points acquired on the scanner "skirt". Indeed these mixed points tend to be at very low distances and thus are filtered before being assigned, which in turn impacts the coherence. Drops in coherence on the naive transformation in S_2 and S_4 are caused by sky points.

Regarding the azimuthal coherence, no specific pattern emerges which seems to indicate that the image coherence does not change as the scanner head rotates. Incoherent azimuth values for the naive transformation are

caused by the azimuth drift as the elevation approaches the zenith or the nadir.

In every scan the naive transformation coherence values are highly impacted by the neighbourhood size. However the proposed transformation shows little to no effect of the neighbourhood size.

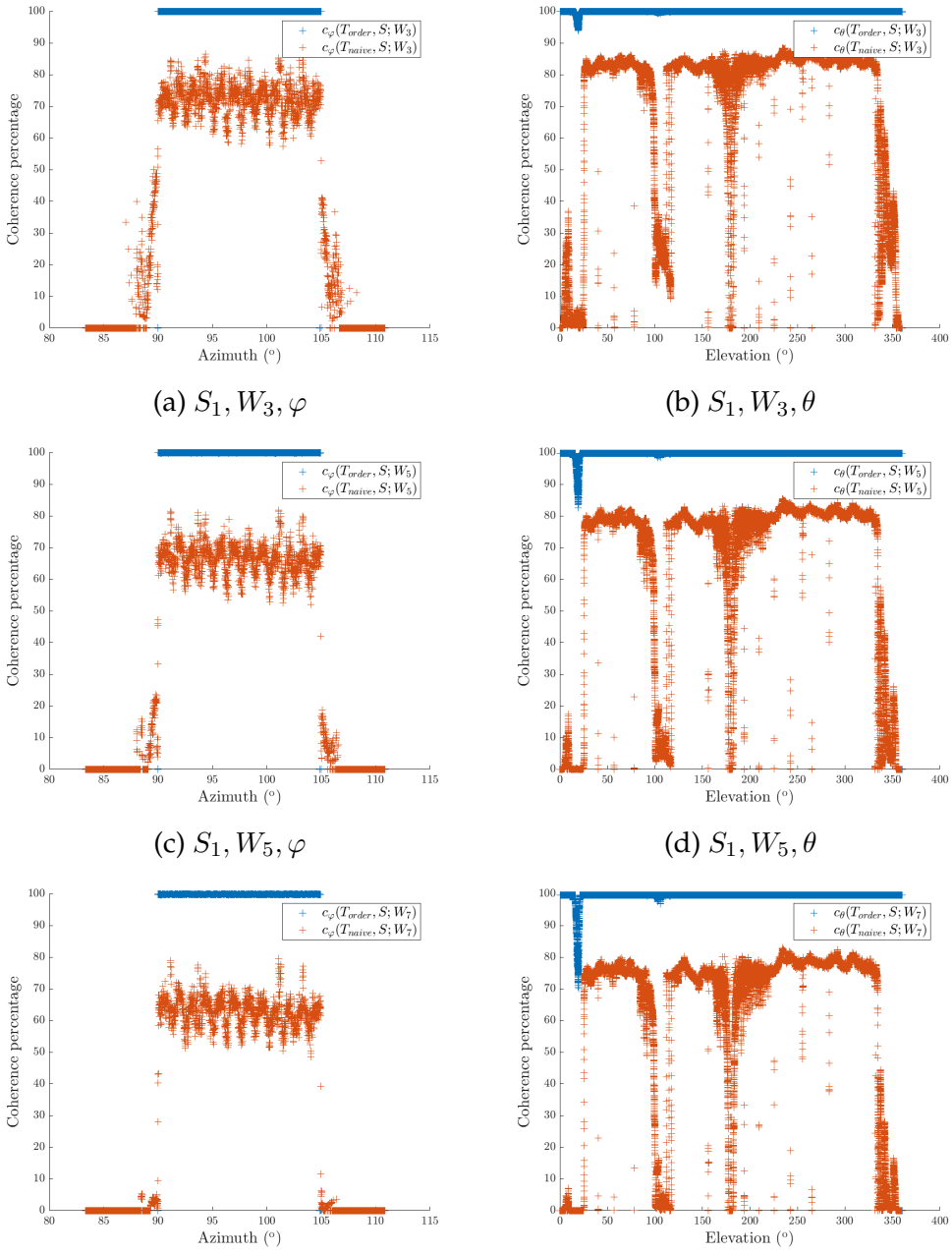

(a) S_1, W_3, φ (b) S_1, W_3, θ

(c) S_1, W_5, φ (d) S_1, W_5, θ

(e) S_1, W_7, φ (f) S_1, W_7, θ

Figure 4.9 – Projection coherence for S_1. In blue the coherence of the proposed method, in orange the coherence of the naive method.

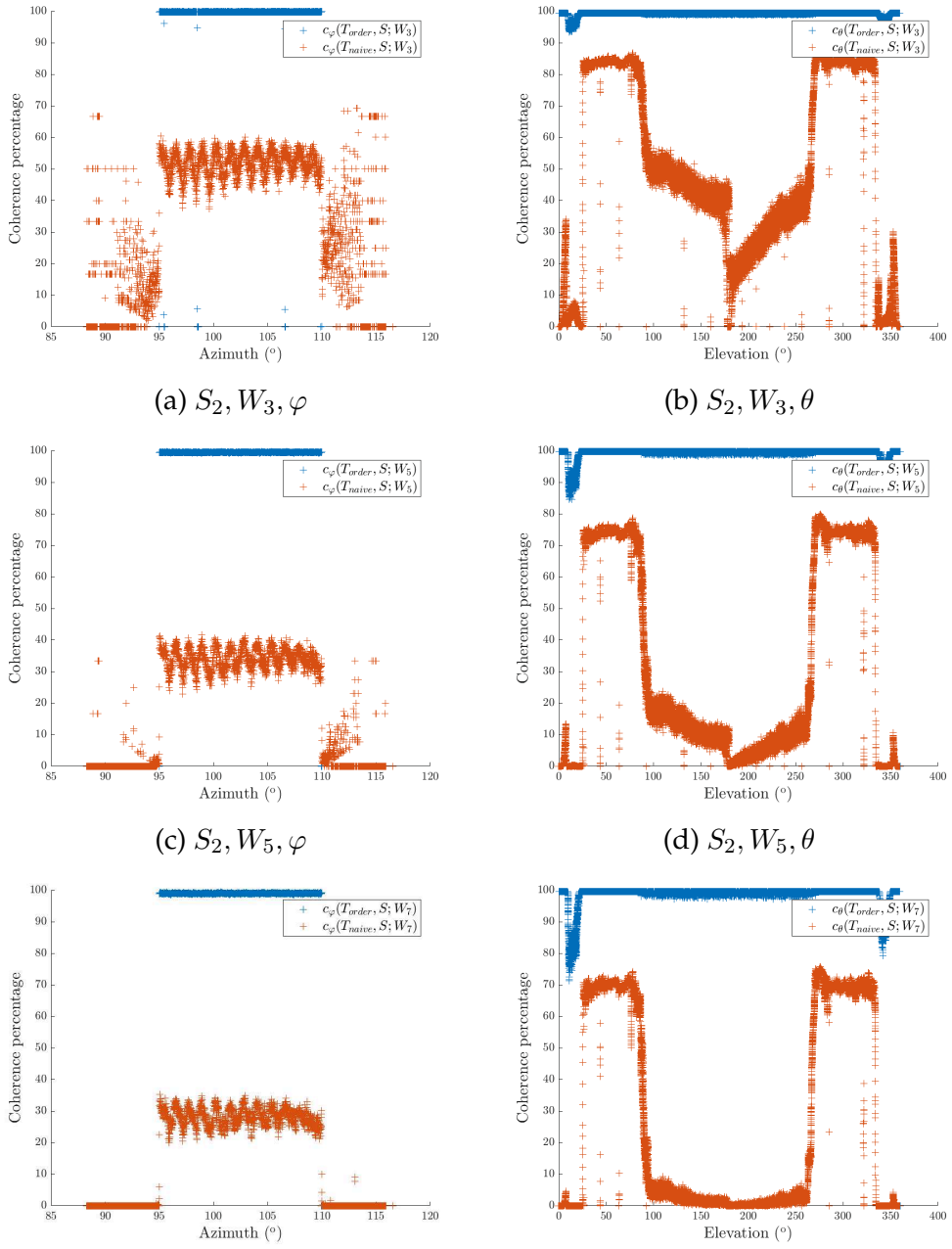

(a) S_2, W_3, φ (b) S_2, W_3, θ

(c) S_2, W_5, φ (d) S_2, W_5, θ

(e) S_2, W_7, φ (f) S_2, W_7, θ

Figure 4.10 – Projection coherence for S_2. In blue the coherence of the proposed method, in orange the coherence of the naive method.

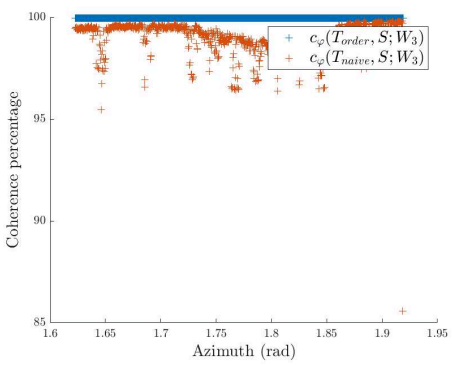

(a) S_3, W_3, φ

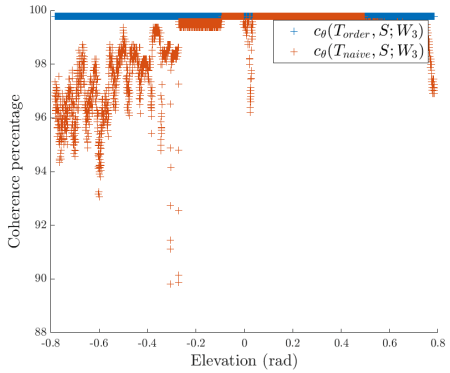

(b) S_4, W_3, θ

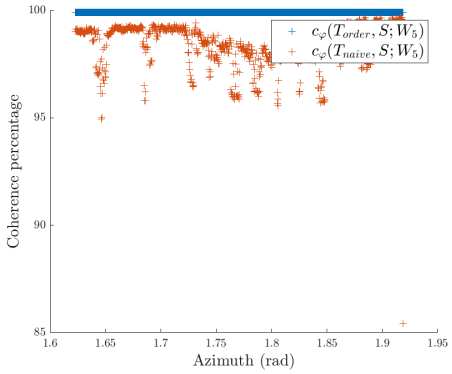

(c) S_3, W_5, φ

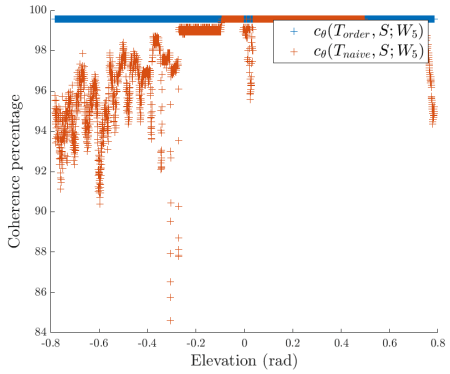

(d) S_3, W_5, θ

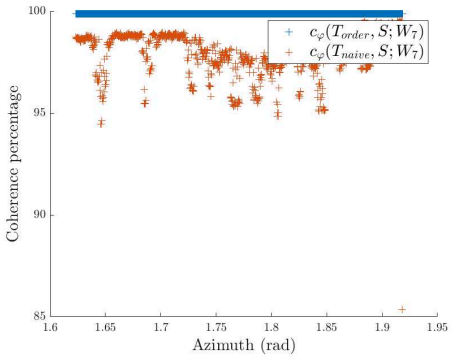

(e) S_3, W_7, φ

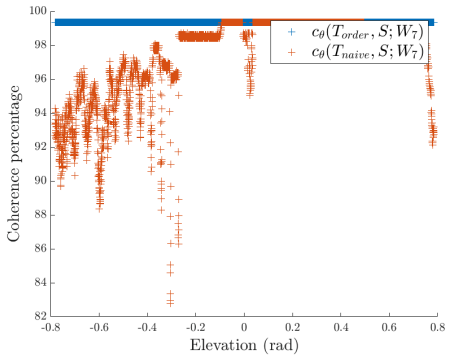

(f) S_3, W_7, θ

Figure 4.11 – Projection coherence for S_4. In blue the coherence of the proposed method, in orange the coherence of the naive method.

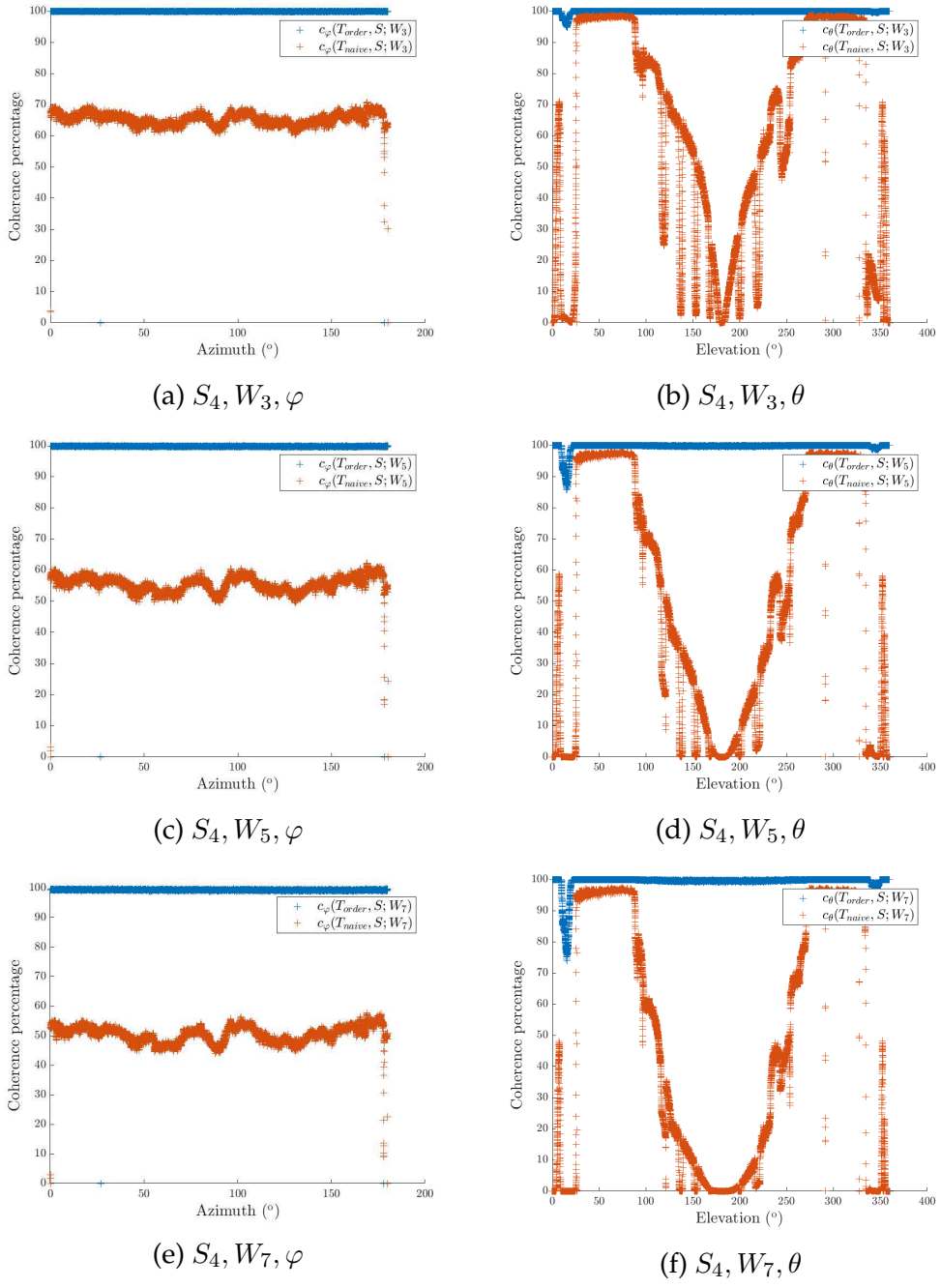

(a) S_4, W_3, φ

(b) S_4, W_3, θ

(c) S_4, W_5, φ

(d) S_4, W_5, θ

(e) S_4, W_7, φ

(f) S_4, W_7, θ

Figure 4.12 – Projection coherence for S_4. In blue the coherence of the proposed method, in orange the coherence of the naive method.

4.4 Discussion and conclusions

In the following section, the viability of the naive and the proposed transformation are discussed. Lossless coefficients and coherence results for the naive transformation (or any transformation relying solely on the elevation and especially azimuth values, e.g. interpolation methods Eysn et al. [2013]) show that, except for the trivial narrow panorama, indoor case of S_3 :

- About 10% of points are randomly lost in all conditions;
- Even on the smallest possible neighbourhood (W_3), coherence drops to 73% in favorable conditions and to 53% in harder scan conditions.

Regarding the loss, the main problem is the fact that the loss is significant and random, meaning that points with critical importance (e.g. edge points in measure application) may be lost, thus tampering with subsequent applications. Coherence results show that the naive projection method is ill suited for any application relying on a local processing (e.g. Liang et al. [2016], Tang et al. [2007]). Indeed, on the smallest neighbourhood, from 27% to 47% of the points will not be computed with meaningful values (true neighbours). If the application relies on a wider neighbourhood (W_7 and wider) most values will be meaningless (from 38% to 72%).

On the other hand the proposed transformation showed good performance in both the lossless property and the coherence :

- About 0.1% of points are lost due to the numerical instabilities filtering;
- The lowest coherence observed was 98.7% on a W_7 neighbourhood, otherwise all coherence were above 99%.

We thus show significant improvements in the fact that, first less points are lost in the transformation process (from 10% to 0.1%) and second the point loss is in a known volume, namely a sphere, centered on the scanner eye and with a radius $R_{threshold}$ ($R_{threshold} = 2\mathrm{cm}$ in our experiments). The point loss being minimal and perfectly localised it does not affect any other processing of the point cloud. The computed image coherence was impacted neither by the scanning conditions (indoor or outdoor), nor by the resolution nor by the neighbourhood size.

The main limitations of our approach is that our algorithm needs the scan to be in acquisition order to work.

To sum up, in this chapter we proposed :

- A theoretical framework for discrete equirectangular projection of LiDAR scans that establishes two core properties for equirectangular projection (lossless and coherence);
- An algorithm to perform an equirectangular projection fulfilling the most important properties previously defined;
- An evaluation framework to quantify how a projection satisfies the lossless and the coherence properties;
- A quantitative comparison between the classic and commonly used transformation and the proposed transformation in various scanning conditions.

We Showed that the classic, naive projection is ill suited when dealing with point clouds with wide elevation panoramas or in outdoor scanning conditions. From now on, all proposed filtering methods will rely on the proposed transformation for image computation.

Chapter 5

Sky and Mixed point filtering

Contents

5.1 Sky noise analysis

In this section we will formally analyse the acquisition of sky points. This will allow us to extract some core properties of the ranges and intensities of sky points.

AMCW Range measurement

Sky noise is produced when an AMCW TLS tries to acquire a point and does not get any return signal. The range and intensity measurement methods are then applied on a random signal, implying a random range and intensity. To characterise the range noise, we must first describe how an AMCW TLS computes its distance. The model presented here is derived from Wang et al. [2016]. To compute the distance the TLS uses the phase-shift method presented 2.1. Although as we have seen, the TLS is then limited to an ambiguity distance R_{max} :

$$R_{max} = \frac{\lambda_m}{2} \tag{5.1}$$

with λ_m the modulation wavelength. The range standard deviation on a normal measure is also proportional to λ_m. To reconcile these two problems the TLS uses several modulation wavelengths. A short wavelengths for precision and several longer wavelengths to lift the ambiguity (or *unwrap* the phase) on the short wavelength measurement. The model presented in Wang et al. [2016] uses 3 wavelengths, we will here do the same. The following notations will be used :

- λ_{m0} the longest modulation wavelength
- λ_{m1} the intermediate modulation wavelength
- λ_{m2} the shortest modulation wavelength
- ϕ_0 phase measurement with λ_{m0}
- ϕ_1 phase measurement with λ_{m1}
- ϕ_2 phase measurement with λ_{m2}
- n_1 the unwrap number for λ_{m1}
- n_2 the unwrap number for λ_{m2}
- R the measured distance

Considering the phase unwrapping procedure the distance is given by :

$$R = \frac{\lambda_{m2}}{2}\left(\frac{\phi_2}{\tau} + n_2\right) \tag{5.2}$$

To compute the unwrap numbers we consider the following equations :

$$\frac{\lambda_{m0}}{2}\frac{\phi_0}{\tau} = \frac{\lambda_{m1}}{2}\left(\frac{\phi_1}{\tau} + n_1\right) \tag{5.3}$$

$$\frac{\lambda_{m1}}{2}\left(\frac{\phi_1}{\tau} + n_1\right) = \frac{\lambda_{m2}}{2}\left(\frac{\phi_2}{\tau} + n_2\right) \tag{5.4}$$

which yields :

$$n_1 = \left\lfloor \frac{\lambda_{m0}}{\lambda_{m1}}\frac{\phi_0}{\tau} - \frac{\phi_1}{\tau} \right\rfloor \tag{5.5}$$

$$n_2 = \left\lfloor \frac{\lambda_{m1}}{\lambda_{m2}}\left(\frac{\phi_1}{\tau} + n_1\right) - \frac{\phi_2}{\tau} \right\rfloor \tag{5.6}$$

where $\lfloor x \rfloor$ is the closest integer inferior to x.

We must now discuss how the phase is measured. Let $s(t)$ be the sent intensity signal and $r(t)$ be the reflected signal measured by the TLS. The sent signal is a cosine with a an amplitude a and pulsation $\omega = \frac{2\pi c}{\lambda_m}$:

$$s(t) = a\cos(\omega t) \tag{5.7}$$

In the case of a non altered measure, the received signal is a cosine with amplitude A, offset B, pulsation $\omega = \frac{2\pi c}{\lambda_m}$ and phase ϕ:

$$r(t) = B + A\cos(\omega t - \phi) \tag{5.8}$$

The four buckets methods consists in computing the cross-correlation $C(x)$ and using four samples of C to estimate ϕ, A and B. The cross-correlation between $s(t)$ and $r(t)$ is given by :

$$C(x) = \lim_{p\to\infty}\frac{1}{p}\int_{-\frac{p}{2}}^{\frac{p}{2}} s(t)r(t+x)dt \tag{5.9}$$

For a non altered measure we have :

$$C(x) = \frac{aA}{2}\cos(\omega x + \phi) + B \tag{5.10}$$

Or equivalently with $\psi = \omega x$;

$$C(\psi) = \frac{aA}{2}\cos(\psi + \phi) + B \tag{5.11}$$

Finally with four equidistant samples of C, at ψ_1, ψ_2, ψ_3 and ψ_4 where $\psi_i = (i-1)\frac{\tau}{4}$ (i.e. $C_1 = C(0)$, $C_2 = C\left(\frac{\tau}{4}\right)$, $C_3 = C\left(\frac{\tau}{2}\right)$, $C_4 = C\left(\frac{3\tau}{4}\right)$) we have :

$$\phi = \arctan2(C_4 - C_2, C_1 - C_3) \tag{5.12}$$

$$A = \frac{1}{2a}\sqrt{(C_3 - C_1)^2 + (C_0 - C_2)^2} \tag{5.13}$$

$$B = \frac{1}{4}(C_0 + C_1 + C_2 + C_4) \tag{5.14}$$

and :

$$\arctan2 : \mathbb{R} \to [0, \tau] \tag{5.15}$$

$$(y, x) \mapsto \begin{cases} \arctan\left(\frac{y}{x}\right) \text{ if } x > 0, y > 0 \\ \arctan\left(\frac{y}{x}\right) + \tau \text{ if } x > 0, y < 0 \\ \arctan\left(\frac{y}{x}\right) + \frac{\tau}{2} \text{ if } x < 0, y > 0 \\ \arctan\left(\frac{y}{x}\right) + \frac{\tau}{2} \text{ if } x < 0, y < 0 \end{cases} \tag{5.16}$$

The full range measurement procedure is summarised in Frame 5.1.

We will see in the following section how this procedure influences ϕ and R if $r(t)$ is a random signal.

Frame 5.1 – Range measurement procedure

For a single range measurement, the TLS :

1. measures a received signal $r(t)$ for several time periods T ($T = \frac{\lambda_m}{c}$),
2. estimates the cross-correlation between $r(t)$ and $s(t)$ the sent signal,
3. samples the cross-correlation function at four equidistant points ψ_1, ψ_2, ψ_3 and ψ_4 where $\psi_i = (i-1)\frac{\tau}{4}$,
4. computes ϕ with Equation (5.12),
5. repeats steps 1 through 4 for all modulation wavelengths,
6. computes the range R with Equations (5.5), (5.6) and (5.2).

Sky range noise

During the acquisition of a sky point the TLS is only receiving background radiation. The background radiation is a random process $X(t)$ that we will consider stationary (it keeps the same probability distribution at all time) and with finite variance i.e. :

$$\forall (t_1, t_2), f_{X(t_1)} = f_{X(t_2)} \tag{5.17}$$

$$\forall t,\ \text{var}\left[X(t)\right] = E\left[\left(X(t) - E[X(t)]\right)^2\right] < \infty \tag{5.18}$$

$$E[X] = \int_{\mathbb{R}} x f_X(x)\, dx \tag{5.19}$$

where f_V is the probability density function of the random variable V and $E[V]$ is the expected value of the r.v (random variable) V. This assumption is perfectly valid since a sky point is acquired by measuring background radiation in a single direction and for a very short time. We will denote the probability density function describing $X(t)$ as f_X, $E[X(t)]$ as μ .

Following the measurement chain presented in Frame 5.1 up to step 4 with $X(t)$ as its input ($r(t) = X(t)$), I found a core property of the sky noise. This property is presented in Theorem 3, where Φ is the random variable representing the measured phase and $\mathcal{U}(a, b)$ the uniform distribution between a and b.

Theorem 3. ***Phase distribution theorem***
$r(t)$ is a stationary random process with finite variance $\implies \Phi \sim \mathcal{U}(0, \tau)$

The proof being seven pages long, it is given in Appendix A.2. Note that Theorem 3 implies that, in the case of an acquisition from background radiation (or a signal with very bad signal to noise ratio), the range distribution is independent of the noise characteristics.

We can now use Theorem 3 to simulate an acquisition of sky points. We acquired the sky range distribution in a manually cropped scan. The reference distribution was approximated with the normalised histogram computed from approximately 27 million points in 377 bins. The bin number was found using Terrell's rule (Terrell and Scott [1985]) i.e. $n_{bins} = \lfloor \sqrt[3]{2N_{data}} \rfloor$, N_{data} the number of data points used to compute the histogram. The distribution of the simulated range will then be compared to the reference range distribution.

The application of Theorem 3 yields :

$$\Phi_0 \sim \mathcal{U}(0, \tau) \tag{5.20}$$
$$\Phi_1 \sim \mathcal{U}(0, \tau) \tag{5.21}$$
$$\Phi_2 \sim \mathcal{U}(0, \tau) \tag{5.22}$$

Then if $\mathcal{R}$ denotes the measured range random variable, we have :

$$\mathcal{R} = \frac{\lambda_{m2}}{2}\left(\frac{\Phi_2}{\tau} + \left\lfloor \frac{\lambda_{m1}}{\lambda_{m2}}\left(\frac{\Phi_1}{\tau} + \left\lfloor \frac{\lambda_{m0}}{\lambda_{m1}}\frac{\Phi_0}{\tau} - \frac{\Phi_1}{\tau}\right\rfloor\right) - \frac{\Phi_2}{\tau}\right\rfloor\right) \tag{5.23}$$

The TLS modulation wavelengths were extracted by measuring some point cloud features. The longest wavelength λ_{m0} can be estimated as the maximal measured length divided by 2. Then if $(R_i)_{i\in[1,N_{data}]}$ is the set of measured distances :

$$\hat{\lambda}_{m0} = 2 \max_i(R_i) \tag{5.24}$$

The shortest wavelength can be estimated by analysing some mixed point measurements. Indeed looking at Equation (5.2) shows that noisy distance measurement may exhibit sudden $\frac{\lambda_{m2}}{2}$ jumps. Such jumps were

manually measured in some scans and if R_{jump} is the jump distance, we have :

$$\hat{\lambda}_{m2} = 2R_{jump} \tag{5.25}$$

Finally, analysing Equation (5.23) reveals that the minimum possible value for $\mathcal{R}$, $\mathcal{R}_{min}$ is :

$$\mathcal{R}_{min} = -\frac{\lambda_{m1} + \lambda_{m2}}{2} \tag{5.26}$$

Then if R_{min} is the minimum measured distance, λ_{m1} can be estimated by Equation (5.27).

$$\hat{\lambda}_{m1} = -2R_{min} - \hat{\lambda}_{m2} \tag{5.27}$$

Although as we'll see later, this method needs to be slightly adjusted because of the way the TLS deals with negative range (the method still relies on the same property).

For our TLS, a Leica HDS6100, the estimations yielded :

$$\begin{aligned}\lambda_{m0} &= 158m \\ \lambda_{m1} &= 15m \\ \lambda_{m2} &= 1.44m\end{aligned}$$

We produced 6697830 samples of Φ_0, Φ_1 and Φ_2 to compute the same number of samples of $\mathcal{R}$ from Equation (5.23). That number of samples was chosen to have the same number of bins as the reference histogram.

We present Figure 5.1 the observed distribution and the simulated range distribution.

As we can see in Figure 5.1, the simulated and observed distributions are perfectly matching for $R > 8m$. The discrepancy can be explained by the fact that Equation (5.23) can yield negative values, which is incompatible as a range value. To correct it, we suppose that the TLS adds $\mathcal{R}_{min}$ to any negative range value computed. Considering this procedure, λ_{m1} can be estimated using R_p, the most probable range value.

$$\hat{\lambda}_{m1} = 2R_p - \hat{\lambda}_{m2} \tag{5.28}$$

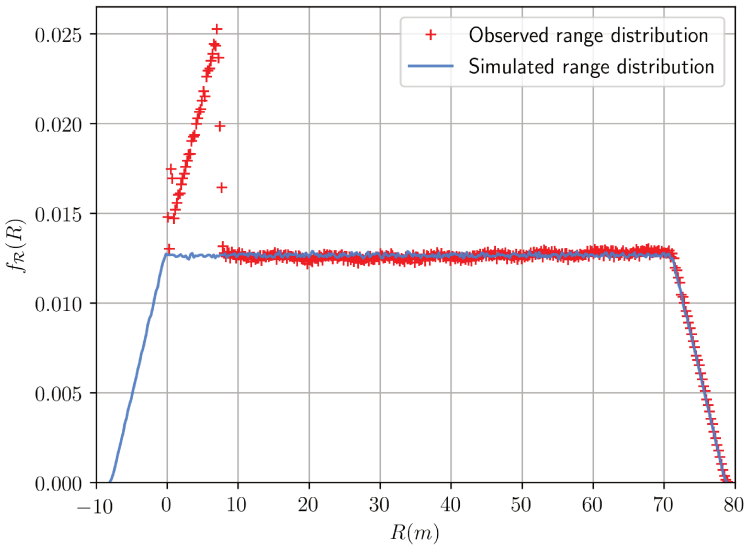

Figure 5.1 – Observed sky range distribution in red and Simulated range distribution in blue.

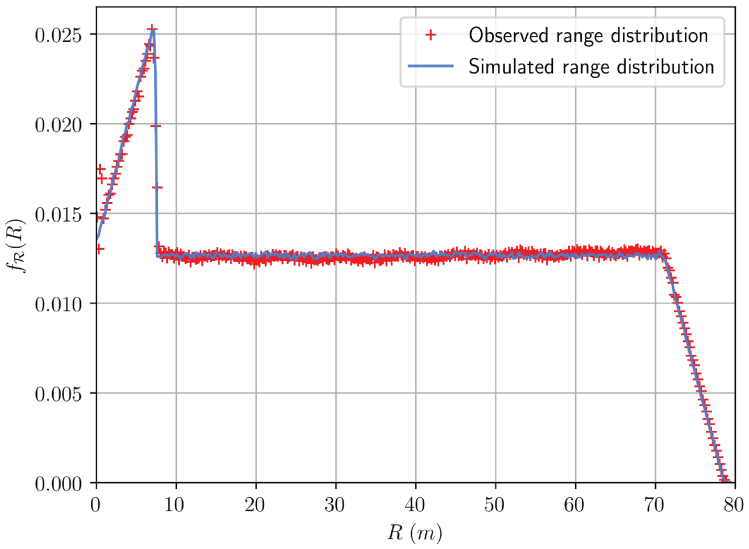

Figure 5.2 – Observed sky range distribution in red and Simulated range distribution in blue. Here the negative range correction procedure was used.

Also, recomputing the simulated range distribution with the negative range correction yields the distribution shown Figure 5.2.

Using this correction procedure yields exactly the observed distribution. As we have seen, Theorem 3 allowed us to simulate a range acquisition with the same distribution. Finally all these evidences allows us to conclude that the sky range noise distribution is independent from the background radiation characteristics.

5.2 Sky noise detection

Two properties of the sky noise oriented the conception of the sky detector. First, any sky point is recorded from a diffuse illumination signal and any correctly recorded point will receive this diffuse component on top of the energy from the return signal, making the sky points the lowest intensity returns in the scan. Second, as we have seen in Section 5.1 the range produced by a sky noise acquisition is not influenced by the illumination characteristics but only by the scanner modulation wavelengths. The sky range distribution has very high variance (in our case about $500m^2$) and most probably some of the highest in the scan. Indeed let's consider a set R_d of n points where one half is at a distance R and the other half at a distance $R+d$ (making it the highest variance configuration for such distances). The empirical range variance of this set of points is given Equation (5.29).

$$\mathrm{var}(R_d) = \frac{n}{n-1}\frac{d^2}{4} \tag{5.29}$$

As we can see in Equation (5.29) the empirical variance of these points will only get to the same order of magnitude as the sky range variance for range transition of about $20m$ ($d \geq 20$) which are expected to be uncommon.

Filtering principle

To detect sky points independently the previously computed range and intensity maps were used using the method described in Chapter 4. First, based on the local range variance, a partial sky detection was performed to estimate a sky intensity profile. Then an intensity threshold was computed using the intensity profile. Finally the sky was identified as all points with an intensity lower than the computed threshold.

For each pixel p in the range map R_{map} local variance was computed by taking a square window centred on p with side w, noted $W(p)$, and associating to p the unbiased empirical variance of the range values $R_{map}(p_i)$ of non empty pixels contained in $W(p)$:

$$\text{var}(p) = \frac{1}{N_W(p) - 1} \sum_{p_i \in W(p)} \left(R_{map}(p_i) - \frac{1}{N_W(p)} \sum_{p_j \in W(p)} R_{map}(p_j) \right) \quad (5.30)$$

With $N_W(p)$ the number of scan points mapped to a pixel in $W(p)$. Note that $N_W(p)$ was used instead of w^2 to ignore empty pixels in the range image, caused by the discarded points. Note that, for a given point class (i.e. points at a given range with a given surface noise, sky points, etc) the distribution of the empirical variance of that class will tend toward a χ^2 distribution. As shown by Jouini et al. [2011], χ^2 distributions are well approximated by Log-Normal distributions. From this, computing the distribution of the log variance will yield a mixture of Gaussian where the Gaussian with the highest mean log variance will represent the sky range variance.

The log variance distribution was approximated by computing the histogram of the computed log variance values using the Terell-Scott rule (Terrell and Scott [1985]) (the number of bins $n_{bins} = \lfloor \sqrt[3]{2N_{data}} \rfloor$).

A first sky detection was performed by thresholding the variance map with the log variance at which the mode of highest log variance was found (see Figure 5.3 for an example).

The sky intensity distribution was estimated with the intensity histogram, H_I, of the previously detected sky (example Figure 5.4).

An intensity threshold, T_I, was computed from the cumulative intensity histogram S_{H_I} :

$$S_{H_I}(I) = \sum_{x<I} H_I(x) \quad (5.31)$$

T_I satisfies : $S_{H_I}(T_I) = \rho_{sky} N_{detected}$ with $N_{detected}$ the number of points detected with the variance threshold and ρ_{sky} a user defined parameter used to filter non sky intensities. A second detection is performed by thresholding the intensity image and labelling as sky all pixels with an intensity inferior to T_I

At this point a few sparse undetected sky points were expected. Missing sky points are detected with a w by w sliding window. For each

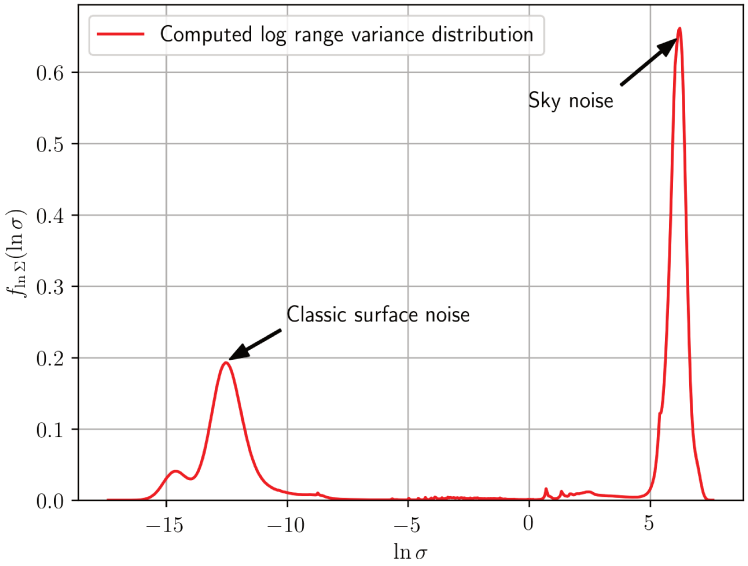

Figure 5.3 – Estimated range log variance distribution. Here $\ln\Sigma$ denotes the range log variance random variable.

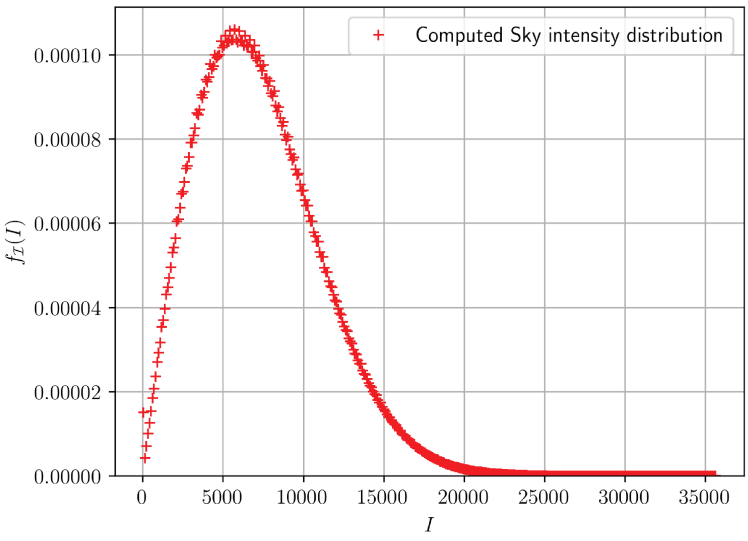

Figure 5.4 – Estimated intensity distribution. Here $\mathcal{I}$ denotes the sky intensity random variable.

undetected pixel p in the sky image, if more than half of the window surrounding p were labelled as sky then p labelled as sky. This process was repeated until less than $\frac{N_{map}}{1000}$ new sky points were detected.

5.3 Mixed point detection

We built our detector on the range map R_{map} using a w by w pixel sliding window, with w a user defined parameter. For each pixel p of R_{map} and each window size s ($s \in [3, w]$, s odd), the angles $\beta_{jk,lm}$ between the laser beam direction at P (3D point mapped at p) and the normal to the triangles formed by P and two 3D points, $P_{j,k}$ and $P_{l,m}$ mapped to two chosen neighbours of p, $p_{j,k}$ and $p_{l,m}$ were computed. Neighbours were taken in order while circulating clockwise on the s sized window border (see Figure 5.5 for a visual representation). Let $P = (R, \theta, \varphi, I)$ be mapped to the pixel p at coordinates (u, v), $P_{j,k} = (R_{j,k}, \theta_{j,k}, \varphi_{j,k}, I_{j,k})$ and $P_{l,m} = (R_{l,m}, \theta_{l,m}, \varphi_{l,m}, I_{l,m})$ be mapped respectively to $p_{j,k}$ and $p_{l,m}$ at coordinates $(u+j, v+k)$ and $(u+l, v+m)$, $(j, k, l, m) \in \mathbb{Z}^4$. We have, with a perfect scanner sampling :

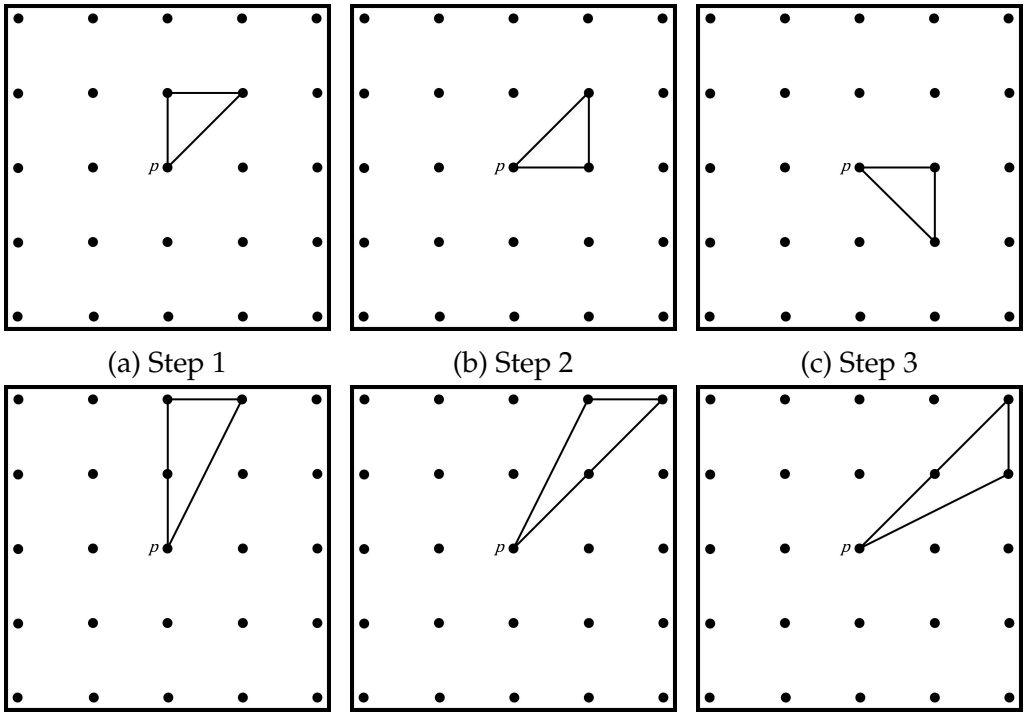

(a) Step 1 (b) Step 2 (c) Step 3

(d) Step 9 (e) Step 10 (f) Step 11

Figure 5.5 – Neighbour choice for the mixed point detector with $w = 5$. The first 8 steps focus on the 3 by 3 window then the remaining 16 steps focus on the 5 by 5 window border.

$$P = R \begin{pmatrix} \cos\theta\,\cos\varphi \\ \cos\theta\,\sin\varphi \\ \sin\theta \end{pmatrix} = R\overrightarrow{u_0} \tag{5.32}$$

$$P_{j,k} = R_{j,k} \begin{pmatrix} \cos(\theta + j\delta)\ \cos(\varphi + k\delta) \\ \cos(\theta + j\delta)\ \sin(\varphi + k\delta) \\ \sin(\theta + j\delta) \end{pmatrix} \tag{5.33}$$

By keeping the 1^{st} order term of the Taylor expansion :

$$P_{j,k} = R_{j,k}\left(\overrightarrow{u_0} + j\delta\overrightarrow{u_1} + k\delta\overrightarrow{u_2}\right) \tag{5.34}$$

With :

$$\overrightarrow{u_1} = \begin{pmatrix} -\sin\theta\,\cos\varphi \\ \sin\theta\,\sin\varphi \\ \cos\theta \end{pmatrix} \tag{5.35}$$

$$\overrightarrow{u_2} = \begin{pmatrix} -\cos\theta\,\sin\varphi \\ \cos\theta\,\cos\varphi \\ 0 \end{pmatrix} \tag{5.36}$$

The angle $\beta_{jk,lm}$ is given by :

$$\cos(\beta_{jk,lm}) = \frac{(P_{j,k} - P) \wedge (P_{l,m} - P)}{\left\|(P_{j,k} - P) \wedge (P_{l,m} - P)\right\|} \cdot \frac{P}{\|P\|} \tag{5.37}$$

Where $\wedge$ is the cross product and $\cdot$ the dot product.
Let :

$$d_{j,k} = R_{j,k} - R \tag{5.38}$$

$$A = \delta\left(l d_{j,k} R_{l,m} - j d_{l,m} R_{j,k}\right) \tag{5.39}$$

$$B = \delta\left(m d_{j,k} R_{l,m} - k d_{l,m} R_{j,k}\right)\cos\theta \tag{5.40}$$

$$C = \delta_{TLS}^2 R_{j,k} R_{l,m}\,(jm - kl)\cos\theta \tag{5.41}$$

By inserting (5.34) in (5.37) we have :

$$\cos\left(\beta_{jk,lm}\right) = \frac{C}{\sqrt{A^2 + B^2 + C^2}} \tag{5.42}$$

We thus expressed $\beta_{jk,lm}$ independently of the azimuth under the condition that the angular sampling is perfect, which is almost true for the elevation. All the $\beta_{jk,lm}$ values were computed following (5.42). The pixel p was classified as mixed point if more than half of the $w^2 - 1$ computed angle values were above a user defined threshold $\beta_{threshold}$.

5.4 Discussion and conclusions

In this section we presented an analysis for sky noise, exhibiting its core property presented in Theorem 3 which can be summarized as : The measured phase will follow a uniform distribution in $[0, \tau]$ whatever the properties of the random input signal (e.g. distribution, mean, variance etc.) as long as this signal is stationary and with finite variance. This property has several interesting implications, for example, since the range is only dependant on the measured phases and the modulation wavelengths, then the range noise distribution is only dependant on the modulation wavelengths. Also since it only relies on the fact that the input signal is stationary and with finite variance and on the fact that the device uses the four buckets methods, it can be applied to other devices, e.g. a TOF camera. This theorem is supported by a proof presented in Appendix A.2 and solid experimental evidence where it allowed to simulate a range distribution that matches perfectly with the observed distribution.

From the discovered properties of the sky noise we designed a detector with two parameters w, a window size and ρ_{sky} the fraction of the sky distribution to keep. Higher window parameter allows to have a better defined sky log variance mode but fewer points will be detected for the intensity distribution estimation. Since the variance mode is clearly defined even for low w values, we advice to use low w values to maximise the number of detected points for the intensity distribution estimation. Higher ρ_{sky} allow for better detection with a higher chance of false positives (since higher ρ_{sky} imply a higher intensity threshold value).

Based on the detector proposed by Tang et al. [2007] we designed a new mixed point detector using a wider neighbourhood for more robustness

with two parameters : w,a window size and $\beta_{threshold}$ a threshold angle value. Higher window parameter allows the use of more triangles for mixed point detection allowing more robustness, however it also reduces the detector resolution, i.e. the size of the smallest, non noisy, object it can classify has non noise. The detector resolution $\delta_{detector}$ (in pixel size) can be easily deduced from the detector principle : $\delta_{detector} = \frac{w}{2}$. Indeed, if a given object takes less than half the window, it will necessarily be classified as noise since less than half of the triangle will even be on the object. The second detector parameter $\beta_{threshold}$ will control the detector capacity to correctly label points. Lower $\beta_{threshold}$ will allow for more noise detection with a higher risk of false detection and higher $\beta_{threshold}$ will allow for lower risk of false detection with higher risk of non detection of noise.

Chapter 6

Detection evaluation in controlled conditions

Contents

6.1 Experimental setup

Material

Experiments were conducted on scans taken with a phase-based Leica HDS6100. It scans using a red laser with a wavelength between 650nm and 690 nm Kaasalainen et al. [2011] with an angular resolution ranging from 5000 pts/turn ($2\pi 10^{-4}$ rad, resolution "L" - low) to 40000 pts/turn ($\frac{\pi}{2}10^{-4}$ rad, resolution "U" - ultra high). In these experiments scans were taken using the ultra resolution and subsampled (using the equirectangular projection) to every other resolution accessible to the Leica HDS6100 (see table 6.1). The targets used in our experimental setup were made with Canson paper sheets and their reflectivities were measured with a Spectral evolution SM-2500 manufactured by Spectral Evolution.

Two different setups were used considering the parameters driving the noise patterns (see table 2). The sky noise detector evaluation was performed on scans taken outdoor, on a rooftop to have purely sky noise and the mixed point detector performance was assessed on scans taken indoor to avoid sky noise influence. The chosen reflectivities cover a wide range of applications, with low reflectivities (green and brown paper, showing refelctivities of 9% and 21%) common to forestry applications and high refelectivy (white paper at 94% albedo) for civil engineering applications. Scanning ranges go from close range (9m) to mid range (about 30m) again common in forestry and civil engineering applications. The acquisitions parameters (distance to the scanner, incidence angle on the targets etc) are summed up in table 6.2 and 6.3.

Resolution	U - Ultra	H - High	M - Medium	L - Low
Angular sampling (fraction of 2π)	$\frac{1}{4}10^{-4}$	$\frac{1}{2}10^{-4}$	10^{-4}	2.10^{-4}
Points per revolution	40000	20000	10000	5000

Table 6.1 – Resolution table

Experimental procedure

Each outdoor resp. indoor setup was filtered with the sky resp. mixed-point filter with different sets of filters parameters presented in table 6.4.

Shape	Cylinder	Circular hole
Diameters (mm)	21.5, 36, 68, 105, 250	40, 90, 230, 480
Color (albedo % at 670nm)	white (94), brown (21), green (9)	

Table 6.2 – Target parameters

Type	Indoor	Outdoor
Distance from scanner to setup (m)	9, 16, 21, 27	9, 15, 21, 27
Distance from first target to second target (m)	1, 2, 3, 4, 5	N/A
Incidence angle on the first target (fraction of 2π)	N/A	0, $\frac{1}{12}$, $\frac{1}{8}$

Table 6.3 – Acquisition parameters

Sky filter parameters	W	3, 5, 7, 9, 11, 13, 15
	ρ_{sky} (%)	10, 20, 30, 40, 50, 60, 70, 80, 85, 90, 91, 92, 93, 94, 95, 96, 97, 98, 99, 100
Mixed-point filter parameters	W	3, 5, 7, 9, 11, 13, 15
	$\beta_{threshold}$ (^{o})	20, 40, 60, 70, 75, 80, 81, 82 83, 84, 85, 86, 87, 88, 89, 90

Table 6.4 – Filter parameters tested

In each filtered scan, were evaluated : the diameter, in pixel in the equirectagular image, of the hole or cylinder and the number of *true positives*, *false positives*, *true negatives* and *false negatives* (details on their definition in table 6.5). Pixel size was chosen for the analysis since it is a more adapted measure to assess the filter performance. Indeed, a 1m diameter cylinder at 10m will have the same pixel diameter in the image than a 2m diameter cylinder at 20m. From the measured and estimated diameters a linear regression analysis was carried to assess the global performance of each parameter. The *true positives*, *false positives*, *true negatives* and *false negatives* were used to compute the *true positive rates* (or *sensitivity*) and the *false positive rate* (or *fall-out*) for a **Receiver Operating Characteristic** analysis. Both analysis will be detailed in the following sections.

		Reference	
		Valid	Noise
Filter Result	Valid	True negative	False negative
	Noise	False positive	True positive

Table 6.5 – Definitions of *true positives*, *false positives*, *true negatives* and *false negatives*

6.2 Reference construction

Filter performance were evaluated against reference labelled scans. The usual approach is to have an expert label the scans based on visual inspection. The proposed analysis was based on semi-automatically generated references and automatic labelling based on a footprint model. This evaluation provided an objective framework to assess filter performance. In this section the reference construction methods will be described followed by the footprint model description.

Cylinder references

All cylinders were recreated in each scene by first manually extracting them separately. Then, each cylinder axis was computed thanks to a PCA. For each color slice, the cylinder points were projected on a plane perpendicular to the cylinder axis. Points that were not obviously on the cylinder were then manually discarded. The position of a circle, with its radius constrained to be equal to the measured radius, was optimised to minimise the distance with the projected points (least square geometric fit with constrained radius). The circle positions for each color slice were manually adjusted and the filtering was revised until the centers alignment error with the cylinder axis (meaning the distance between the centers and their projection on the cylinder axis) was below 10^{-4}m for all centers. Finally the centers were projected on the cylinder axis to yield their final position.

Hole references

Each circle with its frame was manually extracted. An arbitrary over filtered version on each circle was selected to fit a plane corresponding to the wood board for that hole (note that the plane was not fitted on the whole board since it was not perfectly flat). The references were done man-

ually, using 3DReshaper, by placing on the scan a circle with a fixed radius, equal to the real radius measured on the setup. The placement was done to minimise the maximum intensity inside the circle. Indeed, as stated in section 5.2, sky noise should correspond to the lowest observed intensities, or more specifically, any intensity recorded on the board should be lower than an intensity recorded entirely or partially in the sky. Note that the projection on the plane was done following the scans directions, thus the projection $P' = (R', \theta', \varphi')$ of a point $P = (R, \theta, \varphi)$ on a plane Π is given by :

$$\Pi : y = a_\Pi x + b_\Pi z + c_\Pi \tag{6.1}$$

$$\theta' = \theta \tag{6.2}$$

$$\varphi' = \varphi \tag{6.3}$$

$$R' = \frac{c_\Pi}{\cos(\theta)\sin(\varphi) - a_\Pi \cos(\theta)\cos(\varphi) - b_\Pi \sin(\theta)} \tag{6.4}$$

Footprint model

To correctly evaluate the filters, the reference shapes were recreated in the scans and raw scan point were labelled as non noisy, sky noise and mixed point noise depending on their position. A point was labelled as non noisy if, considering its acquisition direction, the laser footprint was integrally formed on the cylinder, rectangle or the holes frame depending on the case. A point was labelled as sky noise if the laser footprint was integrally lost in the sky. Finally a point was labelled as mixed point noise if the footprint lied partially on the considered object. To calculate the angular size of the mixed point noise zone, the laser was modelled as a Gaussian beam. Beam waist size, w_0 (smallest footprint radius across the beam) and collimation distance R_{w_0} (distance were the footprint radius equals the waist) are usually not provided in the LiDAR datasheets. Equations were thus derived to compute them from a footprint radii measures at different distances. At least three measures are required, in our case a measure at $R = 1\text{m}$, $R = 25\text{m}$ and $R = 50\text{m}$ were provided in the datasheet. The equation of the footprint radius w as a function of distance from the laser exit is given by :

$$w(R) = w_0 \sqrt{1 + \left(\frac{\lambda (R - R_{w_0})}{\pi w_0^2} \right)^2} \tag{6.5}$$

With λ the laser wavelength. Equivalently :

$$w^2(R) = w_0^2 + \frac{\lambda^2}{\pi^2 w_0^2} R_{w_0}^2 - 2\frac{\lambda^2}{\pi^2 w_0^2} R_{w_0} R + \frac{\lambda^2}{\pi^2 w_0^2} R^2 \tag{6.6}$$

Let :

$$A = \frac{\lambda^2}{\pi^2 w_0^2} \tag{6.7}$$

$$B = -2\frac{\lambda^2}{\pi^2 w_0^2} R_{w_0} \tag{6.8}$$

$$C = w_0^2 + \frac{\lambda^2}{\pi^2 w_0^2} R_{w_0}^2 \tag{6.9}$$

And w_k be the k^{th} observation of the footprint radius at distance R_k, then :

$$\begin{pmatrix} w_0^2 \\ \vdots \\ w_n^2 \end{pmatrix} = \begin{pmatrix} R_0^2 & R_0 & 1 \\ \vdots & \vdots & \vdots \\ R_n^2 & R_n & 1 \end{pmatrix} \begin{pmatrix} A \\ B \\ C \end{pmatrix} \tag{6.10}$$

And :

$$\begin{pmatrix} A \\ B \\ C \end{pmatrix} = \begin{pmatrix} R_0^2 & R_0 & 1 \\ \vdots & \vdots & \vdots \\ R_n^2 & R_n & 1 \end{pmatrix}^{\dagger} \begin{pmatrix} w_0^2 \\ \vdots \\ w_n^2 \end{pmatrix} \tag{6.11}$$

Where $M^{\dagger} = \left(M^T M\right)^{-1} M^T$ is the pseudo-inverse of M.
Finally :

$$w_0 = \frac{\lambda}{\pi\sqrt{A}} \tag{6.12}$$

$$R_{w_0} = -\frac{B}{2\sqrt{A}} \tag{6.13}$$

Then consider the laser beam pointing towards a straight edge at a distance R (meaning that the beam center line and the edge line are

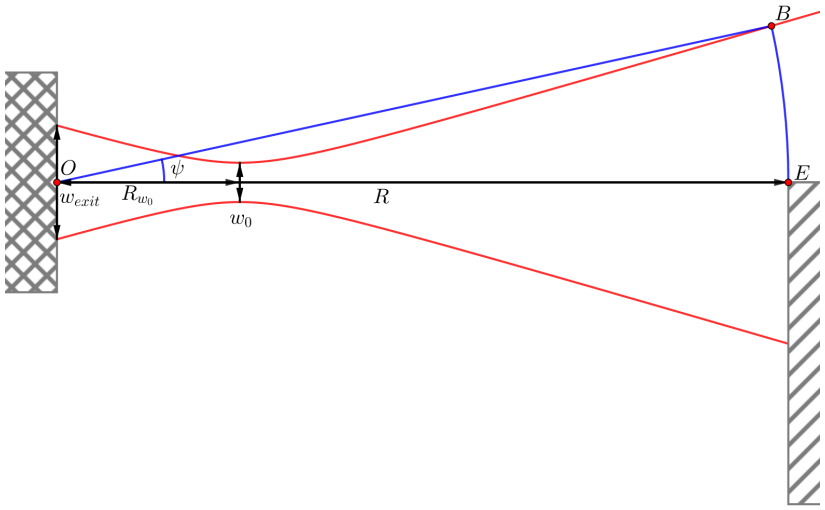

Figure 6.1 – Gaussian laser beam model.

secant), and let ψ be the minimal angle the scanner needs to turn in any direction (even not accessible to the laser) to have the laser footprint not formed on the edge at all, here after called the *unconstrained angular edge loss* (figures 6.1, 6.2), then :

$$R \sin \psi = w_0 \sqrt{1 + \left(\frac{\lambda \left(R \cos \psi - R_{w_0} \right)}{\pi {w_0}^2} \right)^2} \tag{6.14}$$

Solving equation (6.14) for ψ yields (details given in Appendix A.3) :

$$\cos \psi = \frac{K^2 R_{w_0} + \sqrt{K^4 R_{w_0}^2 + (1 + K^2) \left(R^2 - {w_0}^2 - K^2 R_{w_0}^2 \right)}}{(1 + K^2) R} \tag{6.15}$$

$$K = \frac{\lambda}{\pi w_0} \tag{6.16}$$

To estimate the edge loss the real sampling pattern or the LiDAR must be accounted for. It follows a spherical, regular and discrete angular sampling. Then the loss can be more easily expressed in terms of "angular loss" or number of points that would be acquired as mixed points while rotating from the edge in the azimuthal or zenithal directions. Considering this direction restriction, the loss is conditioned by the angle γ the edge

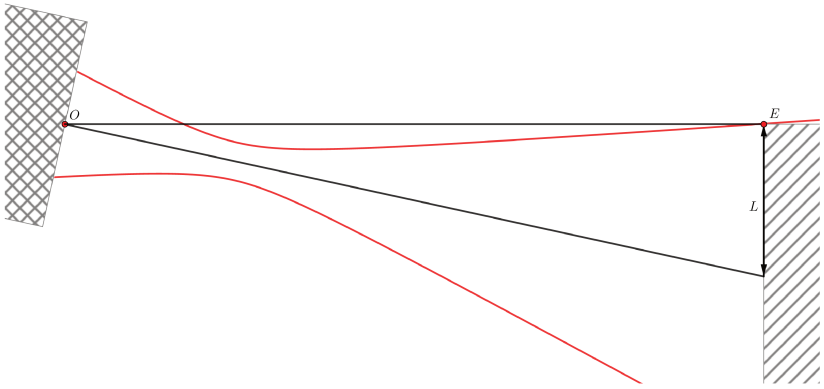

Figure 6.2 – Gaussian laser beam model, derived edge loss

makes with the sampling grid. Let $\vec{e}$ be the unit vector tangent to the edge at the considered point, $\vec{a} = (\cos\theta\cos\varphi \quad \cos\theta\sin\varphi \quad \sin\theta)^T$ the aiming vector (unit vector from the origin to the considered point) and $\vec{a_\theta} = (-\sin\theta\cos\varphi \quad \sin\theta\sin\varphi \quad \cos\theta)^T$ the local orthogonal unit vector in the direction of increasing θ, then :

$$\gamma = \arccos\left(\frac{\vec{a_\theta}\cdot(\vec{a}\wedge(\vec{e}\wedge\vec{a}))}{\sin(\arccos(\vec{e}\cdot\vec{a}))}\right) \tag{6.17}$$

Projecting the unconstrained angular edge loss onto the sampling grid yields the *zenithal angular edge loss* ψ_θ and the *azimuthal angular edge loss* ψ_φ :

$$\psi_\theta = \delta\left\lceil\frac{1}{\delta}\arctan(\tan(\psi)\cos(\gamma))\right\rceil \tag{6.18}$$

$$\psi_\varphi = \delta_\varphi\left\lceil\frac{1}{\delta_\varphi}\arctan(\tan(\psi)\sin(\gamma))\right\rceil \tag{6.19}$$

$$\delta_\varphi = \arccos\left(\cos(\theta)^2\cos(\delta)+\sin(\theta)^2\right) \tag{6.20}$$

With δ_φ the *adjusted azimuthal resolution*, the angle between a point at coordinates (R,θ,φ) and a point at coordinates $(R,\theta,\varphi+\delta)$:

Finally the edge loss L is :

$$L = R\sqrt{\tan\left(\psi_\theta\right)^2 + \tan\left(\psi_\varphi\right)^2} \tag{6.21}$$

6.3 Result extraction and analysis

The goal being to evaluate the filter performance, the methods chosen to compute diameters must not be robust against under or over filtering and outliers. In this section will be described the methods used to compute the results and the analysis carried on the extracted values.

Result extraction

Cylinder diameters

All diameter measures were converted in pixel size for this analysis. To compute pixel sizes, angular size must be evaluated first. Given a cylinder of radius r, its angular size α at a distance R is given by :

$$\alpha = 2\arcsin\left(\frac{r}{r+R}\right) \tag{6.22}$$

Any angular size α can be converted in a pixel diameter d_{pixel}, representing the number of pixels occupied this diameter represents in the equirectangular map :

$$d_{pixel} = \left\lfloor \frac{\alpha}{\delta} \right\rfloor \tag{6.23}$$

Considering the objective of each filter, i.e. filtering all mixed points for the mix point filter and filtering all the sky points for the sky filter, suiting target pixel diameters values must be computed. Due to the edge loss effect, target diameters will be slightly lower, resp. higher, for the mixed-point, resp. sky, filter than the real diameter. Diameters are reduced in the mixed point case, since if all mixed point are removed, the diameter will be shortened by $2L$, with L defined in equation (6.21). In angular measurement, if α_- is the angular span where the footprint can entirely be formed on the cylinder for a cylinder of radius r at distance R and d^-_{pixel}, its pixel converted measure, we have :

$$\alpha_- = \max\left(\alpha - 2\delta\left\lceil\frac{\psi}{\delta}\right\rceil; 0\right) \tag{6.24}$$

$$d^-_{pixel} = \left\lfloor\frac{\alpha_-}{\delta}\right\rfloor \tag{6.25}$$

Inversely, if α_+ is the angular span where the footprint intercepts, at least partially, the cylinder and d^+_{pixel} its pixel converted measure, we have :

$$\alpha_+ = \alpha + 2\delta\left\lceil\frac{\psi}{\delta}\right\rceil \tag{6.26}$$

$$d^+_{pixel} = \left\lfloor\frac{\alpha_+}{\delta}\right\rfloor \tag{6.27}$$

where ψ is defined in equation (6.16) and assuming $\gamma = 0$

In the filtered scans cylinder diameters were directly computed in pixel units by counting the number of consecutive valid pixels for a single cylinder slice in the image in the φ direction (along the lines) for all the lines and taking their median. Let p_{est} be that pixel number.

Hole diameters

The same precautions must be taken when evaluating the sky filter on holes. As with the cylinder diameters, hole areas, or solid angles, will be slightly diminished since sky point are defined as points where the laser beam was not intercepted at all. A radius loss of L will then be observed. The corrected hole radius r_- of a circle of radius r at distance R considering the edge loss is :

$$r_- = r - R\tan\left(\delta\left\lceil\frac{\psi}{\delta}\right\rceil\right) \tag{6.28}$$

The corrected radius in pixel units, r_{pixel} is then :

$$r_{pixel} = \frac{r_-}{R\tan(\delta)} \tag{6.29}$$

As the incidence angle on the hole panel ε increases, the circular hole will form an ellipse of increasing eccentricity. For the evaluation of the sky filter, the biggest window size fitting in the original hole w_{max}, and the reconstructed hole w_{est} were computed. This was done to have comparable scale compared to the other evaluations.

The ellipse formed in the image has a semi-major axis a and semi-minor axis b :

$$a = r_{pixel} \tag{6.30}$$
$$b = r_{pixel} \cos(\varepsilon) \tag{6.31}$$

The area of the maximum size square A_{max} inscribed in the ellipse is given by :

$$A_{max} = \frac{4a^2b^2}{a^2 + b^2} \tag{6.32}$$

thus its side w_{max} is :

$$w_{max} = \frac{2r_{pixel}}{R\tan(\delta)} \sqrt{\frac{\cos(\varepsilon)^2}{1 + \cos(\varepsilon)^2}} \tag{6.33}$$

To compute w_{est} from filtered scans, points labelled as noise were projected on the board computed plane following equation (6.4), then triangulated using a Delaunay triangulation. The hole area A_{tri} was estimated by summing the area of each triangle. Finally, the w_{est} was estimated by :

$$w_{est} = \frac{2\sqrt{\frac{A_{tri}}{\pi}}}{R\tan(\delta)} \sqrt{\frac{\cos(\varepsilon)^2}{1 + \cos(\varepsilon)^2}} \tag{6.34}$$

Table 6.6 shows a summary of the values of interest and their estimated counterpart for the two filters.

	Value of interest	Estimated value from scans
Sky filter, holes	w_{max}	w_{est}
Sky filter, cylinders	d^+_{pixel}	p_{est}
Mixed-points filter, cylinders	d^-_{pixel}	p_{est}

Table 6.6 – Values of interest analysed in every filter-setup case

Result analysis

Two approaches were used to assess filter performance. First a regression analysis was performed to extract global trends. For each (δ, Albedo, W, ρ_{sky}) or (δ, Albedo, W, $\beta_{threshold}$) combination, depending on the filter, linear regressions of the values of interest versus estimated values were computed. From the regressions, slope, intercept and Root Mean Square Error (RMSE) were analysed. If $X = (x_1, \ldots, x_n)$ is the set of data of an interest value (here Ω^-_{pixel}, d^+_{pixel} or d^-_{pixel}) of one parameter configuration and $Y = (y_1, \ldots, y_n)$ the set of data of the corresponding estimated value, we have :

$$\overline{x} = \frac{1}{n} \sum_{x \in X} x \tag{6.35}$$

$$slope = \frac{\sum_{i=1}^{n} (y_i - \overline{y})(x_i - \overline{x})}{\sum_{i=1}^{n} (x_i - \overline{x})^2} \tag{6.36}$$

$$intercept = \overline{y} - slope\, \overline{x} \tag{6.37}$$

$$\hat{y}_i = slope\, x_i + intercept \tag{6.38}$$

$$RMSE = \sqrt{\frac{\sum_{i=1}^{n} (y_i - \hat{y}_i)^2}{n}} \tag{6.39}$$

A detailed analysis was then carried with a **Receiver Operating Characteristic** (ROC) analysis. In this analysis data was grouped into pixel size classes shown in table 6.7, and for each (δ, Albedo, W, ρ_{sky}) or (δ, Albedo, W, $\beta_{threshold}$) combination true positive rates tpr and false positive rates fpr of every scan in this category were computed from true positives TP, true negatives TN, false positives FP and false negatives FN numbers of each scans. Mean tpr ($\overline{tpr}$) and fpr ($\overline{fpr}$) were computed for each category.

$$tpr = \frac{TP}{TP + FN} \tag{6.40}$$

$$fpr = \frac{FP}{FP + TN} \tag{6.41}$$

Finally a score was computed from the $\overline{tpr}$ and $\overline{fpr}$ values. In ROC analysis a detector, that for a given parameter has $tpr = 1$ and $fpr = 0$ or $tpr = 0$ and $fpr = 1$ acheives perfectly right (or perfectly wrong)

classification (thus perfect discrimination). Inversely a detector with $tpr = fpr$ can be considered as a random classifier with a probability to classify as noise equal to tpr. The evaluation score used was then the distance to the random classifier (the $tpr = fpr$ line) :

$$score = \left| \sqrt{2} \begin{pmatrix} \cos\left(-\frac{\pi}{4}\right) & -\sin\left(-\frac{\pi}{4}\right) \\ \sin\left(-\frac{\pi}{4}\right) & \cos\left(-\frac{\pi}{4}\right) \end{pmatrix} \begin{pmatrix} \overline{fpr} \\ \overline{tpr} \end{pmatrix} \cdot \begin{pmatrix} 0 \\ 1 \end{pmatrix} \right| \tag{6.42}$$

$$score = \left| \begin{pmatrix} 1 & 1 \\ -1 & 1 \end{pmatrix} \begin{pmatrix} \overline{fpr} \\ \overline{tpr} \end{pmatrix} \cdot \begin{pmatrix} 0 \\ 1 \end{pmatrix} \right| \tag{6.43}$$

$$score = \left| \overline{tpr} - \overline{fpr} \right| \tag{6.44}$$

Pixel size classes			
0	$[1,3]$	$[4,6]$	≥ 7

Table 6.7 – Pixel size classes

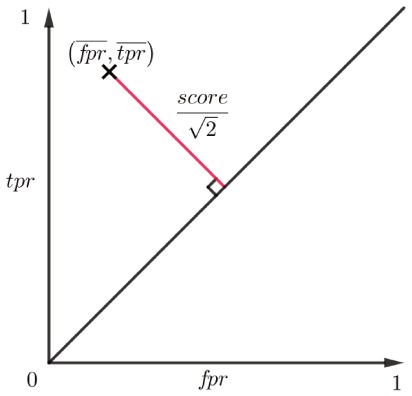

Figure 6.3 – Score used in the ROC evaluation.

6.4 Sky filter results

In this section we will present the results of the regression and the ROC analysis for the sky filter on cylinder targets and hole targets. We only present in this document the results for the brown paper and for the Ultra and High resolutions for the ROC analysis. The results for all colors and resolutions are available at https://github.com/rrombourg/Chapter6_Results.

Sky filter on holes

Figures 6.4 through 6.7 show the regression results for the brown part of the board (21% albedo) for all four resolutions. $slope$, $intercept$ and $RMSE$ point to a consistent result degradation as the resolution goes from Ultra to Low. Resolution also increased the effect of the window, high W values ($W > 9$) on Medium or Low resolutions resulted in poor diameter estimation and worse filter consistency for all pixel sizes (increased $RMSE$). Regression results showed little effect of albedo on filter quality.

Figures 6.8 to 6.12 present ROC analysis results for the brown part of the board in Ultra and High resolution, other resolutions showed similar behaviours. The number of data points used to compute each value is presented figure 6.14. The window parameter had little effect whatever the object sizes present in the Ultra and High scans but filtering performance was highly degraded on small objects ($p_{size} \in [1, 3]$) filtered with high window parameters ($W > 5$) this effect can only be seen in Medium and Low scans since the lowest pixel sizes were not present otherwise. For all resolutions and pixel sizes, tpr as well as fpr increased with increasing ρ_{sky}, with best detection performance for $\rho_{sky} \in [90, 99]$ for all object sizes.

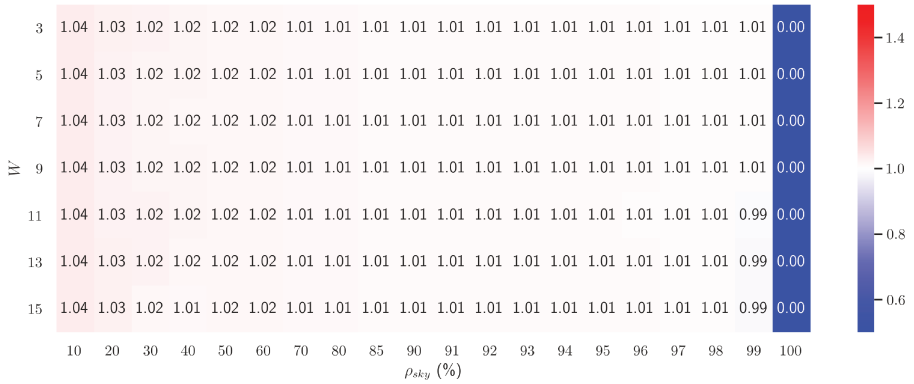

(a) U, Brown, *slope*

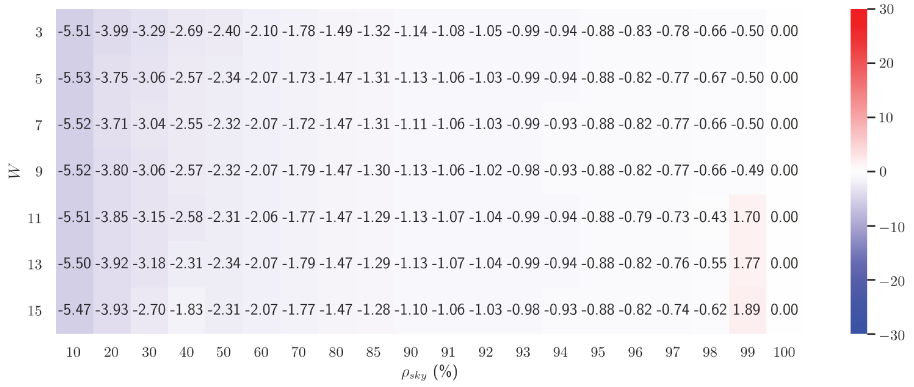

(b) U, Brown, *intercept*

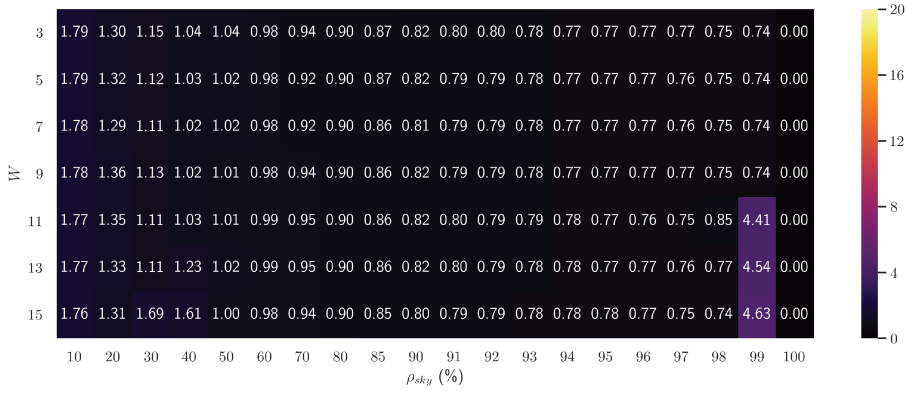

(c) U, Brown, *RMSE*

Figure 6.4 – Sky filter regression results for the brown hole slice in Ultra resolution.

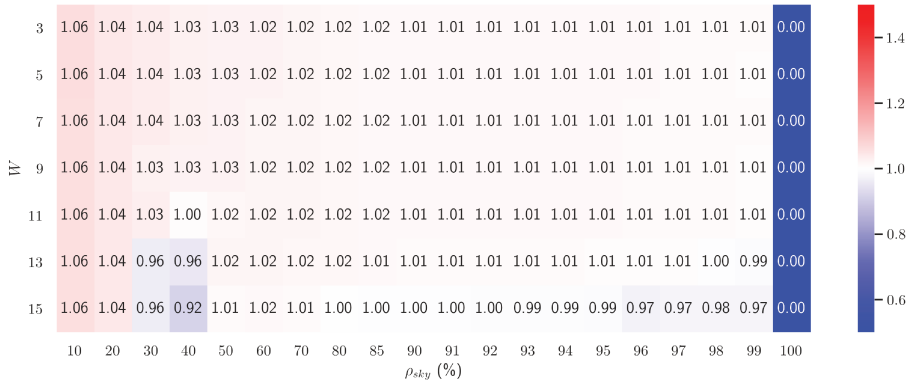

(a) H, Brown, *slope*

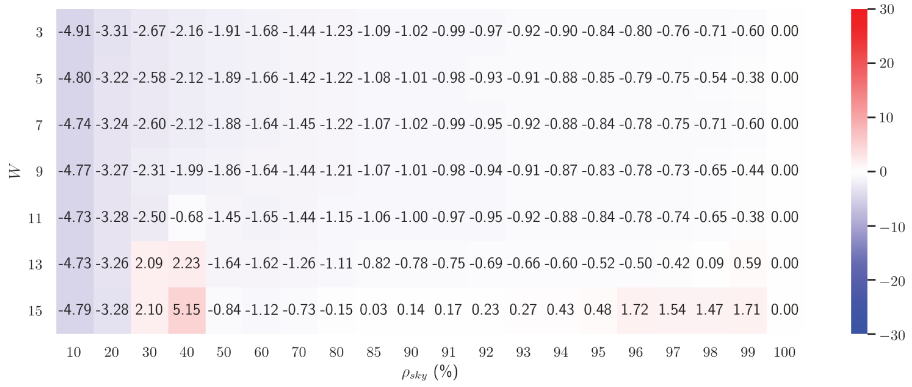

(b) H, Brown, *intercept*

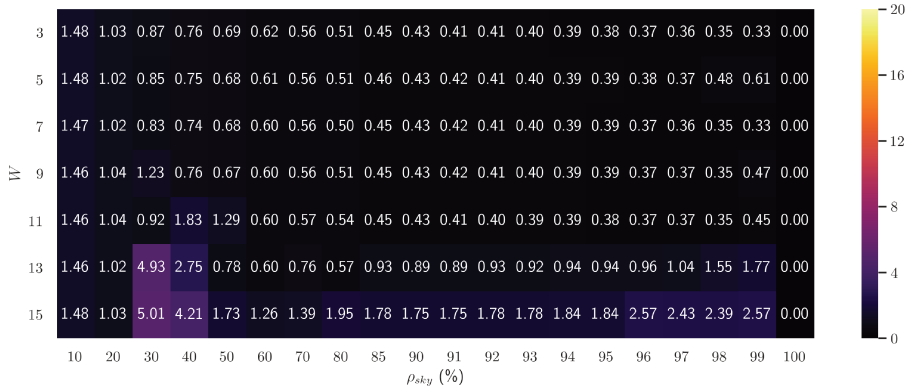

(c) H, Brown, *RMSE*

Figure 6.5 – Sky filter regression results for the brown hole slice in High resolution.

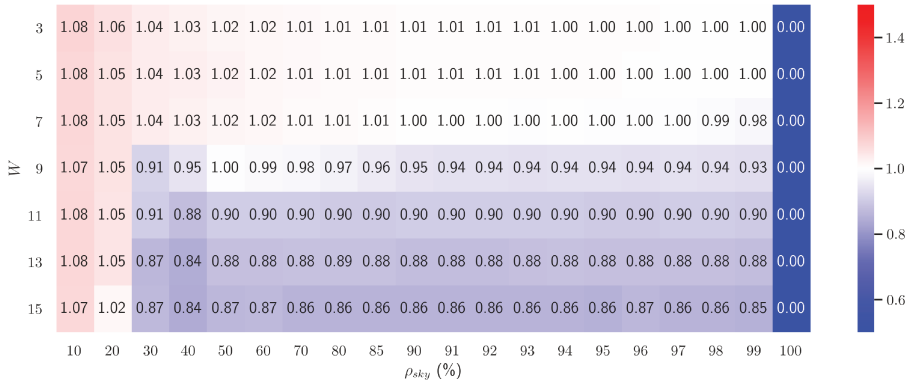

(a) M, Brown, *slope*

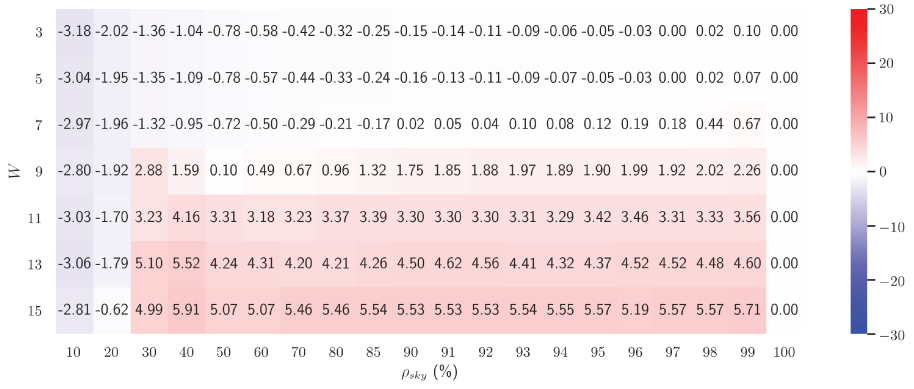

(b) M, Brown, *intercept*

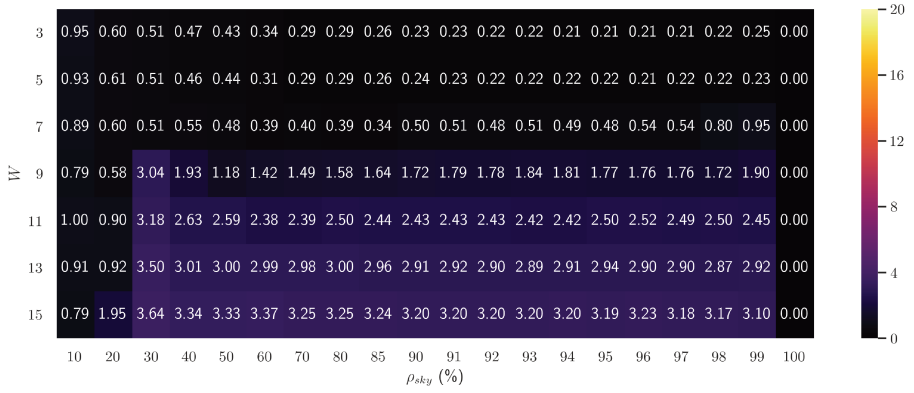

(c) M, Brown, *RMSE*

Figure 6.6 – Sky filter regression results for the brown hole slice in Medium resolution.

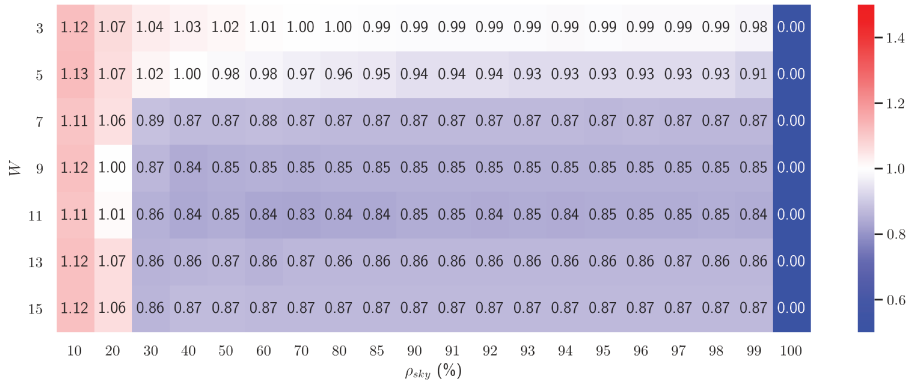

(a) L, Brown, *slope*

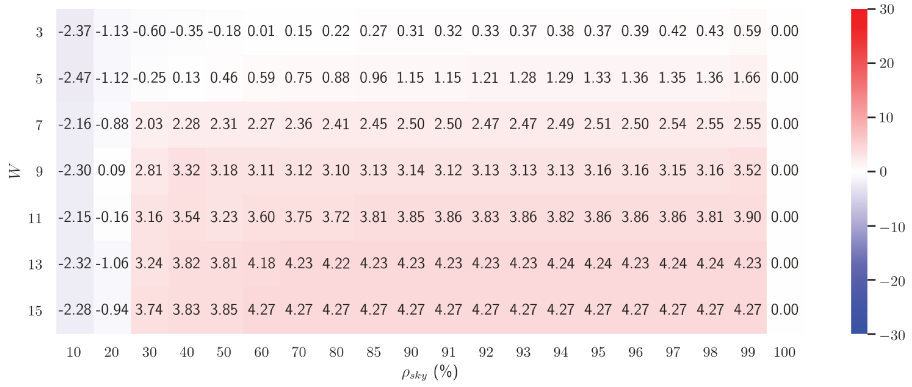

(b) L, Brown, *intercept*

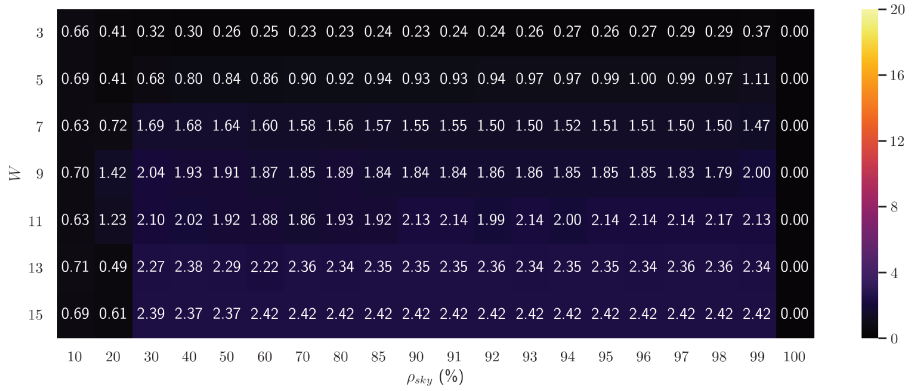

(c) L, Brown, *RMSE*

Figure 6.7 – Sky filter regression results for the brown hole slice in Low resolution.

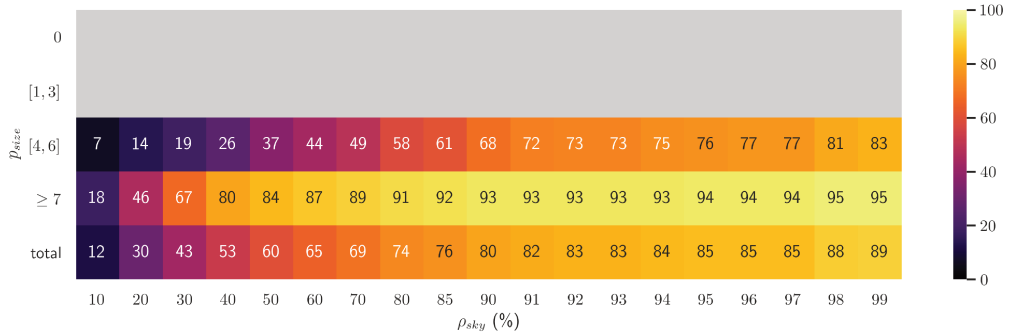

(a) U, Brown, W_3, $score$

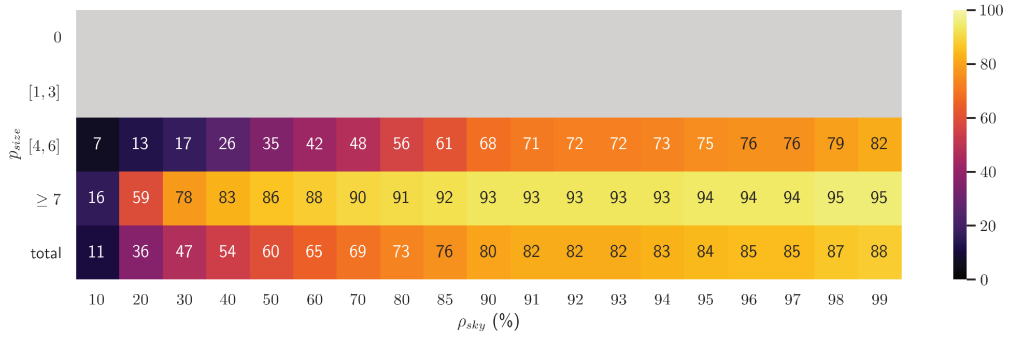

(b) U, Brown, W_5, $score$

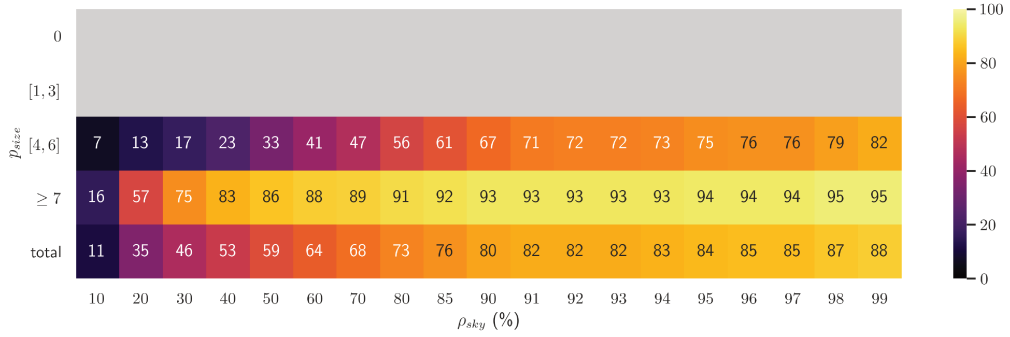

(c) U, Brown, W_7, $score$

Figure 6.8 – Sky filter ROC $score$ results for the brown hole slice in Ultra resolution for W_3, W_5, W_7.

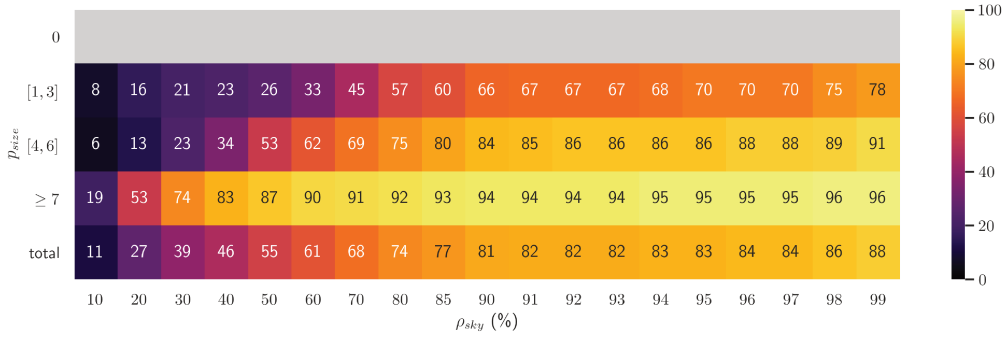

(a) H, Brown, W_3, $score$

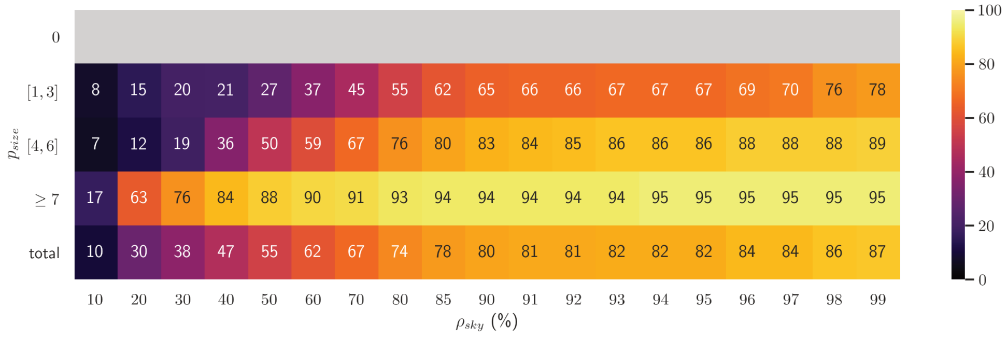

(b) H, Brown, W_5, $score$

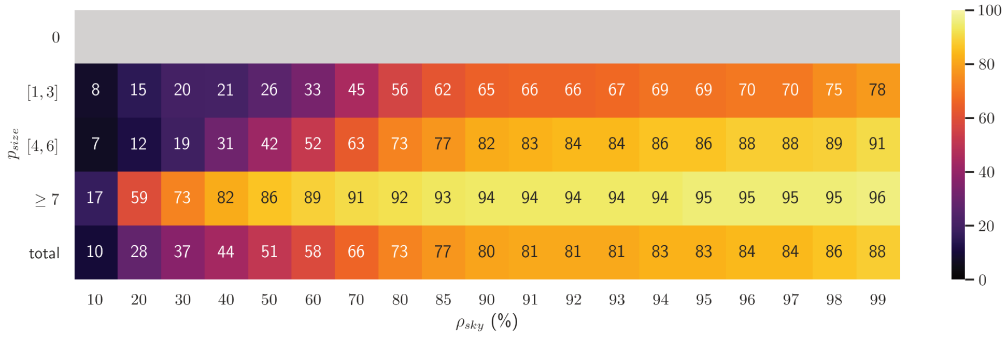

(c) H, Brown, W_7, $score$

Figure 6.9 – Sky filter ROC $score$ results for the brown hole slice in High resolution for W_3, W_5, W_7.

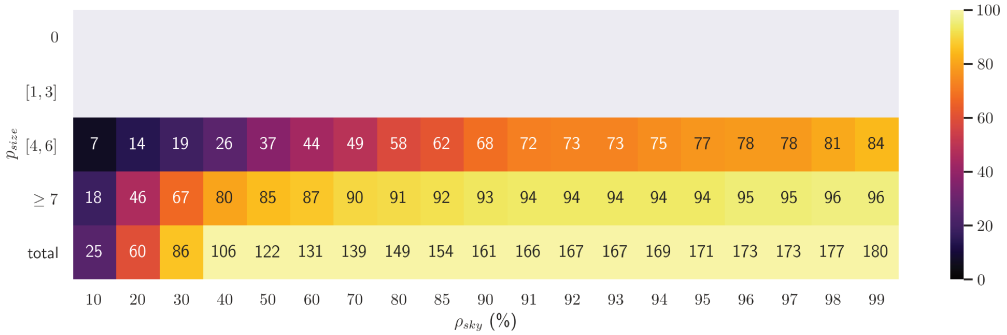

(a) U, Brown, W_3, tpr

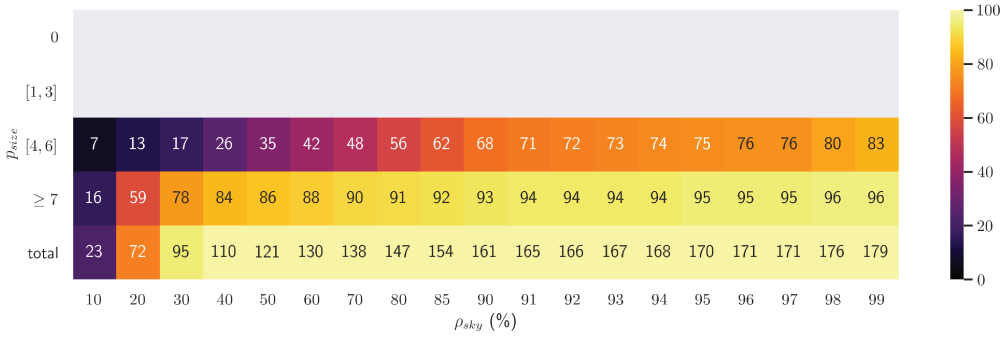

(b) U, Brown, W_5, tpr

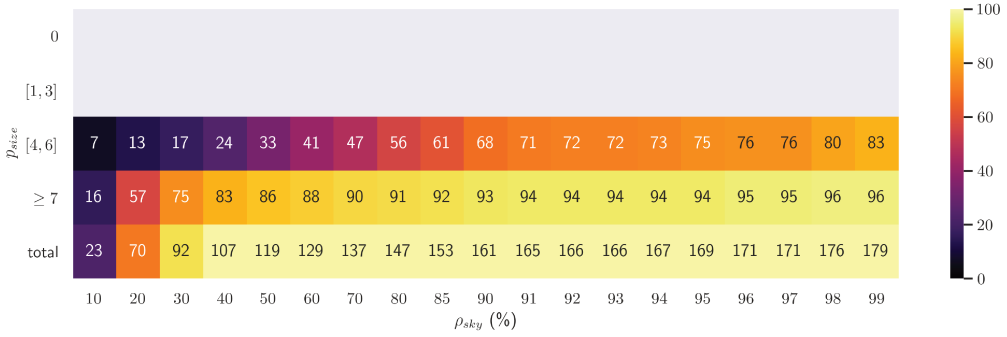

(c) U, Brown, W_7, tpr

Figure 6.10 – Sky filter ROC tpr results for the brown hole slice in Ultra resolution for W_3, W_5, W_7.

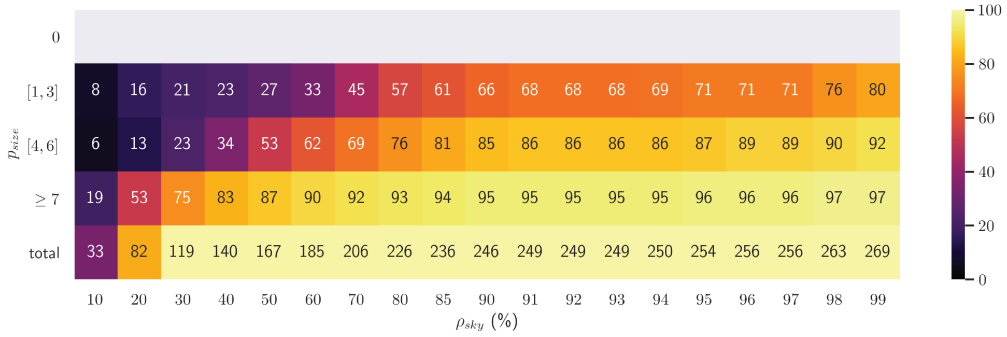

(a) H, Brown, W_3, tpr

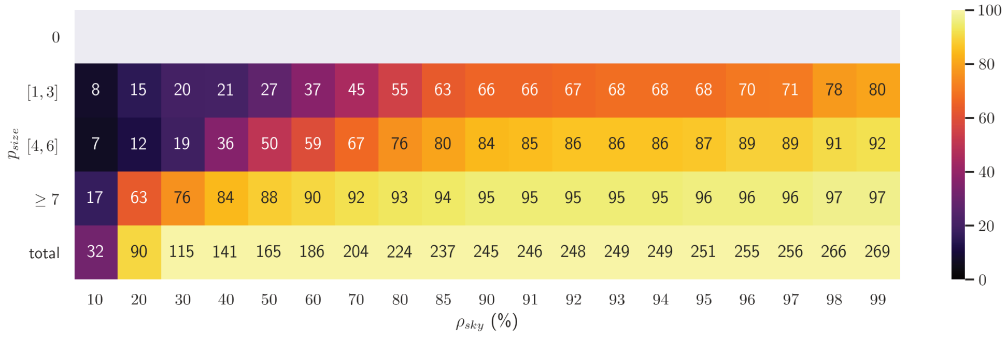

(b) H, Brown, W_5, tpr

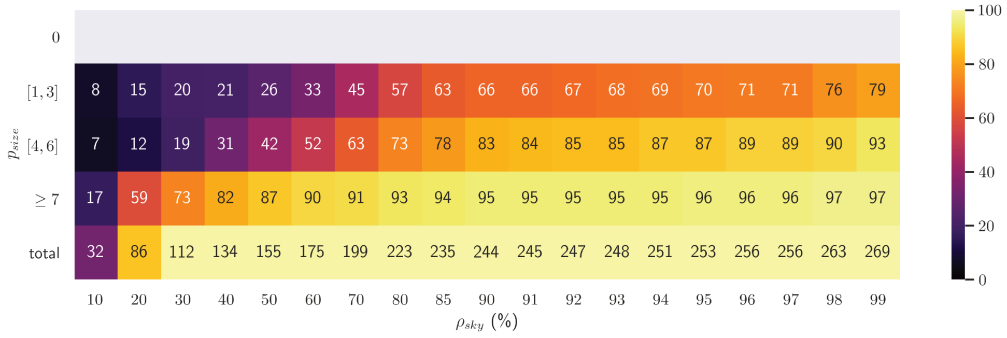

(c) H, Brown, W_7, tpr

Figure 6.11 – Sky filter ROC tpr results for the brown hole slice in High resolution for W_3, W_5, W_7.

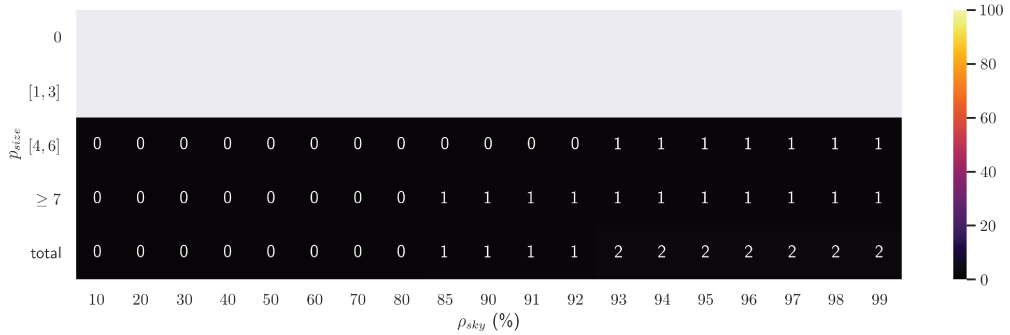

(a) U, Brown, W_3, *fpr*

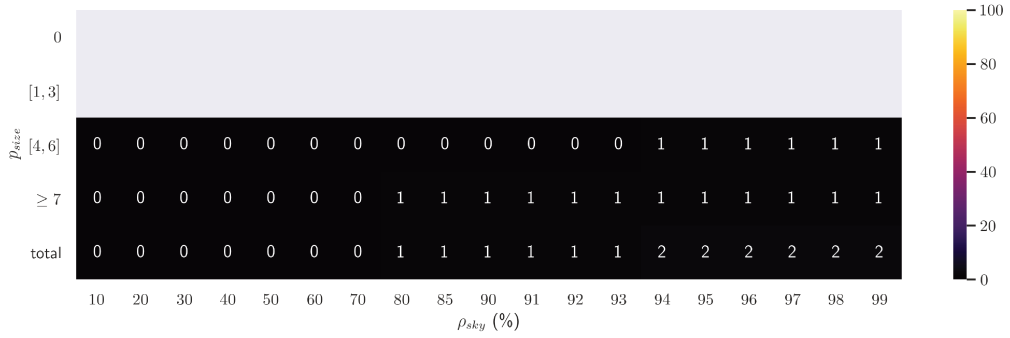

(b) U, Brown, W_5, *fpr*

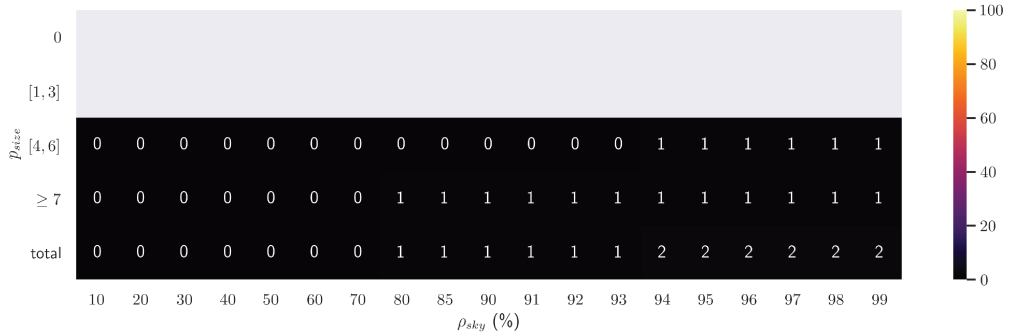

(c) U, Brown, W_7, *fpr*

Figure 6.12 – Sky filter ROC *fpr* results for the brown hole slice in Ultra resolution for W_3, W_5, W_7.

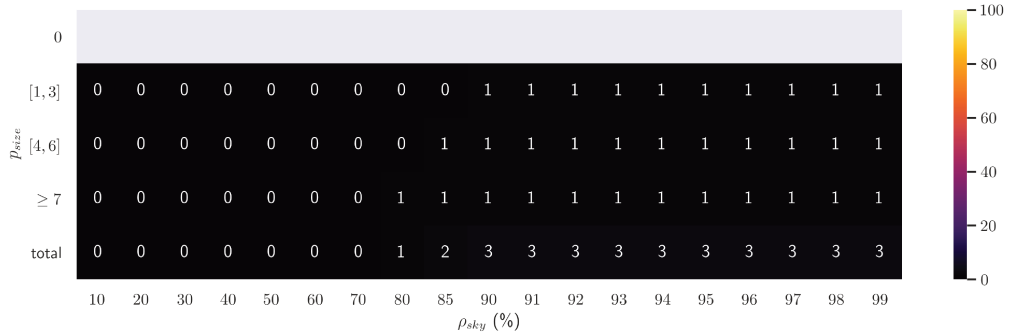

(a) H, Brown, W_3, *fpr*

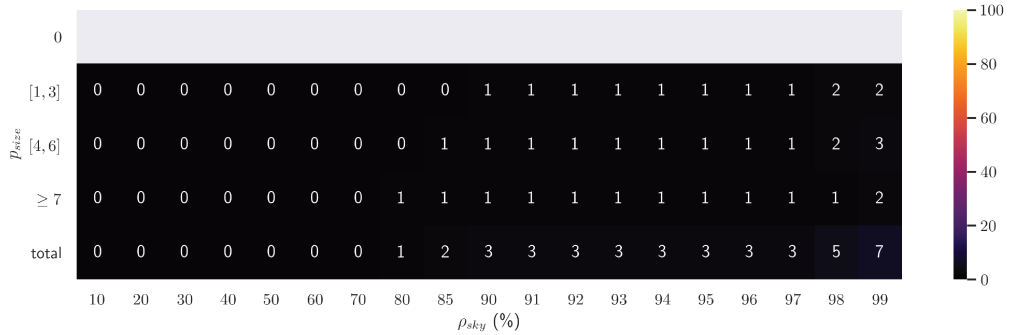

(b) H, Brown, W_5, *fpr*

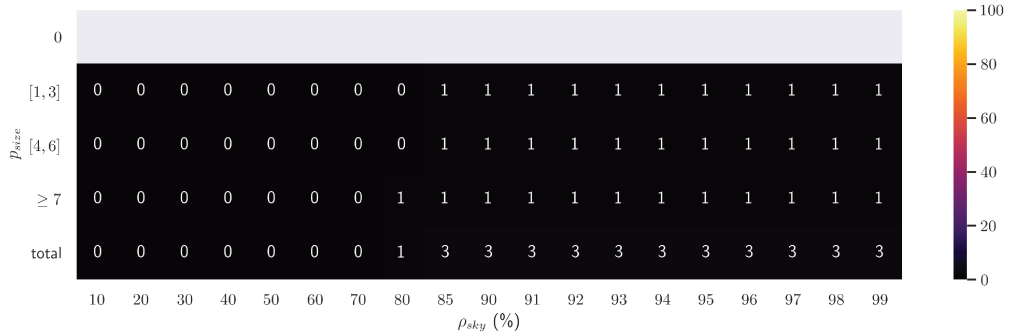

(c) H, Brown, W_7, *fpr*

Figure 6.13 – Sky filter ROC *fpr* results for the brown hole slice in High resolution for W_3, W_5, W_7.

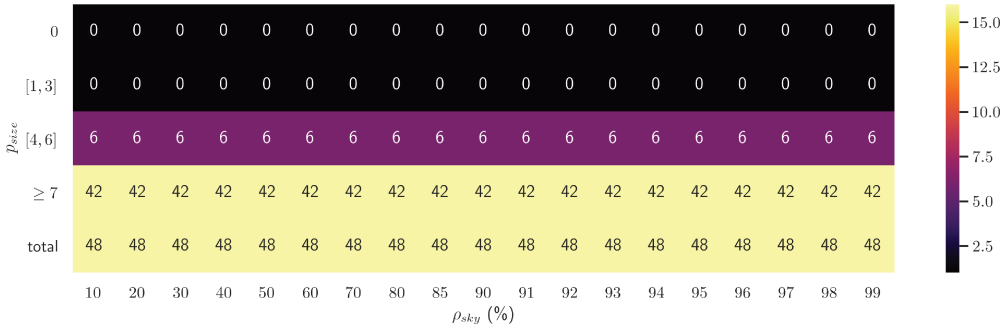

(a) U, N_{data}

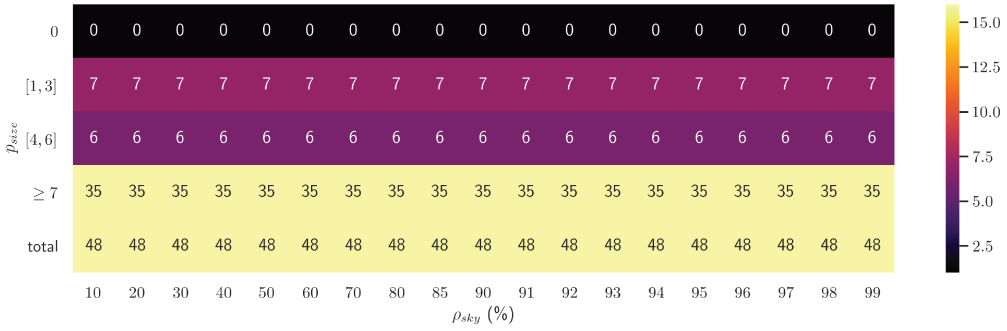

(b) H, N_{data}

Figure 6.14 – Number of data per class for the sky filter ROC analysis in Ultra and High resolution for W_3, W_5, W_7.

Sky filter on cylinders

Figures 6.15 through 6.18 show the regression results for the brown slice (21% albedo) for all four resolutions. $slope$, $intercept$ and $RMSE$ point to a consistent result degradation as the resolution goes from Ultra to Low. According to the regression results window had little impact in Ultra and High resolution for high enough ρ_{sky} (≥ 90). Concerning Medium and Low resolution, window above 9 lead to reduced filter consistency, i.e. increased $RMSE$, high $slope$ and low $intercept$ indicating over-filtering of small elements and under-filtering of larger ones. Note that parameters configurations with 0 $slope$, $intercept$ and $RMSE$ indicate a configuration where all estimated diameters were equal to 0 (indicating strong over-filtering). Regression results showed little of albedo on filter quality.

Figures 6.19 to 6.21 present ROC analysis results for the brown slice in Ultra and High resolution, other resolutions showed similar behaviours. The number of data points used to compute each value is presented figure 6.22. The window parameter had no effect whatever the object sizes present in the Ultra and High scans but filtering performance was highly degraded on small objects ($p_{size} \in [1, 3]$) filtered with high window parameters ($W > 5$) this effect can only be seen in Medium and Low scans since the lowest pixel sizes were not present otherwise. For all resolutions and pixel sizes, tpr as well as fpr increased with increasing ρ_{sky}, with good compromise ($score > 80$) for $\rho_{sky} \in [90, 99]$.

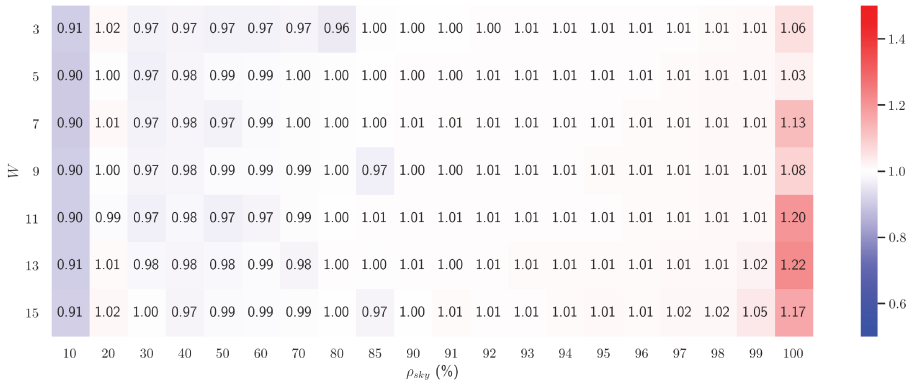

(a) U, Brown, *slope*

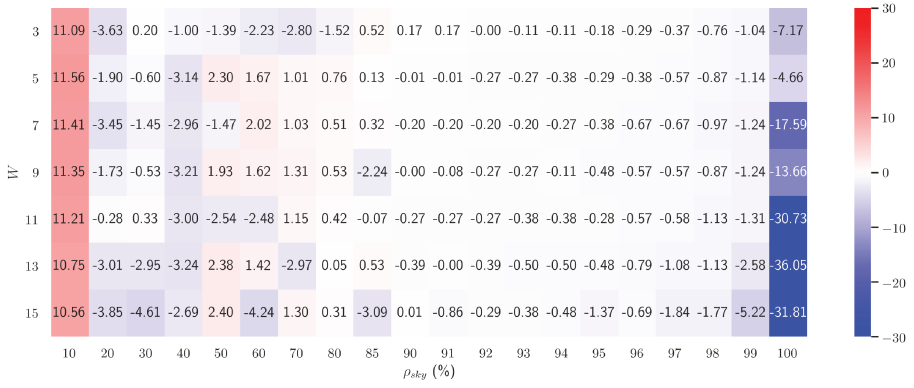

(b) U, Brown, *intercept*

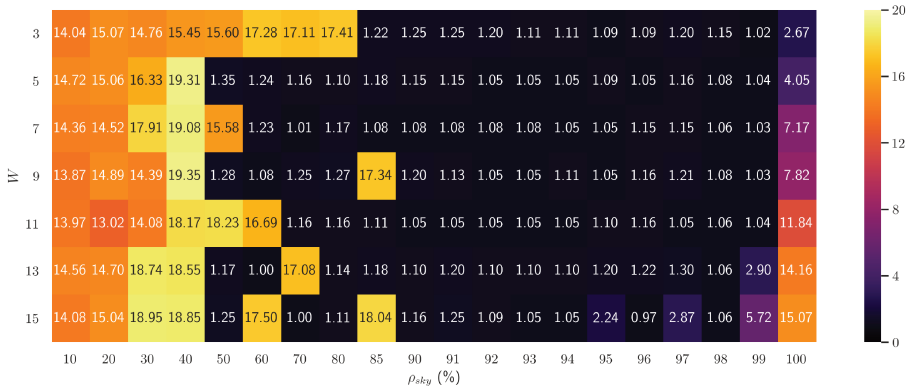

(c) U, Brown, *RMSE*

Figure 6.15 – Sky filter regression results for the brown cylinder slice in Ultra resolution.

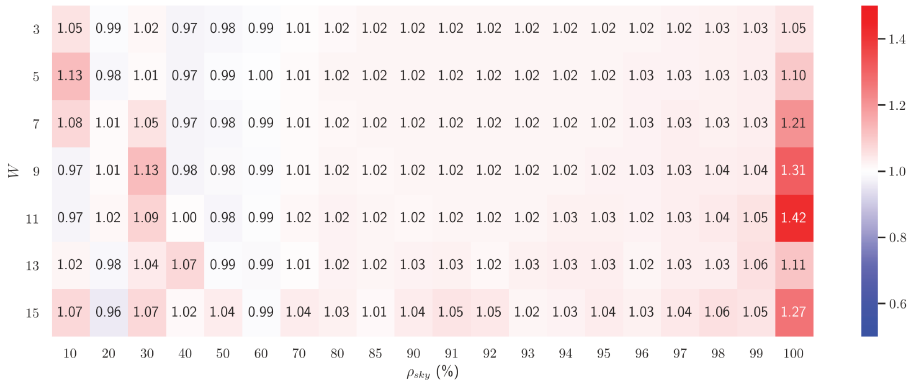

(a) H, Brown, *slope*

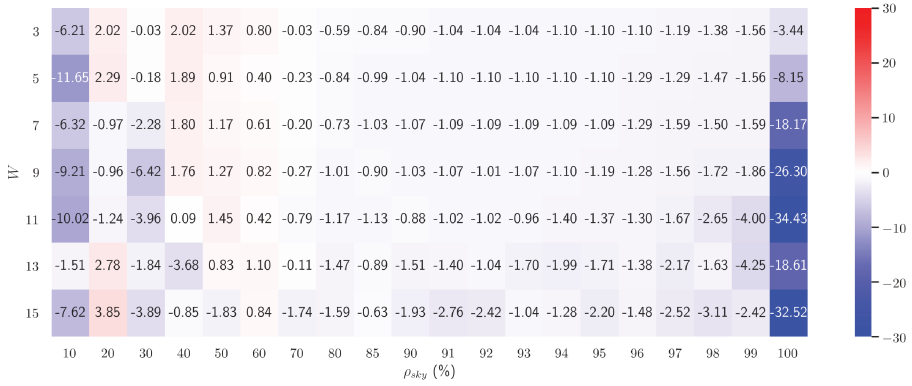

(b) H, Brown, *intercept*

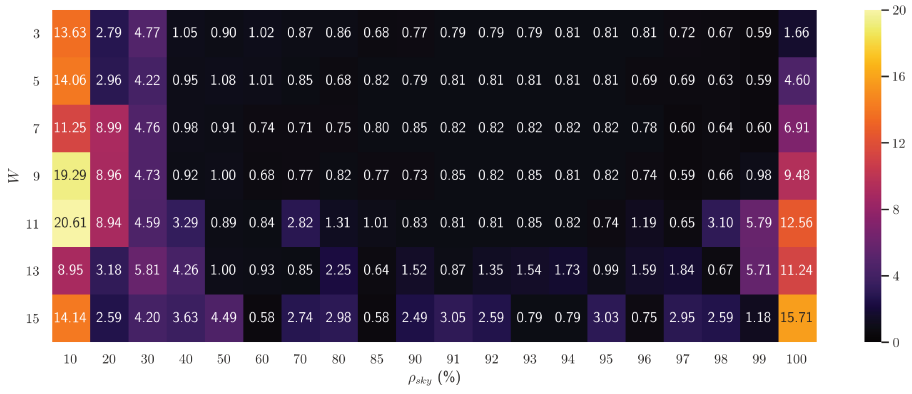

(c) H, Brown, *RMSE*

Figure 6.16 – Sky filter regression results for the brown cylinder slice in High resolution.

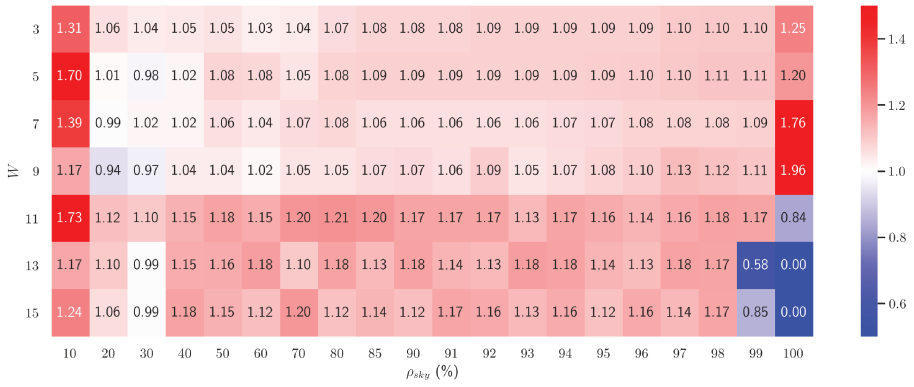

(a) M, Brown, *slope*

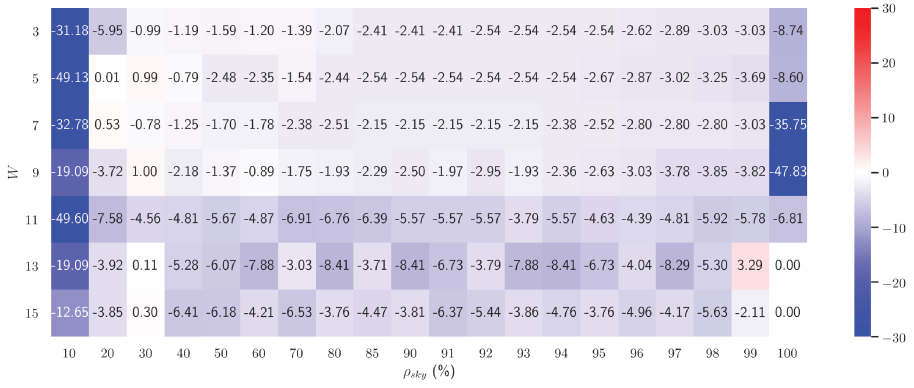

(b) M, Brown, *intercept*

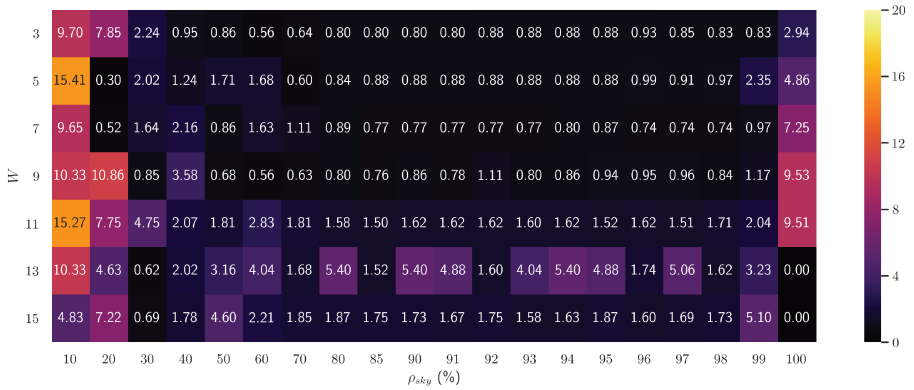

(c) M, Brown, *RMSE*

Figure 6.17 – Sky filter regression results for the brown cylinder slice in Medium resolution.

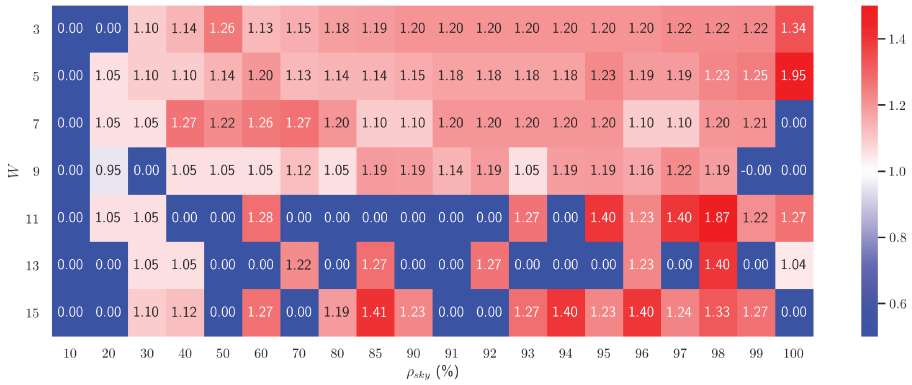

(a) L, Brown, *slope*

(b) L, Brown, *intercept*

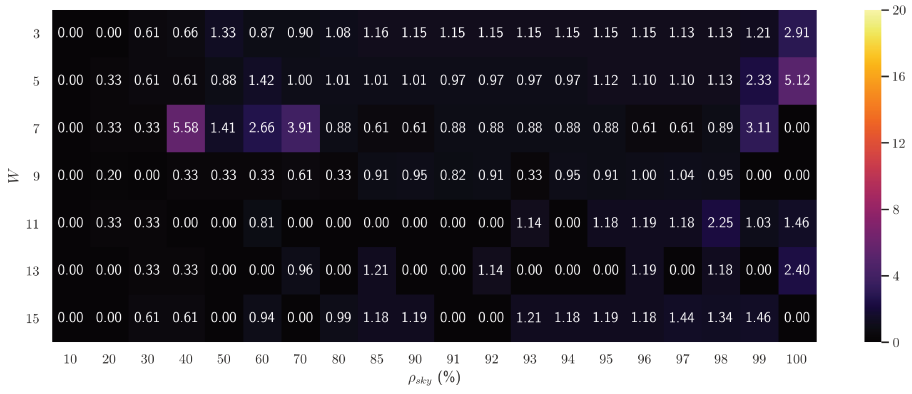

(c) L, Brown, *RMSE*

Figure 6.18 – Sky filter regression results for the brown cylinder slice in Low resolution.

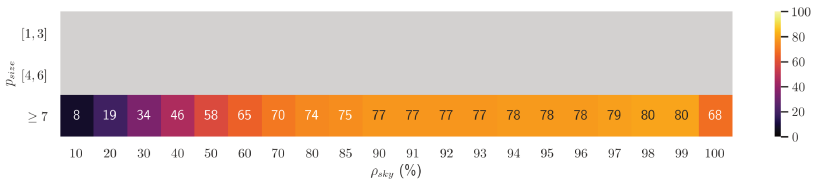

(a) U, Brown, W_3, $score$

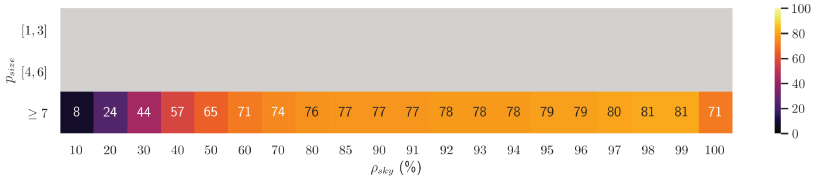

(b) U, Brown, W_5, $score$

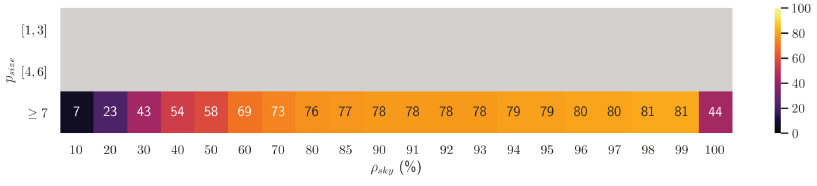

(c) U, Brown, W_7, $score$

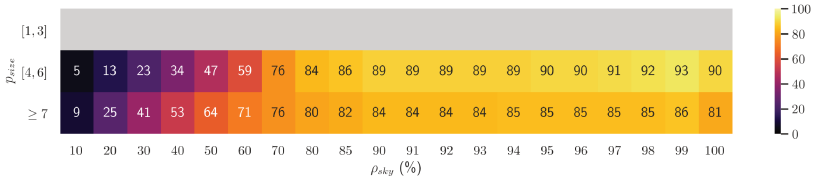

(d) H, Brown, W_3, $score$

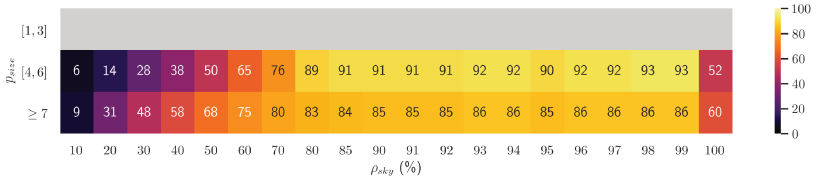

(e) H, Brown, W_5, $score$

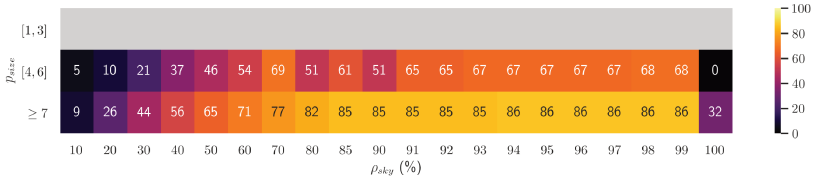

(f) H, Brown, W_7, $score$

Figure 6.19 – Sky filter ROC $score$ results for the brown cylinder slice in Ultra and High resolutions for W_3, W_5, W_7.

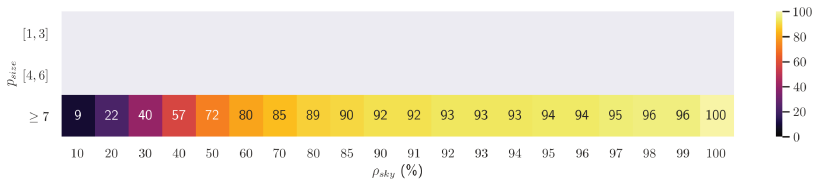

(a) U, Brown, W_3, tpr

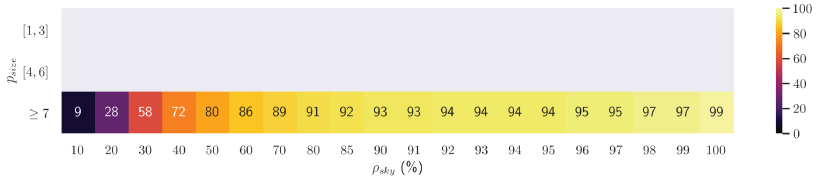

(b) U, Brown, W_5, tpr

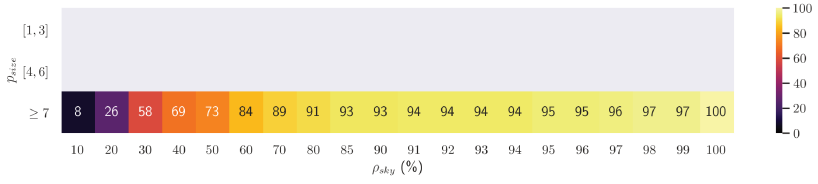

(c) U, Brown, W_7, tpr

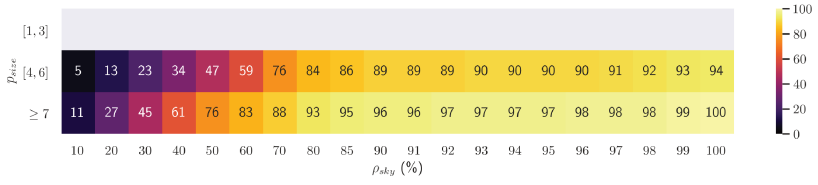

(d) H, Brown, W_3, tpr

(e) H, Brown, W_5, tpr

(f) H, Brown, W_7, tpr

Figure 6.20 – Sky filter ROC tpr results for the brown cylinder slice in Ultra and High resolution for W_3, W_5, W_7.

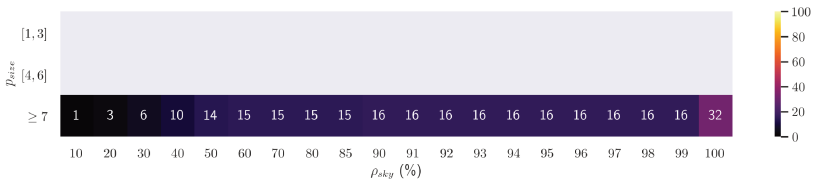

(a) U, Brown, W_3, *fpr*

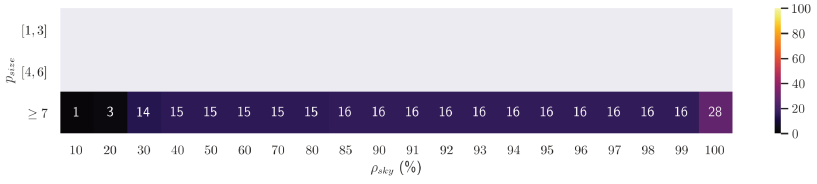

(b) U, Brown, W_5, *fpr*

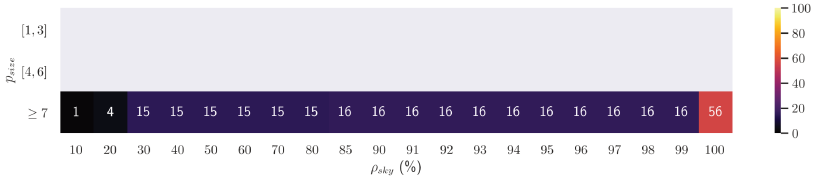

(c) U, Brown, W_7, *fpr*

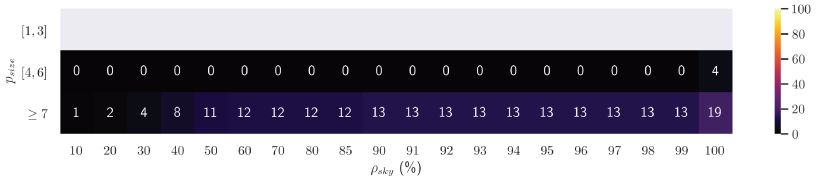

(d) H, Brown, W_3, *fpr*

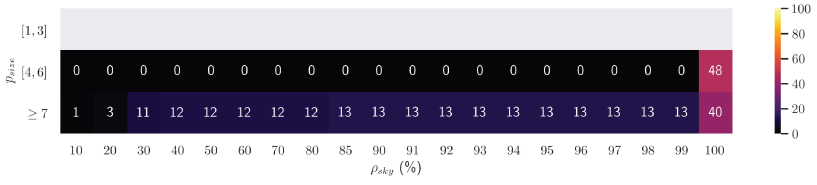

(e) H, Brown, W_5, *fpr*

(f) H, Brown, W_7, *fpr*

Figure 6.21 – Sky filter ROC *fpr* results for the brown cylinder slice in Ultra and High resolution for W_3, W_5, W_7.

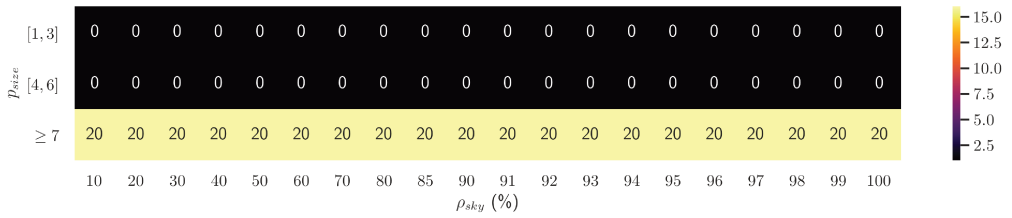

(a) U, N_{data}

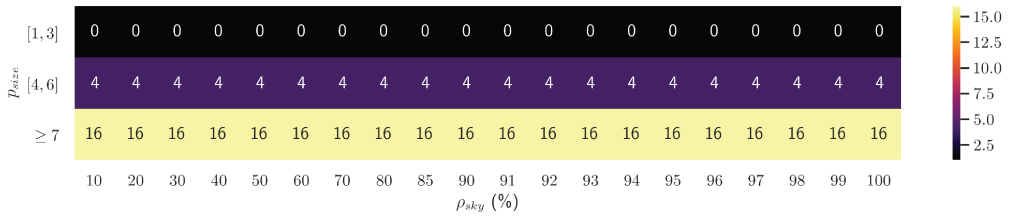

(b) H, N_{data}

Figure 6.22 – Number of data per class for the sky filter ROC analysis in Ultra and High resolution for W_3, W_5, W_7.

6.5 Mixed-point filter results

In this section we will present the results of the regression and the ROC analysis for the mixed-point filter on cylinder targets. As stated in the previous section, we only present in this document the results for the brown paper and for the Ultra and High resolutions for the ROC analysis. The results for all colors and resolutions are available at https://github.com/rrombourg/Chapter6_Results.

Figures 6.23 through 6.26 show the regression results for the brown cylinder slice for all four resolutions. $slope$, $intercept$ and $RMSE$ point to a consistent result degradation as the resolution goes from Ultra to Low, especially for Medium and Low resolutions. Window had little impact in Ultra and High resolution for high enough $\beta_{threshold}$ (≥ 75). For Medium and Low resolution, window above 9 lead to reduced filter consistency and increase in over-filtering for low $\beta_{threshold}$. For mixed-point the filter regression results showed little effect of albedo on filter quality.

Figures 6.27 to 6.31 present ROC analysis results for the brown slice in Ultra and High resolution, other resolutions showed similar behaviours. The number of data points used to compute each value is presented figure 6.33. The window parameter had little effect on $[4-6]$ and ≥ 7 pixel size categories objects in the Ultra and High scans. For all resolutions and pixel sizes, tpr as well as fpr decreased with increasing $\beta_{threshold}$, with best compromise for $\beta_{threshold} \in [75, 83]$. The filter consistently showed fpr around 40% and tpr around 90% for the best compromises.

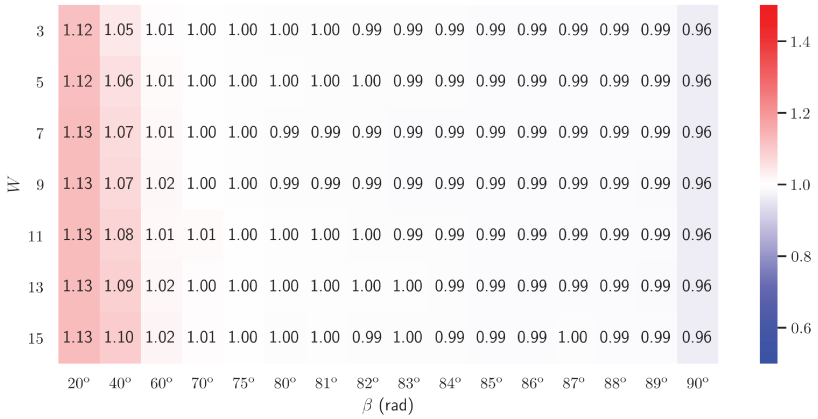

(a) U, Brown, *slope*

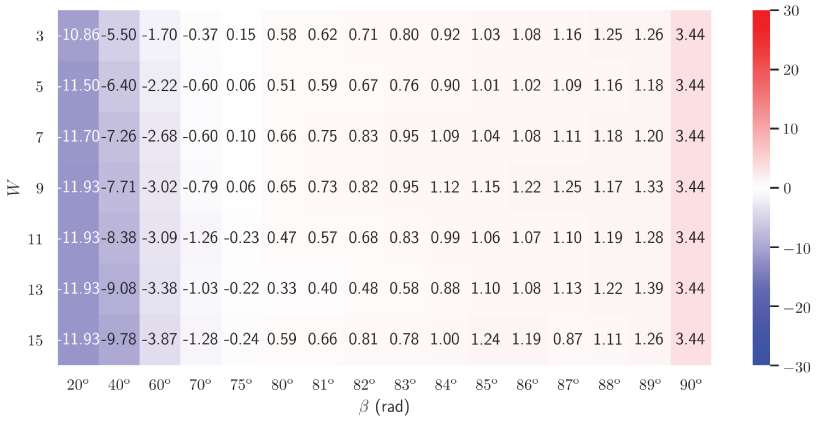

(b) U, Brown, *intercept*

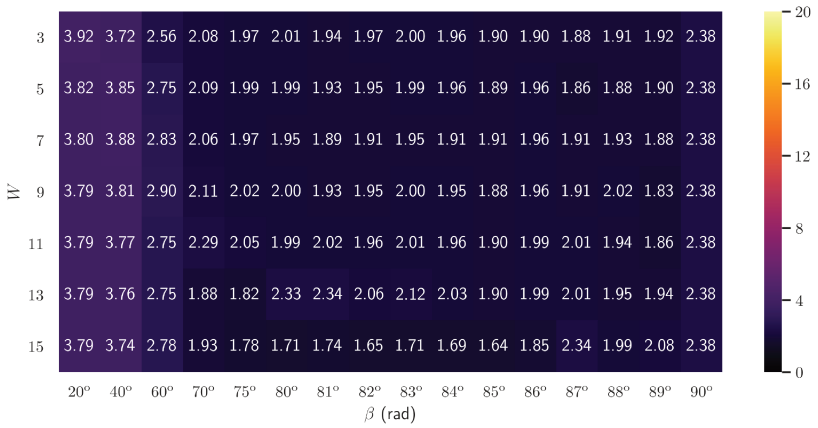

(c) U, Brown, *RMSE*

Figure 6.23 – Mixed-point filter regression results for the brown cylinder slice in Ultra resolution.

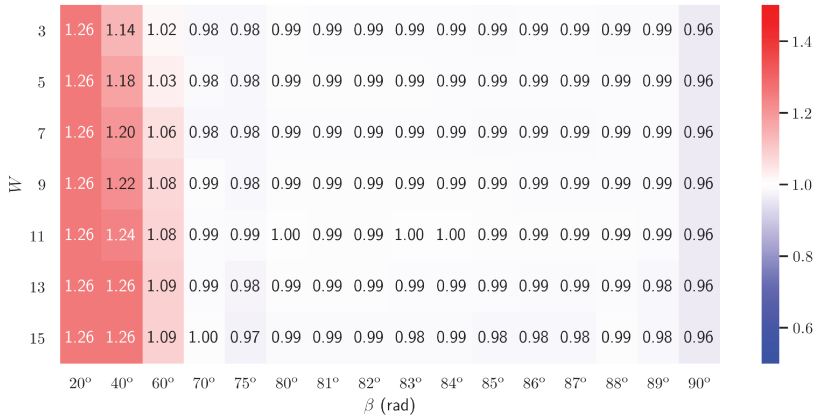

(a) H, Brown, *slope*

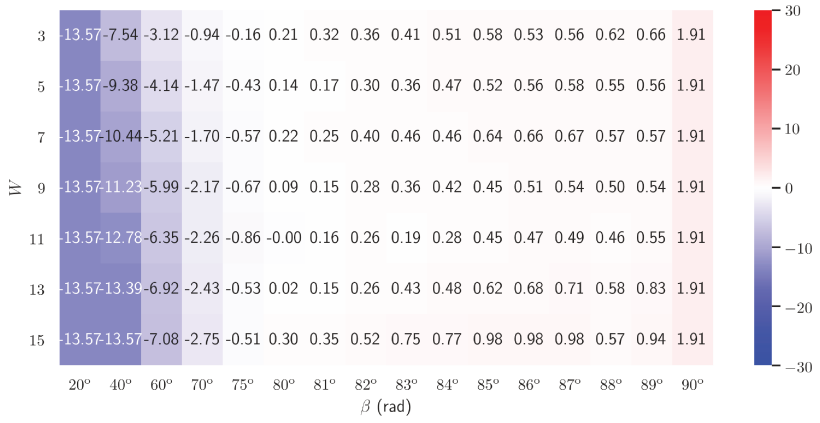

(b) H, Brown, *intercept*

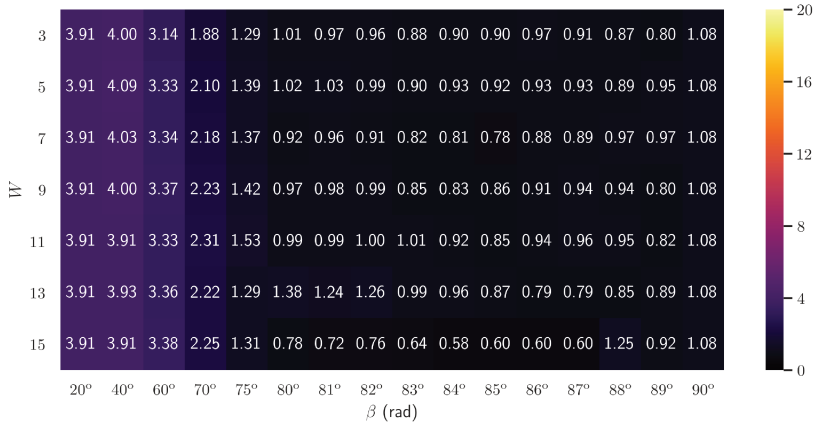

(c) H, Brown, *RMSE*

Figure 6.24 – Mixed-point filter regression results for the brown cylinder slice in High resolution.

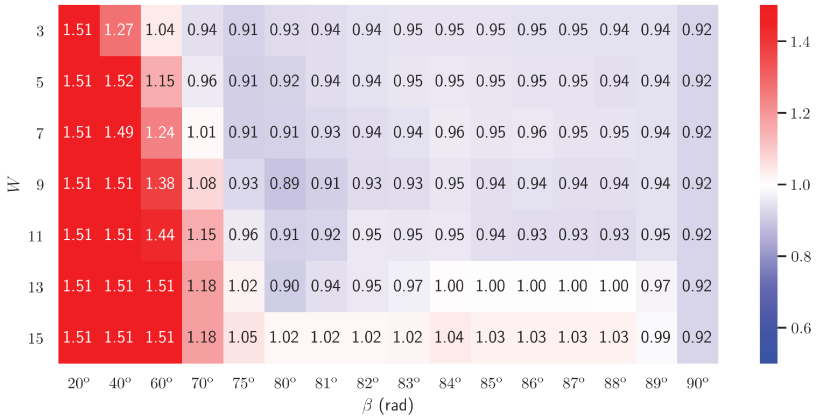

(a) M, Brown, *slope*

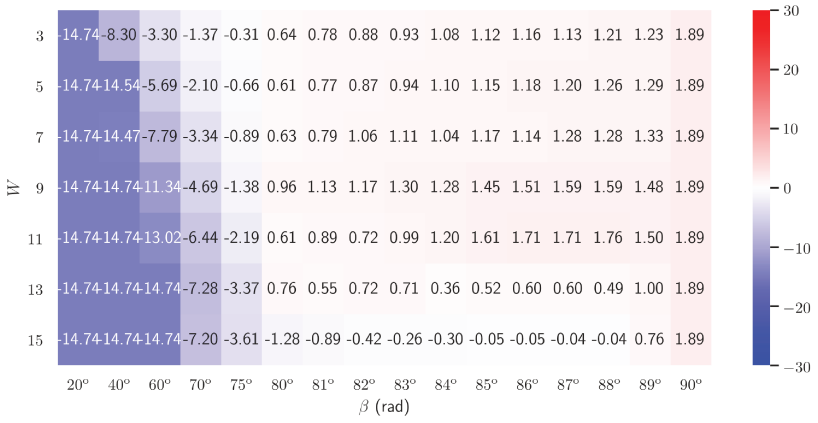

(b) M, Brown, *intercept*

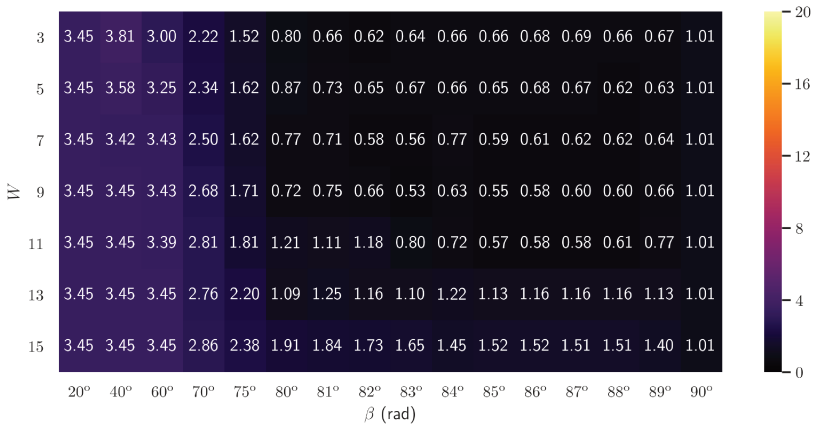

(c) M, Brown, *RMSE*

Figure 6.25 – Mixed-point filter regression results for the brown cylinder slice in Medium resolution.

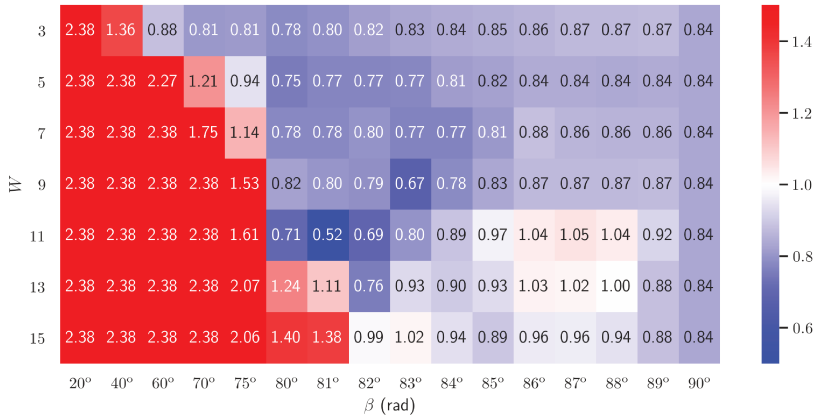

(a) L, Brown, *slope*

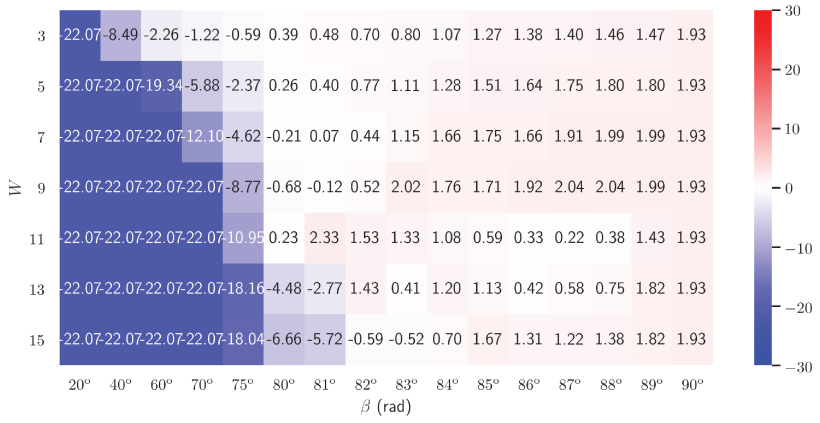

(b) L, Brown, *intercept*

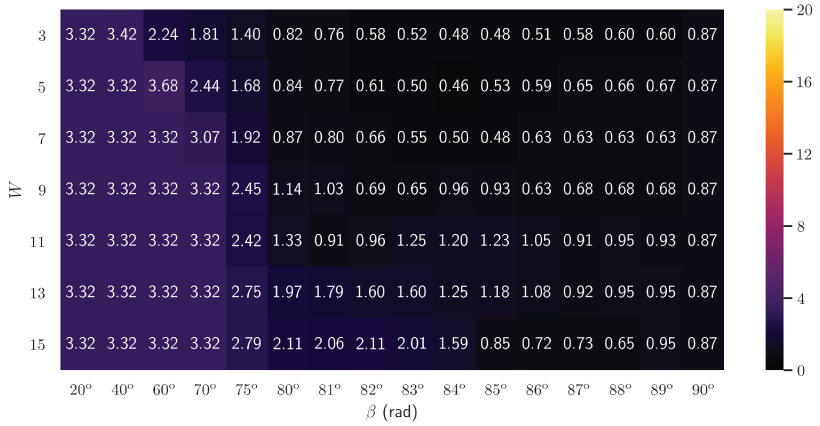

(c) L, Brown, *RMSE*

Figure 6.26 – Mixed-point filter regression results for the brown cylinder slice in Low resolution.

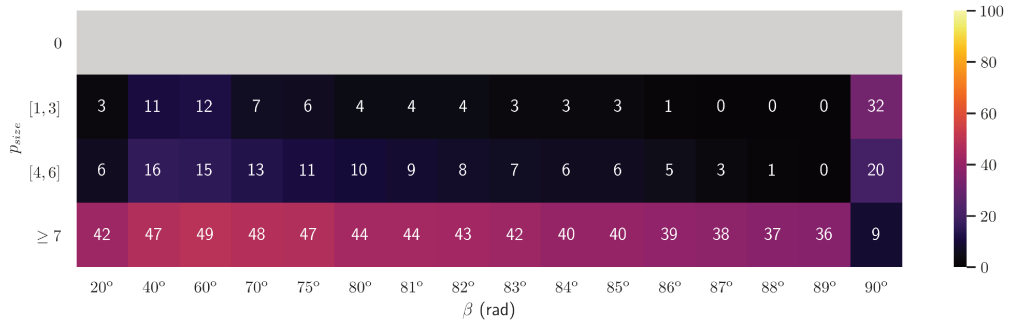

(a) U, Brown, W_3, $score$

(b) U, Brown, W_5, $score$

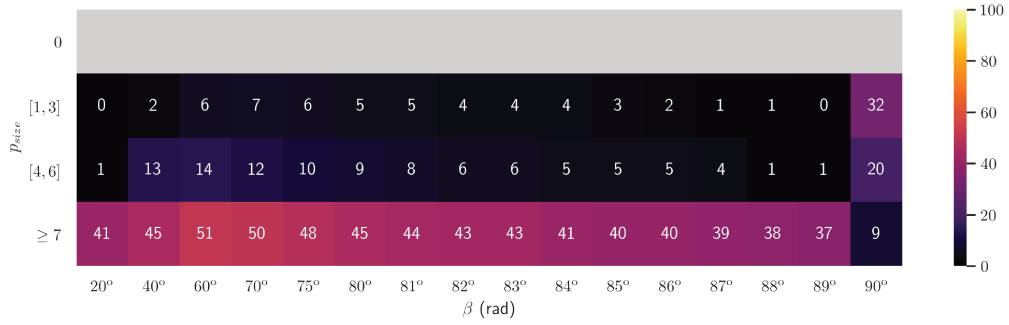

(c) U, Brown, W_7, $score$

Figure 6.27 – Mixed-point filter ROC $score$ results for the brown cylinder slice in Ultra resolution for W_3, W_5, W_7.

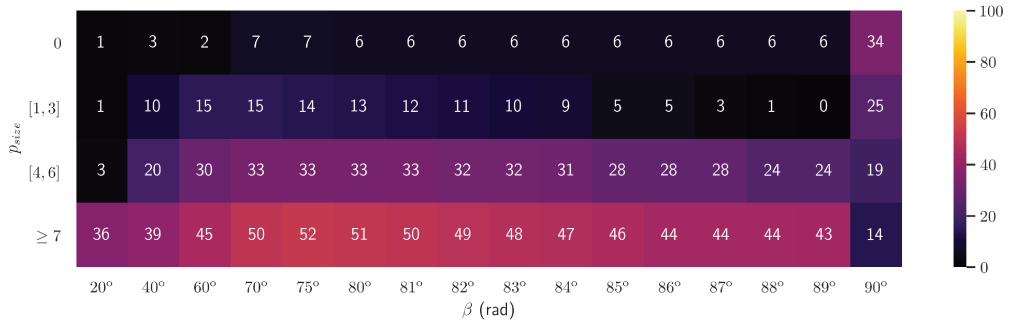

(a) H, Brown, W_3, $score$

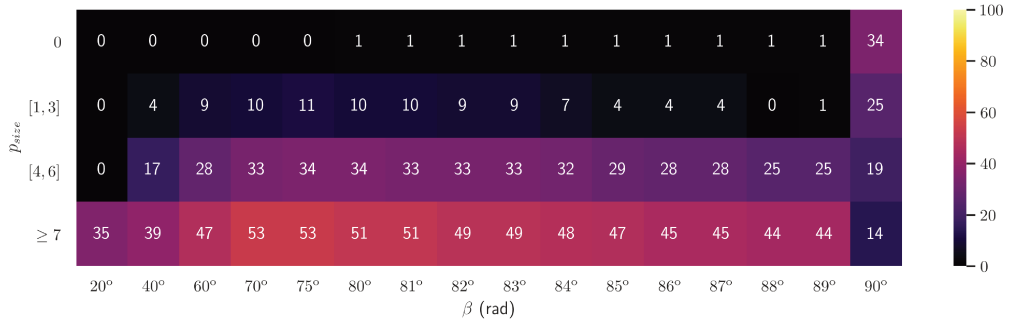

(b) H, Brown, W_5, $score$

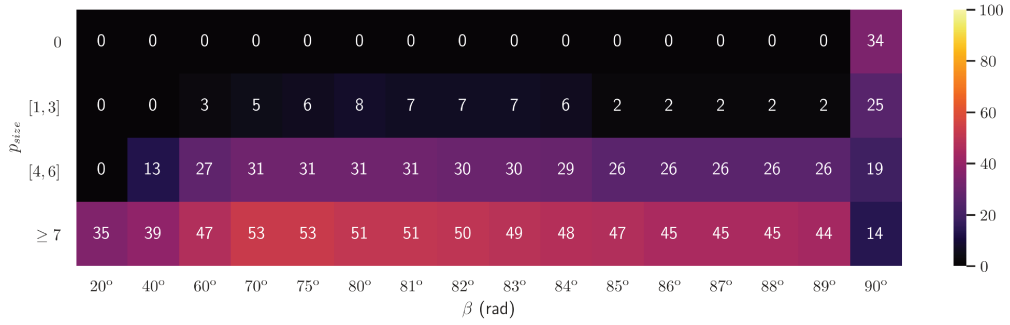

(c) H, Brown, W_7, $score$

Figure 6.28 – Mixed-point filter ROC $score$ results for the brown cylinder slice in High resolutions for W_3, W_5, W_7.

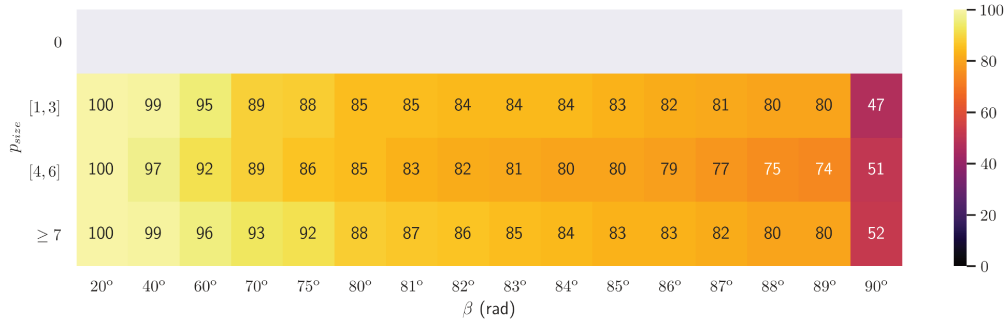

(a) U, Brown, W_3, tpr

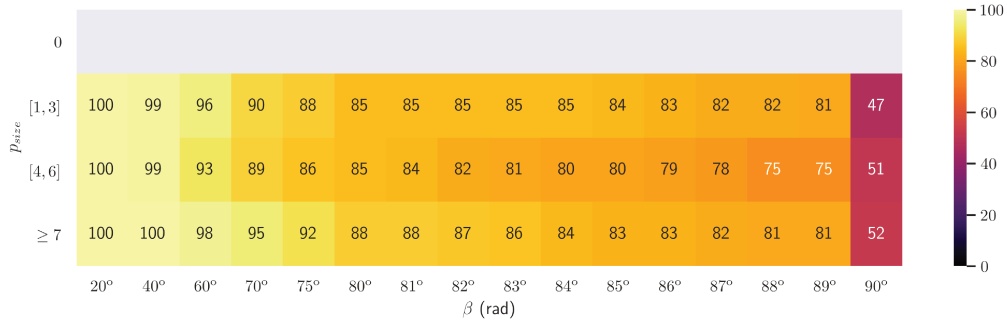

(b) U, Brown, W_5, tpr

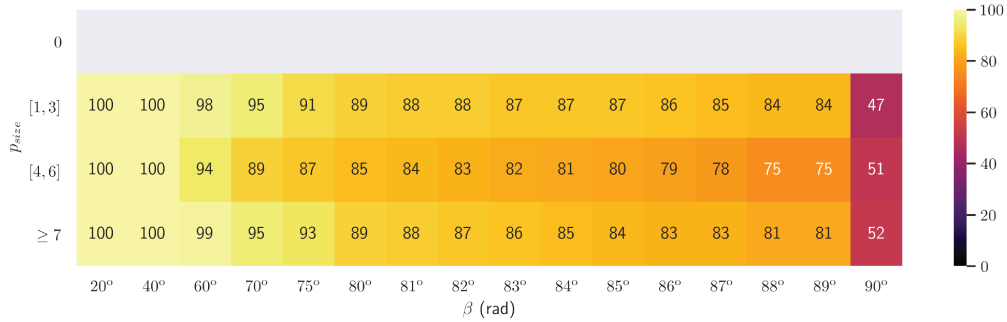

(c) U, Brown, W_7, tpr

Figure 6.29 – Mixed-point filter ROC tpr results for the brown cylinder slice in Ultra resolution for W_3, W_5, W_7.

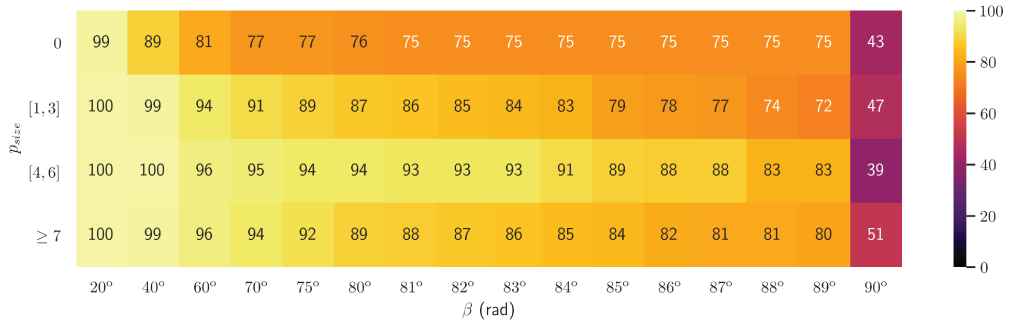

(a) H, Brown, W_3, tpr

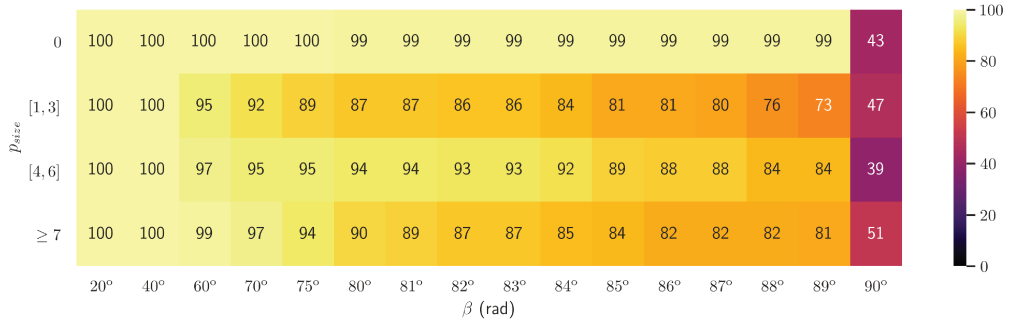

(b) H, Brown, W_5, tpr

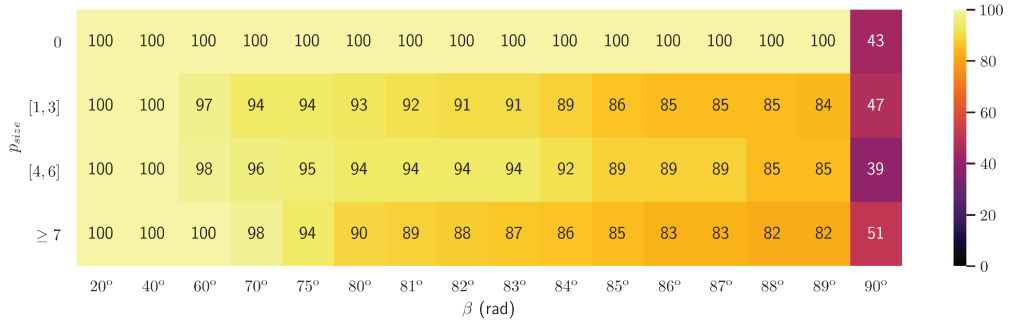

(c) H, Brown, W_7, tpr

Figure 6.30 – Mixed-point filter ROC tpr results for the brown cylinder slice in High resolution for W_3, W_5, W_7.

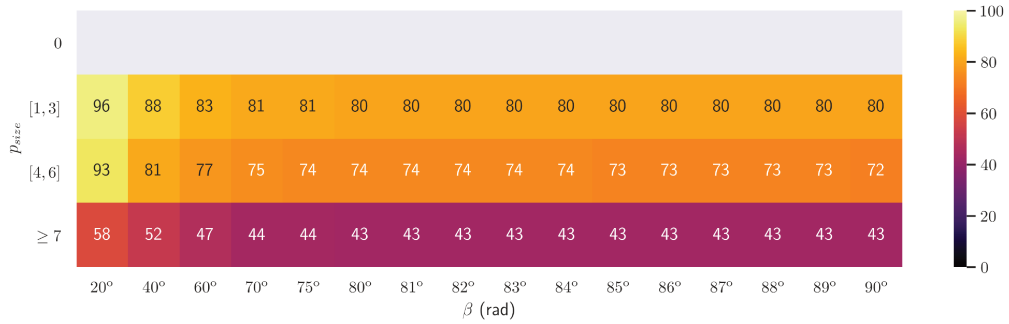

(a) U, Brown, W_3, *fpr*

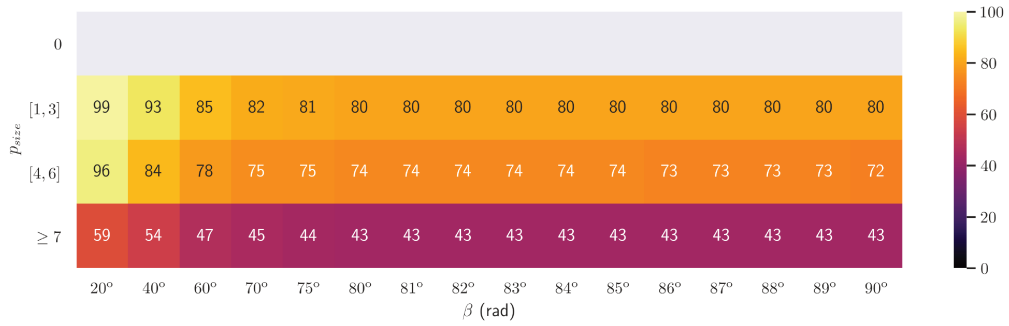

(b) U, Brown, W_5, *fpr*

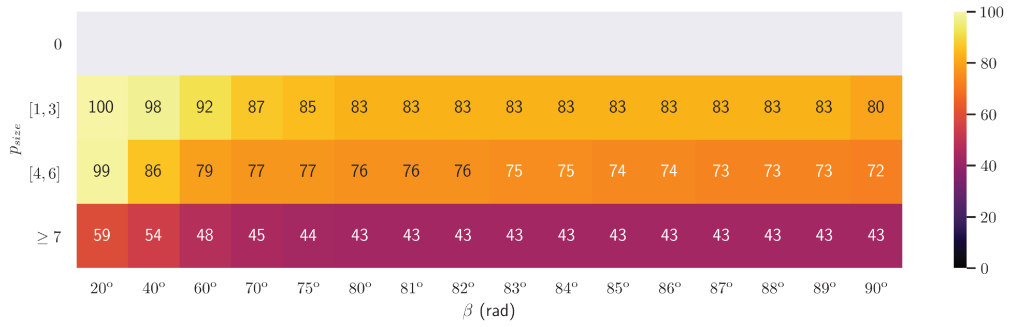

(c) U, Brown, W_7, *fpr*

Figure 6.31 – Mixed-point filter ROC *fpr* results for the brown cylinder slice in Ultra resolution for W_3, W_5, W_7.

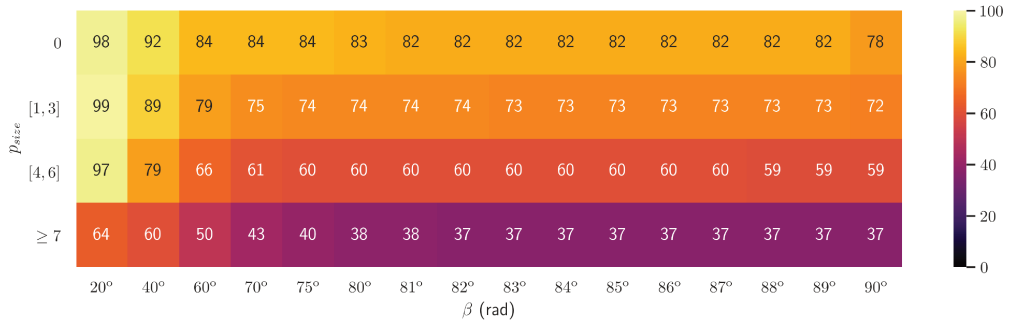

(a) H, Brown, W_3, *fpr*

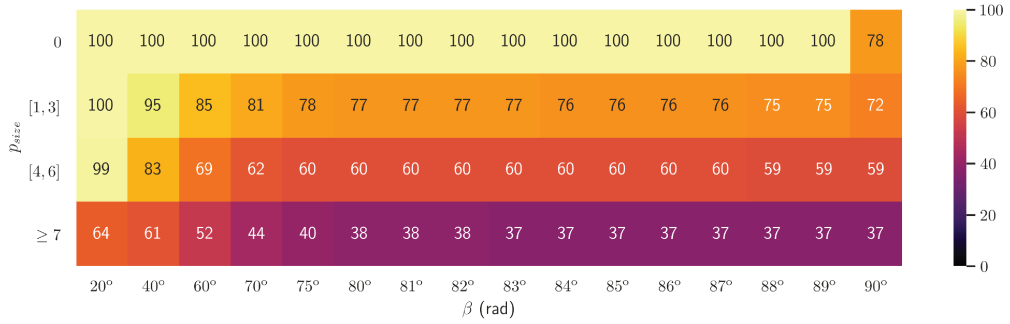

(b) H, Brown, W_5, *fpr*

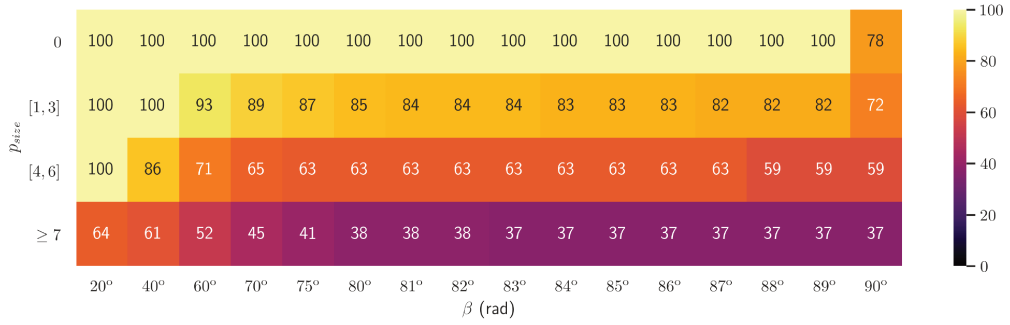

(c) H, Brown, W_7, *fpr*

Figure 6.32 – Mixed-point filter ROC *fpr* results for the brown cylinder slice High resolution for W_3, W_5, W_7.

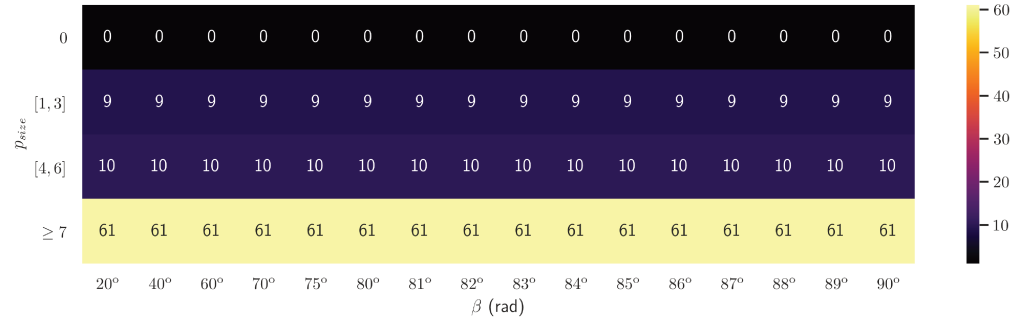

(a) U, N_{data}

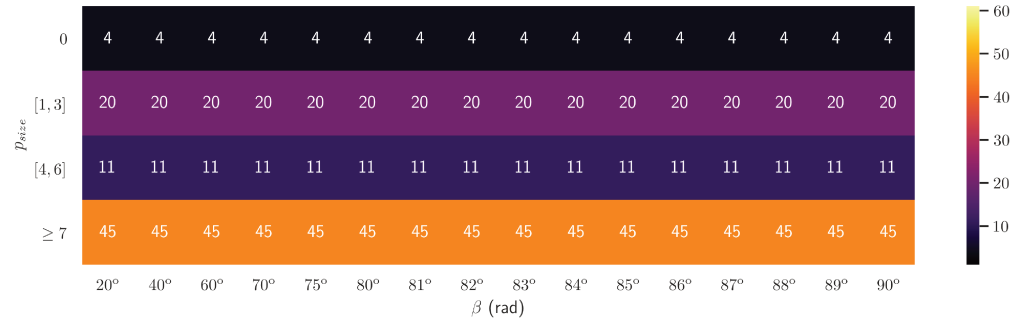

(b) H, N_{data}

Figure 6.33 – Number of data per class for the mixed-point filter ROC analysis in Ultra and High resolution for W_3, W_5, W_7.

6.6 Discussion

In the following section will be presented the discussion of the results found in the filter experimentation.

Sky filter discussion

Results showed that the proposed sky noise detector could consistently detect almost all noise with few false positives and for all tested object colors :

- In Ultra resolution the best compromised was achieved for $\rho_{sky} = 99$ and $W = 5$ with $tpr = 97\%$ and $fpr = 16\%$
- In High resolution the best compromised was achieved for $\rho_{sky} = 99$ and $W = 3$ with $tpr = 96\%$ and $fpr = 7\%$
- In Medium resolution the best compromised was achieved for $\rho_{sky} = 99$ and $W = 3$ with $tpr = 91\%$ and $fpr = 5\%$
- In Low resolution the best compromised was achieved for $\rho_{sky} = 93$ and $W = 3$ with $tpr = 97\%$ and $fpr = 17\%$

As stated previously the filter had good detection performances for all resolution for $W = 3$ and $\rho_{sky} \in [90, 99]$. Cylinder results showed poorer performance than the holes results. This could be caused by the reference point classification. Indeed, reference construction for the cylinder targets was much more prone to errors, especially for small cylinders due to the quasi nonexistence of visual cues and points that could be declared non-noisy with just visual inspection. Drop in performances could have also been caused by the drop in intensity at the border of the cylinder (itself due to the rapid increase in incidence angle), making sky intensities and cylinder intensities closer. Also the small performance difference between colored targets seems to indicates that even for albedos as low as 9% (at $670nm$ for our green target) the intensity differences are sufficient for the filter to work properly.

Mixed-point filter discussion

The best found compromises were :

- In Ultra resolution the best compromised was achieved for $\beta_{threshold} = 60$ and $W = 3$ with $tpr = 94\%$ and $fpr = 69\%$
- In High resolution the best compromised was achieved for $\beta_{threshold} = 75$ and $W = 3$ with $tpr = 88\%$ and $fpr = 64\%$

- In Medium resolution the best compromised was achieved for $\beta_{threshold} = 83$ and $W = 3$ with $tpr = 91\%$ and $fpr = 53\%$
- In Low resolution the best compromised was achieved for $\beta_{threshold} = 85$ and $W = 3$ with $tpr = 95\%$ and $fpr = 45\%$

Although most of the noise was detected in every best compromise case, false positive rates were much higher for this filter. This may be caused by the fact that these results are very sensitive to the reference positioning since here only the object border, thus very few points, are labelled as noise. The parameters extracted as best compromises here, take into account the score for every object size with the same weight, this induces that pixel size results computed from very few members may be noisy and interfere in the final result. We also need to note that the highest size class for this study was 7 pixels, which is still very small (about 3 cm at 27m), bigger pixel sizes may have yielded better results. The effect of window size versus pixel size is very apparent, it is clear that if $\frac{W}{2} < p_{size}$ the detection performances are consistently bad (with high false positive rates), which is perfectly explained by how the filter operates. Indeed if the object to be filtered occupies less than half of the filter window it is impossible for a valid point to have less than half of the window triangles computed angles to be under the threshold.

Chapter 7

Conclusion

Contents

In this thesis, we proposed several contributions in the domain of TLS point cloud noise modelling and detection. We focused on sky noise, (i.e. noise produced when a AMCW TLS does not get any return) and mixed point noise (i.e. points computed when the TLS was receiving several different return signals).

We first analysed in Chapter 2, how the TLS samples space and deduced properties on how the local point cloud density evolves with respect to the elevation. This allowed us to show the limits of classical density based noise detection techniques. We then oriented our focus on 2D non density based detection techniques.

We review in Chapter 3 the main noise detection techniques and their advantages and inconvenient. Our previous density analysis allowed to pinpoint how most techniques are ill suited for TLS scanning noise detection. We also review the equirectangular projection techniques, applications and the problems reported in the literature when they are applied to TLS scans.

Then, we defined in Chapter 4 a theoretical framework to analyse projection methods, unavoidable foundations for 2D detection methods. This framework allowed us to bring to light two fundamental properties that should be satisfied by a projection. Following these properties, we designed a projection algorithm that satisfied them as much as possible. We then defined a way to quantify projection quality and compared our proposed algorithm with the widely used classic algorithm.

After that, in Chapter 5 we formally analysed sky noise and extracted its fundamental properties. From our projection and the discovered properties, we designed a sky detector and a mixed point detector.

Finally, in Chapter 6 we evaluated our detectors in controlled conditions with an experimental setup reflecting various real world conditions. This analysis allowed us to show the efficiency of our detectors and the optimal ways to configure them.

In the following, we first provide a summary of our contributions. Then, we present the limitations of this work and finally, we provide some interesting future research directions.

7.1 Summary of contributions

Density analysis

To analyse the point cloud density we proposed a model allowing to compute the density augmentation factor, i.e. by how much the point density at the horizon (zero elevation) is multiplied as a function of the elevation and the scan resolution. Deeper analysis allowed us to derive a simpler, resolution independent, model and we expressed the error bound between the complete and the simplified model.

Our density model showed that more that two thirds of any full panorama scan, is at least 10% denser that its horizon density, and one third is more than twice as dense as the horizon density, making classical

density based noise detection more and more inefficient as the elevation grows.

Equirectangular projection

Any image based noise detector must first project scan data on a 2D grid (image) and then locally process that image. Among all projections the equirectangular projection is the most used for its neighbouring properties where neighbours in the projection are angular neighbours (neighbours in the visual field). As Käshammer and Nüchter [2015] pointed out, the classic equirectangular projection algorithm was bringing several distortions and point losses. We thus decided to create a theoretical framework to properly study and define what is a good equirectangular projection applied to TLS scans. That framework allowed us to extract 2 essentials property :

- Lossless projection : Every scan point must be mapped to a unique image pixel
- Coherent projection : All points need to be correctly placed with respect to each other. This property can be divided in two sub properties :
  - Line coherence : All points with a close enough elevation must be mapped to the same line
  - Column coherence : All points acquired during a single eye turn must be mapped to the same column

Taking these properties as guidelines, we built an algorithm that computes a scan equirectangular projection that satisfies these properties as much as possible.

To evaluate and compare the classic and the proposed projection, we proposed a new framework allowing to quantify the quality of a projection via two numeric indicators reflecting how much a given projection satisfies the aforementioned properties :

- Lossless coefficient : The fraction of points mapped to the image
- Coherence coefficient : For a given neighbourhood size, indicates the fraction of points with an entirely correct neighbourhood (i.e. all points in the given neighbourhood are correctly placed with respect to each other)

Frame 7.1 – Fundamental sky noise property

The measured phase will follow a uniform distribution in $[0, \tau]$ whatever the properties of the random input signal (e.g. distribution, mean, variance etc.) as long as this signal is stationary and with finite variance.

The lossless coefficient is easily interpreted as a point loss. The coherence coefficient can be interpreted as a fraction of points, where any local processing in the defined neighbourhood will use coherent sets of points.

Using our evaluation framework we compared the classic equirectangular projection algorithm and the proposed algorithm on four test scans (representing different scanning conditions, like small or large panoramas, indoor or outdoor scanning). The results revealed that the classic projection was unsuitable for 2D detectors, indeed the analysis showed a point loss of about 10% on all scans and a coherence always under 73%, except for the trivial case of a small indoor panorama. The proposed method showed a point loss under 0.1% and a coherence always above 99%.

We concluded that the classic projection cannot be used, except for trivial cases but the proposed projection showed almost excellent results in all cases proving that its perfectly fitted for 2D noise detection.

Sky range noise analysis

To tackle the noise detection problem we first focus on the sky noise. A point of sky noise (a sky point) is point acquired when an AMCW TLS does not get any return signal.

Since that subject was never addressed in the literature, we started by modelling the phenomenon. To model sky noise we considered that, during a sky point acquisition, the TLS was receiving a random stationary signal with finite variance, a coherent hypothesis with background radiation modelling. From this input signal we followed the range measurement process used by the TLS, the four buckets method.

This model allowed us to extract a fundamental property of the sky noise (or any noise produced by the acquisition of a random stationary signal with finite variance) showed in Frame 7.1

Also the fundamental sky property is true for any device using the four buckets methods (e.g. TOF camera). A theoretical proof of this property was proposed to support its validity.

Using this property we were able to simulate an acquisition of sky points. The range distribution of the simulated points was compared with a range distribution of sky points manually extracted from a scan acquired with a Leica HDS6100. This comparison showed perfect similarity between the distribution obtained from our simulation and the distribution obtained from the scanner.

We thus demonstrated by theory and experiments that the sky noise range distribution is always the same, whatever the scan and is only dependant on the modulation wavelengths used by the TLS.

Noise detectors

Sky noise detector

The previously developed sky noise model allowed us to build a sky noise detector to try to solve the sky noise problem.
The designed sky detector operates in 4 steps :

1. Local range variance computation and estimation of the log range variance distribution
2. Extraction of points with a log variance higher that the log variance of the mode of highest log variance
3. Estimation of the sky intensity distribution from the previously extracted points and computation of an intensity threshold for sky detection
4. Detection of isolated points not detected by the intensity threshold

Mixed point noise detector

We then focused on the detection of mixed points, i.e. points acquired when the TLS laser beam hits multiple targets at once. The mixed point detection and modelling problem was widely addressed in the literature. However Huber et al. [2010] points out that this problem is still not fully solved, and that there is still room for improvements.

We decided to base our mixed point detector on the detector proposed by Tang et al. [2007]. Tang's detector showed good performances but it only uses very local information and can adapt the neighbourhood it uses for its computations (which can be important if the detector is used on scans with different resolutions).

The proposed detector and the detector proposed by Tang et al. [2007] rely on computing, for every point, the angle between the acquisition direction at that point and the normal to a triangle formed by that point and two of its neighbours. To define the triangles Tang et al. [2007] used a Triangular Irregular Network, which only defines triangles via the immediate neighbourhood of every points (4 or 8 neighbourhood). Our algorithm uses a sliding window of size given by the user, and consider all triangles that have the window central point as a vertex. This allows for more robustness, especially for "low" resolutions (low angular resolution, i.e. high number of points per turn).

Evaluation in controlled conditions

To evaluate the proposed detectors we proceeded to an evaluation in controlled conditions. Our evaluation focused on two classes of objects :

- Cylinders of different diameters
- Holes of different diameters in a planar object

Several different acquisition conditions were tested : resolution, distance to the studied object, object size and object reflectivity.

The evaluation was based on two complementary approaches :

- Reconstruct the object from the filtered point cloud (filtering a point cloud is removing all detected noise) and compare its dimension with the real object
- Receiver Operating Characteristic (ROC) type analysis, which compares the algorithm labelling (which points it labelled as noise) with a reference labelling

We chose for this analysis not to make the reference labelling by hand (expert labelling) but we went for an automatic labelling.

For the automatic labelling we proposed an edge loss and footprint model allowing better precision than the classical models (conical beam) since it takes into consideration the true shape of the laser beam (under the Gaussian beam approximation) and the discrete nature of TLS sampling.

Using our proposed edge loss model, we were able to automatically label points from semi-automatically recreated cylinders or holes as our reference objects to obtain our reference labelling.

Mixed point detector results

The mixed point detector evaluation showed that it was consistently capable to detect almost all noise (high true positive rates) but with a tendency to over detect (high false positive rates, especially for high points per turn setups). Although, as we will develop in the limitations, part are those results may have been caused by imprecision when recreating the reference objects and the size classes chosen for the analysis.

Sky noise detector results

Sky noise detector analysis revealed good performances for both types of analysis (reconstruction and ROC) and allowed us to extract optimal parameters as a function of TLS resolution. The analysis also showed that the detector could consistently detect almost all noise with few false positives and for all tested resolutions and object reflectivity. Finally the analyses allowed to show the robustness of the detector against external parameter variations (resolution, object size, etc) and internal parameter variations (close results for all windows and $\rho_{sky} \geq 90\%$).

7.2 Limitations

Access to the raw data

The proposed detection methods rely on the proposed equirectangular projection. This projection uses the acquisition order for better projection quality. Then the projection must be applied to raw data since usual manufacturer software automatically rearrange the point cloud. This can be a real hindrance since some manufacturers do not provide any tool to extract raw data without using their software.

Experimental setup : references

We tried to evaluate our detector without using an expert labelling since mixed points (especially mixed points that imply mostly one surface) can be hard to distinguish from valid points. We circumvented that problem by reconstructing the objects being studied in all scans and using

our proposed edge loss model to create labelled references. However, since zones with mixed points are very narrow, this analysis was very sensitive to reference placement and some objects (especially cylinders at high distance) were impossible to recreate without placing them manually. To use a similar analysis one can compute, via our proposed formulae and models, the pixel size (taking the noise into account) of every objects. Every object with a pixel size superior to 10 should be properly recreated using our framework.

7.3 Future works

Order independent projection

We showed in Chapter 4 the importance of the projection method in any image based method. However, as we exposed in the limitation section, our proposed projection method can be inapplicable if one does not have access to the raw data or the scan in acquisition order. Then we think that the study of equirectangular projection for TLS would be very valuable since so much application rely on an equirectangular projection.

Image based compression

One of the very profitable areas that could benefit from good equirectangular projection is point cloud compression. Indeed Houshiar and Nüchter [2015] already started to explore image based compression with very promising results. Using more efficient projections would allow for fast, almost lossless and effective compression. Indeed, lossless compression schemes like PNG compression rely on the local similarity of the image to attain good compression rates. Projections with good coherence and lossless properties would allow for a better exploitation of local similarities often found in natural scenes (e.g. planar objects) with minimal loss.

Mixed point noise correction

Although capital for most applications, noise detection and removal still can degrade some important point cloud features. Indeed, by definition mixed points happen at object edges which can be critical for object size determination. A better approach for AMCW TLS would be to detect and correct noise. Noise correction as already been attempted (e.g.

Larkins et al. [2009]) but no correction methods was based on an actual range measurement model. Using a TLS range measurement model could allow for accurate mixed point range correction.

TLS modulation wavelength estimation

To apply TLS range measurement model based techniques one must know the modulation wavelengths used by the TLS. As we have discussed in Chapter 5 some modulation wavelengths can be extracted by measuring some point cloud features. However some of these features like the jump distance can be very hard to measure accurately. As we proved in Chapter 5 the range distribution of sky points is only dependant on the modulation wavelengths, then further analysis may yield methods to precisely compute modulation wavelengths from an estimated sky range distribution.

Bibliography

M. D. Adams and P. J. Probert. The interpretation of phase and intensity data from amcw light detection sensors for reliable ranging. *The International journal of robotics research*, 15(5):441–458, 1996. (Cited on page 28.)

M. Béland, J.-L. Widlowski, R. A. Fournier, J.-F. Côté, and M. M. Verstraete. Estimating leaf area distribution in savanna trees from terrestrial lidar measurements. *Agricultural and Forest Meteorology*, 151(9):1252–1266, 2011. (Cited on page 4.)

F. Bosché, M. Ahmed, Y. Turkan, C. T. Haas, and R. Haas. The value of integrating scan-to-bim and scan-vs-bim techniques for construction monitoring using laser scanning and bim: The case of cylindrical mep components. *Automation in Construction*, 49:201–213, 2015. (Cited on page 2.)

Z.-x. Cai, J.-x. Yu, X.-b. Zou, and Z.-h. Duan. A 3-d perceptual method based on laser scanner for mobile robot. In *2005 IEEE International Conference on Robotics and Biomimetics-ROBIO*, pages 658–663. IEEE, 2005. (Cited on pages 6 and 38.)

R. Cifuentes, D. Van der Zande, C. Salas, J. Farifteh, and P. Coppin. Correction of erroneous lidar measurements in artificial forest canopy experimental setups. *Forests*, 5(7):1565–1583, 2014. (Cited on pages 6, 31, 35, and 38.)

M. Dassot, T. Constant, and M. Fournier. The use of terrestrial lidar technology in forest science: application fields, benefits and challenges. *Annals of forest science*, 68(5):959–974, 2011. (Cited on pages 2 and 3.)

J. Digne and C. De Franchis. The bilateral filter for point clouds. 2017. (Cited on page 28.)

K. L. El-Ashmawy. A simple technique for road surface modelling. *Geodesy and Cartography*, 42(3):106–114, 2016. (Cited on page 2.)

L. Eysn, N. Pfeifer, C. Ressl, M. Hollaus, A. Grafl, and F. Morsdorf. A practical approach for extracting tree models in forest environments based on equirectangular projections of terrestrial laser scans. *Remote Sensing*, 5(11):5424–5448, 2013. (Cited on pages 7, 33, and 64.)

FARO Technologies Inc. Faro focus s350 tech sheet. https://faro.app.box.com/s/kcxnsakrd9bioivzwvsb2lbsrbcwe2x5/file/391565112686. Accessed: 2019-10-04. (Cited on page 24.)

J. Hackenberg, M. Wassenberg, H. Spiecker, and D. Sun. Non destructive method for biomass prediction combining tls derived tree volume and wood density. *Forests*, 6(4):1274–1300, 2015. (Cited on page 29.)

H. Houshiar and A. Nüchter. 3d point cloud compression using conventional image compression for efficient data transmission. In *2015 XXV International Conference on Information, Communication and Automation Technologies (ICAT)*, pages 1–8. IEEE, 2015. (Cited on pages 7, 33, 34, and 138.)

H. Houshiar, D. Borrmann, J. Elseberg, and A. Nüchter. Panorama based point cloud reduction and registration. In *2013 16th International Conference on Advanced Robotics (ICAR)*, pages 1–8. IEEE, 2013. (Cited on page 7.)

H. Houshiar, J. Elseberg, D. Borrmann, and A. Nüchter. A study of projections for key point based registration of panoramic terrestrial 3d laser scan. *Geo-spatial Information Science*, 18(1):11–31, 2015. (Cited on page 33.)

D. Huber, B. Akinci, P. Tang, A. Adan, B. Okorn, and X. Xiong. Using laser scanners for modeling and analysis in architecture, engineering, and construction. In *2010 44th Annual Conference on Information Sciences and Systems (CISS)*, pages 1–6. IEEE, 2010. (Cited on pages 5 and 135.)

M. Jaboyedoff, T. Oppikofer, A. Abellán, M.-H. Derron, A. Loye, R. Metzger, and A. Pedrazzini. Use of lidar in landslide investigations: a review. *Natural hazards*, 61(1):5–28, 2012. (Cited on pages 2 and 3.)

W. Jouini, D. Le Guennec, C. Moy, and J. Palicot. Log-normal approximation of chi-square distributions for signal processing. In *2011 XXXth URSI General Assembly and Scientific Symposium*, pages 1–4. IEEE, 2011. (Cited on page 76.)

S. Kaasalainen, A. Jaakkola, M. Kaasalainen, A. Krooks, and A. Kukko. Analysis of incidence angle and distance effects on terrestrial laser scanner intensity: Search for correction methods. *Remote Sensing*, 3 (10):2207–2221, 2011. (Cited on page 84.)

P. Käshammer and A. Nüchter. Mirror identification and correction of 3d point clouds. *The International Archives of Photogrammetry, Remote Sensing and Spatial Information Sciences*, 40(5):109, 2015. (Cited on pages 7, 33, 34, and 133.)

F. Lafarge. Some new research directions to explore in urban reconstruction. In *2015 Joint Urban Remote Sensing Event (JURSE)*, pages 1–4. IEEE, 2015. (Cited on page 4.)

R. L. Larkins, M. J. Cree, A. A. Dorrington, and J. P. Godbaz. Surface projection for mixed pixel restoration. In *2009 24th International Conference Image and Vision Computing New Zealand*, pages 431–436. IEEE, 2009. (Cited on pages 32, 35, and 139.)

Leica Geosystems. Leica p50 tech sheet. https://leica-geosystems.com/-/media/files/leicageosystems/products/datasheets/scan/leica%20scanstation%20p50%20ds%20869145%200119%20en%20lr.ashx?la=en-gb&hash=A0D6377040E275EA08B61B301BCB735B. Accessed: 2019-10-04. (Cited on page 24.)

J. L. Lerma, S. Navarro, M. Cabrelles, and V. Villaverde. Terrestrial laser scanning and close range photogrammetry for 3d archaeological documentation: the upper palaeolithic cave of parpalló as a case study. *Journal of Archaeological Science*, 37(3):499–507, 2010. (Cited on pages 2 and 3.)

X. Liang, V. Kankare, J. Hyyppä, Y. Wang, A. Kukko, H. Haggrén, X. Yu, H. Kaartinen, A. Jaakkola, F. Guan, et al. Terrestrial laser scanning in forest inventories. *ISPRS Journal of Photogrammetry and Remote Sensing*, 115:63–77, 2016. (Cited on pages 2, 3, and 64.)

P. Milonni and J. Eberly. Laser resonators and gaussian beams. In *Laser Physics*, chapter 7, pages 269–329. John Wiley & Sons, Ltd, 2010. (Cited on page 20.)

W. Mukupa, G. W. Roberts, C. M. Hancock, and K. Al-Manasir. A review of the use of terrestrial laser scanning application for change detection

and deformation monitoring of structures. *Survey Review*, 49(353): 99–116, 2017. (Cited on page 2.)

M.-J. Rakotosaona, V. La Barbera, P. Guerrero, N. J. Mitra, and M. Ovsjanikov. Pointcleannet: Learning to denoise and remove outliers from dense point clouds. In *Computer Graphics Forum*. Wiley Online Library, 2019. (Cited on page 30.)

P. Raumonen, M. Kaasalainen, M. Åkerblom, S. Kaasalainen, H. Kaartinen, M. Vastaranta, M. Holopainen, M. Disney, and P. Lewis. Fast automatic precision tree models from terrestrial laser scanner data. *Remote Sensing*, 5(2):491–520, 2013. (Cited on pages 28 and 29.)

RIEGL Laser Measurement Systems. Riegl vz-400i tech sheet. http://www.riegl.com/uploads/tx_pxpriegldownloads/RIEGL_VZ-400i_Datasheet_2019-09-02.pdf. Accessed: 2019-10-04. (Cited on page 24.)

P. Tang, D. Huber, and B. Akinci. A comparative analysis of depth-discontinuity and mixed-pixel detection algorithms. In *Sixth International Conference on 3-D Digital Imaging and Modeling (3DIM 2007)*, pages 29–38. IEEE, 2007. (Cited on pages 6, 31, 32, 33, 34, 35, 38, 64, 81, and 136.)

G. R. Terrell and D. W. Scott. Oversmoothed nonparametric density estimates. *Journal of the American Statistical Association*, 80(389):209–214, 1985. (Cited on pages 72 and 76.)

A. Topol, M. Jenkin, J. Gryz, S. Wilson, M. Kwietniewski, P. Jasiobedzki, H.-K. Ng, and M. Bondy. Generating semantic information from 3d scans of crime scenes. In *2008 Canadian Conference on Computer and Robot Vision*, pages 333–340. IEEE, 2008. (Cited on page 2.)

J. Tuley, N. Vandapel, and M. Hebert. Analysis and removal of artifacts in 3-d ladar data. In *Proceedings of the 2005 IEEE International Conference on Robotics and Automation*, pages 2203–2210. IEEE, 2005. (Cited on pages 28 and 29.)

Q. Wang, H. Sohn, and J. C. Cheng. Development of a mixed pixel filter for improved dimension estimation using amcw laser scanner. *ISPRS Journal of Photogrammetry and Remote Sensing*, 119:246–258, 2016. (Cited on pages 30 and 68.)

X. Xiong, A. Adan, B. Akinci, and D. Huber. Automatic creation of semantically rich 3d building models from laser scanner data. *Automation in construction*, 31:325–337, 2013. (Cited on page 35.)

Appendix A

Proofs

A.1 Proofs of the spherical density Theorems

Density function

To compute the local point cloud density, consider a cone $\mathcal{C}$ with directing axis (OP) with O the point cloud origin and P a scan point, and aperture angle α. Let's fist compute the number of points N captured inside of the cone. The number of points inside $\mathcal{C}$ on the line of constant elevation n is given by :

$$n = \frac{2\alpha}{\delta_\varphi} \tag{A.1}$$

$$\tag{A.2}$$

where δ_φ is the angle between two point at the same elevation and with azimuth φ and $\varphi + \delta$. Let P_1 and P_2 be two points at coordinates (R_1, θ, φ) and $(R_2, \theta, \varphi + \delta)$, we have :

$$P_1 = R_1 \begin{pmatrix} \cos(\theta)\ \cos(\varphi) \\ \cos(\theta)\ \sin(\varphi) \\ \sin(\theta) \end{pmatrix} \tag{A.3}$$

$$P_2 = R_2 \begin{pmatrix} \cos(\theta)\ \cos(\varphi + \delta) \\ \cos(\theta)\ \sin(\varphi + \delta) \\ \sin(\theta) \end{pmatrix} \tag{A.4}$$

$$\vec{u_1} = \begin{pmatrix} \cos(\theta)\ \cos(\varphi) \\ \cos(\theta)\ \sin(\varphi) \\ \sin(\theta) \end{pmatrix} \tag{A.5}$$

$$\vec{u_2} = \begin{pmatrix} \cos(\theta)\ \cos(\varphi+\delta) \\ \cos(\theta)\ \sin(\varphi+\delta) \\ \sin(\theta) \end{pmatrix} \tag{A.6}$$

$$\delta_\varphi = \arccos(\vec{u_1} \cdot \vec{u_2}) \tag{A.7}$$

$$\vec{u_1} \cdot \vec{u_2} = \cos(\theta)^2(\cos(\varphi)\cos(\varphi+\delta) + \sin(\varphi)\sin(\varphi+\delta)) + \sin(\theta)^2 \tag{A.8}$$

$$\vec{u_1} \cdot \vec{u_2} = \cos(\theta)^2 \cos(\varphi+\delta-\varphi) + \sin(\theta)^2 \tag{A.9}$$

$$\vec{u_1} \cdot \vec{u_2} = \cos(\theta)^2 \cos(\delta) + \sin(\theta)^2 \tag{A.10}$$

Finally :

$$\delta_\varphi(\delta,\theta) = \arccos\big(\cos(\theta)^2 \cos(\delta) + \sin(\theta)^2\big) \tag{A.11}$$

The number of lines of constant elevation that passes through $\mathcal{C}$ m is given by :

$$m = \frac{2\alpha}{\delta} \tag{A.12}$$

(A.13)

We can compute the number of points in $\mathcal{C}$ by summing the number of points per line of constant elevation. The number of points captured in $\mathcal{C}$ in a line, k lines above the line passing through the cone axis n_k is given in Equation (A.14)

$$n_k(\delta,\theta) = n(\delta,\theta)\sqrt{1-\left(\frac{k\delta}{\alpha}\right)^2} \tag{A.14}$$

Finally the number of points in $\mathcal{C}$ is given Equation (A.15)

$$N(\delta,\theta) = 2n(\delta,\theta)\sum_{k=0}^{\frac{m}{2}}\sqrt{1-\left(\frac{k\delta}{\alpha}\right)^2} \tag{A.15}$$

The number of points at $\theta = 0$ is from Equation (A.15) :

$$N(\delta,0) = \frac{4\alpha}{\delta}\sum_{k=0}^{\frac{m}{2}}\sqrt{1-\left(\frac{k\delta}{\alpha}\right)^2} \tag{A.16}$$

And finally we can deduce the density augmentation factor D i.e. the factor by which the point density at $\theta = 0$ is multiplied :

$$D(\delta,\theta) = \frac{N(\delta,\theta)}{N(\delta,0)} = \frac{\delta}{\delta_{\varphi}(\delta,\theta)} \tag{A.17}$$

Let :

$$D(\delta,\theta) = \frac{\delta}{\arccos\left(\cos(\delta)\cos(\theta)^2 + \sin(\theta)^2\right)}$$

Since δ represents the scanner resolution, we will usually have $\delta \ll 1$ and $\delta > 0$. Let's consider :

$$\lim_{\delta\to 0} D(\delta,\theta) = \lim_{\delta\to 0}\frac{\delta}{\arccos\left(\cos(\delta)\cos(\theta)^2 + \sin(\theta)^2\right)} \tag{A.18}$$

Using l'Hôpital's rule :

$$\lim_{\delta\to 0} D(\delta,\theta) = \lim_{\delta\to 0}\frac{\sqrt{1-\left(\cos(\delta)\cos(\theta)^2 + \sin(\theta)^2\right)^2}}{\sin(\delta)\cos(\theta)^2} \tag{A.19}$$

$$\lim_{\delta\to 0} D(\delta,\theta) = \lim_{\delta\to 0}\frac{\sqrt{1-\left(\cos(\delta)^2\cos(\theta)^4 + 2\cos(\delta)\cos(\theta)^2\sin(\theta)^2 + \sin(\theta)^4\right)}}{\sin(\delta)\cos(\theta)^2} \tag{A.20}$$

Taylor expansion :

$$\lim_{\delta\to 0} D(\delta,\theta) = \lim_{\delta\to 0} \frac{\sqrt{1-\left((1-\delta^2)\cos(\theta)^4 + 2\left(1-\frac{\delta^2}{2}\right)\cos(\theta)^2\sin(\theta)^2 + \sin(\theta)^4\right)}}{\delta\cos(\theta)^2} \tag{A.21}$$

$$\lim_{\delta\to 0} D(\delta,\theta) = \lim_{\delta\to 0} \frac{\sqrt{1-1+\delta^2\left(\cos(\theta)^4 + \cos(\theta)^2\sin(\theta)^2\right)}}{\delta\cos(\theta)^2} \tag{A.22}$$

$$\lim_{\delta\to 0} D(\delta,\theta) = \lim_{\delta\to 0} \frac{\sqrt{\delta^2\cos(\theta)^2\left(\cos(\theta)^2 + \sin(\theta)^2\right)}}{\delta\cos(\theta)^2} \tag{A.23}$$

$$\lim_{\delta\to 0} D(\delta,\theta) = \frac{1}{\cos(\theta)} \tag{A.24}$$

Let

$$D^*(\theta) = \lim_{\delta\to 0} D(\delta,\theta) = \frac{1}{\cos(\theta)} \tag{A.25}$$

We will then prove the density theorems using the notations in this section.

Proof of the Density bounds theorem

Theorem 1. ***Density bounds theorem***

$$\forall\delta \in \left[0, \frac{\tau}{2}\right], \forall\theta,\ D^*(\theta) \leq D(\delta,\theta) \leq \frac{D^*(\theta)}{\operatorname{sinc}\left(\frac{\delta}{2}\right)}$$

Proof. Let's consider Err the relative error between D and D^* :

$$Err(\delta,\theta) = \frac{D(\delta,\theta) - D^*(\theta)}{D(\delta,\theta)} \tag{A.26}$$

To prove Theorem 1 we must prove that Err is bounded and express its bounds.

Let's consider :

$$f(\delta,\theta) = \frac{D(\delta,\theta)}{D^*(\theta)} = \frac{\delta\cos(\theta)}{\arccos\left(\cos(\delta)\cos(\theta)^2 + \sin(\theta)^2\right)} \tag{A.27}$$

Let's compute $f(\delta, \theta)$ for $\theta = 0$ and $\theta = \frac{\pi}{2}$

$$f(\delta, 0) = 1 \tag{A.28}$$

$$\lim_{\theta \to \frac{\pi}{2}} f(\delta, \theta) = \lim_{\theta \to \frac{\pi}{2}} \frac{\delta \cos(\theta)}{\arccos\left(\cos(\delta)\cos(\theta)^2 + \sin(\theta)^2\right)} \tag{A.29}$$

$$\lim_{\theta \to \frac{\pi}{2}} f(\delta, \theta) = \lim_{t \to 0} \frac{\delta \cos\left(\frac{\pi}{2} - t\right)}{\arccos\left(\cos(\delta)\cos\left(\frac{\pi}{2} - t\right)^2 + \sin\left(\frac{\pi}{2} - t\right)^2\right)} \tag{A.30}$$

$$\lim_{\theta \to \frac{\pi}{2}} f(\delta, \theta) = \lim_{t \to 0} \frac{\delta \sin(t)}{\arccos\left(\cos(\delta)\sin(t)^2 + \cos(t)^2\right)} \tag{A.31}$$

Using l'Hôpital's rule :

$$\lim_{\theta \to \frac{\pi}{2}} f(\delta, \theta) = \lim_{t \to 0} \frac{\delta \cos(t)\sqrt{1 - \left(\cos(\delta)\sin(t)^2 + \cos(t)^2\right)^2}}{2(1 - \cos(\delta))\sin(t)\cos(t)} \tag{A.32}$$

Taylor expansion :

$$\lim_{\theta \to \frac{\pi}{2}} f(\delta, \theta) = \lim_{t \to 0} \frac{\delta\sqrt{1 - \left(\cos(\delta)t^2 + 1 - t^2\right)^2}}{2(1 - \cos(\delta))\, t} \tag{A.33}$$

$$\lim_{\theta \to \frac{\pi}{2}} f(\delta, \theta) = \lim_{t \to 0} \frac{\delta\sqrt{1 - \left(1 + 2(\cos(\delta) - 1)\, t^2\right)}}{2(1 - \cos(\delta))\, t} \tag{A.34}$$

$$\lim_{\theta \to \frac{\pi}{2}} f(\delta, \theta) = \frac{\sqrt{2}}{2} \frac{\delta}{\sqrt{1 - \cos(\delta)}} \tag{A.35}$$

If $f(\delta, \theta)$ is monotonic in θ, then :

$$\forall \delta, \forall \theta, 1 \leq f(\delta, \theta) \leq \frac{\sqrt{2}}{2} \frac{\delta}{\sqrt{1 - \cos(\delta)}} \tag{A.36}$$

We must now prove that f is monotonic in θ. We have :

$$\frac{\partial f}{\partial \theta}(\delta,\theta) = F(\delta,\theta)\, G(\delta,\theta) \tag{A.37}$$

$$F(\delta,\theta) = \frac{2(1-\cos(\delta))\cos(\theta)^2}{\sqrt{1-\left(\cos(\delta)\cos(\theta)^2+\sin(\theta)^2\right)^2}} - \arccos\left(\cos(\delta)\cos(\theta)^2+\sin(\theta)^2\right) \tag{A.38}$$

$$G(\delta,\theta) = \frac{\delta\sin(\theta)}{\arccos\left(\cos(\delta)\cos(\theta)^2+\sin(\theta)^2\right)^2} \tag{A.39}$$

It is obvious that G is positive for $\delta > 0$ and $\theta \in \left[0, \frac{\tau}{2}\right]$.
Let :

$$h(\delta,\theta) = \cos(\delta)\cos(\theta)^2 + \sin(\theta)^2 \tag{A.40}$$

then :

$$h(\delta,\theta) = 1 - (1-\cos(\delta))\cos(\theta)^2 \tag{A.41}$$

Thus $h(\delta,\theta)$ has the same monotonicity than $-\cos(\theta)^2$ for $\theta \in \left[0, \frac{\tau}{4}\right]$ i.e. monotonically increasing. Also $h(\delta,0) = \cos(\delta)$ and $\cos(\delta) > 0$ thus $h(\delta,\theta)$ is positive for $\theta \in \left[0, \frac{\tau}{4}\right]$ and $\cos(\delta) \leq h(\delta,\theta) \leq 1$.
from (A.41) :

$$\cos(\theta)^2 = \frac{1-h(\delta,\theta)}{1-\cos(\delta)} \tag{A.42}$$

By substituting (A.42) in (A.38) :

$$F(\delta,\theta) = \frac{2(1-h(\delta,\theta))}{\sqrt{1-h(\delta,\theta)^2}} - \arccos(h(\delta,\theta)) \tag{A.43}$$

Let :

$$g(x) = \frac{2(1-x)}{\sqrt{1-x^2}} - \arccos(x) \tag{A.44}$$

We have :

$$F(\delta,\theta) = (g \circ h)(\delta,\theta) \tag{A.45}$$

And :

$$\frac{dg}{dx}(x) = \frac{x-1}{(1+x)\sqrt{1-x^2}} \tag{A.46}$$

$$\lim_{x\to 1} g(x) = \lim_{x\to 1} \frac{2(1-x)}{\sqrt{1-x^2}} - \arccos(x) \tag{A.47}$$

$$\lim_{x\to 1} g(x) = \lim_{t\to 0} \frac{2(1-1+t)}{\sqrt{1-(1-t)^2}} - \arccos(1-t) \tag{A.48}$$

$$\lim_{x\to 1} g(x) = \lim_{t\to 0} \frac{2t}{\sqrt{2t-t^2}} \tag{A.49}$$

$$\lim_{x\to 1} g(x) = \lim_{t\to 0} \sqrt{t}\frac{2}{\sqrt{2-t}} \tag{A.50}$$

$$\lim_{x\to 1} g(x) = 0 \tag{A.51}$$

$\frac{dg}{dx}(x)$ is negative for $x \in [0,1]$ and $\lim_{x\to 1} g(x) = 0$ thus $g(x)$ is positive and monotonically decreasing for $x \in [0,1]$.

Since $g(x)$ is monotonically decreasing and positive for $x \in [0,1]$ and $h(\delta,\theta)$ is monotonically increasing and $0 \leq h(\delta,\theta) \leq 1$ for $\theta \in \left[0, \frac{\tau}{4}\right]$, then $(g \circ h)(\delta,\theta)$ is positive and monotonically decreasing for $\theta \in \left[0, \frac{\tau}{4}\right]$.

Thus we have proven that $\frac{\partial f}{\partial \theta}(\delta,\theta)$ is positive for $\theta \in \left[0, \frac{\tau}{4}\right]$, then $f(\delta,\theta)$ is monotonically increasing for $\theta \in \left[0, \frac{\tau}{4}\right]$ which proves that :

$$\forall\delta, \forall\theta,\ 1 \leq f(\delta,\theta) \leq \frac{\sqrt{2}}{2}\frac{\delta}{\sqrt{1-\cos(\delta)}} \tag{A.52}$$

From (A.52) we can deduce the following bounds on $Err(\delta,\theta)$:

$$\forall\delta, \forall\theta,\ 0 \leq Err(\delta,\theta) \leq 1 - \sqrt{2}\frac{\sqrt{1-\cos(\delta)}}{\delta} \tag{A.53}$$

And we have, for $\delta \in [0, \frac{\tau}{2}]$

$$\sqrt{2}\frac{\sqrt{1-\cos(\delta)}}{\delta} = \sqrt{2}\frac{\sqrt{1-\left(\cos\left(\frac{\delta}{2}\right)^2 - \sin\left(\frac{\delta}{2}\right)^2\right)}}{\delta} \tag{A.54}$$

$$= \sqrt{2}\frac{\sqrt{1-\left(1-2\sin\left(\frac{\delta}{2}\right)^2\right)}}{\delta} \tag{A.55}$$

$$= \frac{2\sin\left(\frac{\delta}{2}\right)}{\delta} \tag{A.56}$$

$$= \operatorname{sinc}\left(\frac{\delta}{2}\right) \tag{A.57}$$

and finally :

$$\forall \delta \in \left[0, \frac{\tau}{2}\right], \forall \theta,\ 0 \leq Err(\delta, \theta) \leq 1 - \operatorname{sinc}\left(\frac{\delta}{2}\right) \tag{A.58}$$

Then rearranging Equation (A.58) yields Equation (A.59)

$$\forall \delta \in \left[0, \frac{\tau}{2}\right], \forall \theta,\ D^*(\theta) \leq D(\delta, \theta) \leq \frac{D^*(\theta)}{\operatorname{sinc}\left(\frac{\delta}{2}\right)} \tag{A.59}$$

Proving Theorem 1

□

Proof of the Density approximation theorem

Theorem 2. ***Density approximation theorem***

$$\forall \varepsilon > 0, \exists \delta_{lim} \geq \sqrt{24\varepsilon}\ s.t.\ \forall \delta \leq \delta_{lim}, \forall \theta, Err(\delta, \theta) \leq \varepsilon$$

Proof. For $\delta \ll 1$ the Taylor series applied to the upper bound of Err given by Theorem 1 yields :

$$1 - \operatorname{sinc}\left(\frac{\delta}{2}\right) = 1 - \left(1 - \frac{\delta^2}{24} + O\left(\delta^4\right)\right) \tag{A.60}$$

$$1 - \operatorname{sinc}\left(\frac{\delta}{2}\right) = \frac{\delta^2}{24} - O\left(\delta^4\right) \tag{A.61}$$

$$1 - \operatorname{sinc}\left(\frac{\delta}{2}\right) \leq \frac{\delta^2}{24} \tag{A.62}$$

Therefore, from Equation (A.58) and (A.62) :

$$Err(\delta, \theta) \leq \frac{\delta^2}{24} \tag{A.63}$$

$$\tag{A.64}$$

Then for a given error tolerance ε :

$$\frac{\delta^2}{24} \leq \varepsilon \implies Err(\delta, \theta) \leq \varepsilon \tag{A.65}$$

From proposition (A.65) it follows that :

$$\forall \theta, Err\left(\sqrt{24\varepsilon}, \theta\right) \leq \varepsilon \tag{A.66}$$

$$\tag{A.67}$$

And finally :

$$\forall \theta, \forall \varepsilon > 0, \forall \delta \leq \sqrt{24\varepsilon}, Err(\delta, \theta) \leq \varepsilon \tag{A.68}$$

Which proves Theorem 2

□

A.2 Proof of the Phase distribution Theorem

Theorem 3. ***Phase distribution theorem***
$r(t)$ is a stationary random process with finite variance $\implies \Phi \sim \mathcal{U}(0, \tau)$

Proof. During the acquisition of a sky point we have $r(t) = X(t)$. The TLS must discretise all signals for numeric processing, we'll use the following notations :

- n the number of samples recorded per period
- N the number of periods on which the cross-correlation is computed
- K the total number of samples used to compute a cross-correlation value ($K = nN$)
- $X_i = r\left(i\frac{\tau}{n}\right)$ a recorded sample
- $C(i)$ a point of the discrete cross-correlation
- Φ the measured phase random variable

The discretised sent signal $s(i)$ is given by :

$$s(i) = a\cos\left(\frac{i\tau}{n}\right) \tag{A.69}$$

The discrete cross correlation is given by :

$$C(i) = \frac{1}{K}\sum_{k=-\frac{K}{2}}^{\frac{K}{2}} s(k)X_{i+k} \tag{A.70}$$

Note that :

$$\forall\theta, \forall k, \cos(\theta) = \cos(\theta + k\tau) \tag{A.71}$$
$$\forall\theta, \forall k, \cos(\theta) = \cos(-k\tau - \theta) \tag{A.72}$$

From Equations (A.71) and (A.72) we have :

$$\forall i, \forall k, s(i) = s(i + kn) \tag{A.73}$$
$$\forall i, \forall k, s(i) = s(-kn - i) \tag{A.74}$$

Using the properties given Equations (A.73) and (A.74), Equation (A.70) can be rewritten as :

$$C(i) = \frac{1}{nN} \sum_{j=0}^{\frac{n}{2}} s(j) \sum_{k=-N}^{N} (X_{i+j+kn} + X_{i-j-kn}) \tag{A.75}$$

Let :

$$Y_{i,j} = \frac{1}{N} \sum_{k=-N}^{N} (X_{i+j+kn} + X_{i-j-kn}) \tag{A.76}$$

Since all X_i are independent, identically distributed with mean μ and with finite variance σ^2, for big enough N (in practice, here $N > 15$ is enough), we can apply the Central Limit Theorem :

$$\forall (i,j), Y_{i,j} \sim \mathcal{N}\left(2\mu, \frac{2\sigma^2}{N}\right) \tag{A.77}$$

where $\mathcal{N}(\mu, \sigma^2)$ is the normal distribution with mean μ and variance σ^2.

Equation (A.75) can now be written as :

$$C(i) = \frac{1}{n} \sum_{j=0}^{\frac{n}{2}} s(j) Y_{i,j} \tag{A.78}$$

Then :

$$C(i) \sim \mathcal{N}\left(\frac{2\mu}{n} \sum_{j=0}^{\frac{n}{2}} s(j), \frac{2\sigma^2}{n^2 N} \sum_{j=0}^{\frac{n}{2}} s(j)^2\right) \tag{A.79}$$

We have now characterised the cross-correlation if $r(t)$ is a stationary random process with finite variance, completing step 2 of the process presented Frame 5.1. We must now determine how the cross-correlation will impact the phase calculation.

Let :

$$U = \frac{2\mu}{n} \sum_{j=0}^{\frac{n}{2}} s(j) \tag{A.80}$$

$$\Sigma = \frac{2\sigma^2}{n^2 N} \sum_{j=0}^{\frac{n}{2}} s(j)^2 \tag{A.81}$$

$$\forall i, W_i \sim \mathcal{N}(0,1) \tag{A.82}$$

Then the cross-correlation signal can be written as :

$$C(i) = U + \Sigma W_i \tag{A.83}$$

Considering that the phase is computed with Equation (5.12). Let the four sampling point be :

$$i_1 = 0 \tag{A.84}$$

$$i_2 = \frac{n}{4} \tag{A.85}$$

$$i_2 = \frac{n}{2} \tag{A.86}$$

$$i_4 = \frac{3n}{4} \tag{A.87}$$

Let Γ be the r.v. described by :

$$\Gamma = \arctan\left(\frac{C(i_4) - C(i_2)}{C(i_1) - C(i_3)}\right) \tag{A.88}$$

Using (A.83) yields :

$$\Gamma = \arctan\left(\frac{W_{i_4} - W_{i_2}}{W_{i_1} - W_{i_2}}\right) \tag{A.89}$$

And the difference of two normal distribution is again a normal distribution :

$$\Gamma = \arctan\left(\frac{2W'_1}{2W'_2}\right) \tag{A.90}$$

$$\Gamma = \arctan\left(\frac{W'_1}{W'_2}\right) \tag{A.91}$$

$$W'_i \sim \mathcal{N}(0,1) \tag{A.92}$$

Let :

$$Z = \frac{W_1'}{W_2'} \tag{A.93}$$

Then Z follows a standard Cauchy distribution,

$$Z \sim \text{Cauchy}(0, 1) \tag{A.94}$$

and

$$\Gamma = \arctan(Z) \tag{A.95}$$

If F_Z is the cumulative distribution function for the r.v. Z, we have :

$$F_Z(z) = \mathbb{P}(Z \leq z) \tag{A.96}$$

$$F_Z(z) = \frac{1}{\pi}\arctan(z) + \frac{1}{2} \tag{A.97}$$

And if F_Γ is the cumulative distribution function for the r.v. Γ, we have :

$$F_\Gamma(\gamma) = \mathbb{P}(\Gamma \leq \gamma) \tag{A.98}$$

$$F_\Gamma(\gamma) = \mathbb{P}(\arctan(Z) \leq \gamma) \tag{A.99}$$

$$\tag{A.100}$$

Since $\gamma \in \left[-\frac{\tau}{4}, \frac{\tau}{4}\right]$:

$$\arctan(Z) \leq \gamma \iff Z \leq \tan(\gamma) \tag{A.101}$$

Equation (A.101) implies :

$$F_\Gamma(\gamma) = \mathbb{P}(\Gamma \leq \gamma) \tag{A.102}$$

$$F_\Gamma(\gamma) = \mathbb{P}(\arctan(Z) \leq \gamma) \tag{A.103}$$

$$F_\Gamma(\gamma) = \mathbb{P}(Z \leq \tan(\gamma)) \tag{A.104}$$

$$F_\Gamma(\gamma) = F_Z(\tan(\gamma)) \tag{A.105}$$

$$F_\Gamma(\gamma) = \frac{\gamma}{\pi} + \frac{1}{2} \tag{A.106}$$

$$f_\Gamma(\gamma) = \frac{1}{\pi} \tag{A.107}$$

$$\Gamma \sim \mathcal{U}\left(-\frac{\tau}{4}, \frac{\tau}{4}\right) \tag{A.108}$$

We know that :

$$\Phi = \text{arctan2}(W_1', W_2') \tag{A.109}$$

To determine the distribution of Φ we must consider each sign case for $\text{arctan2}(W_2', W_1')$.

Case $W_1' > 0$ **and** $W_2' > 0$

In that case we have :

$$\Phi = \arctan\left(\frac{W_1'}{W_2'}\right) \tag{A.110}$$

Let $\mathcal{W}_1$ be the proposition $W_1' > 0, W_2' > 0$. Such restrictions on W_1' and W_2' implies restrictions on Φ :

$$\mathcal{W}_1 \iff \Phi \in \left[0, \frac{\tau}{4}\right] \tag{A.111}$$

And for $\phi \in \left[0, \frac{\tau}{4}\right]$

$$\mathbb{P}(\Phi \leq \phi) = \mathbb{P}(\Gamma \leq \phi \mid \mathcal{W}_1)\, \mathbb{P}(\mathcal{W}_1) \tag{A.112}$$

$$\mathbb{P}(\Phi \leq \phi) = 2\mathbb{P}(0 \leq \Gamma \leq \phi)\, \frac{1}{4} \tag{A.113}$$

$$\mathbb{P}(\Phi \leq \phi) = \frac{1}{2}(\mathbb{P}(\Gamma \leq \phi) - \mathbb{P}(\Gamma \leq 0)) \tag{A.114}$$

From Equations (A.111) and (A.114) we have :

$$\forall \phi \leq \frac{\tau}{4}, \mathbb{P}(\Phi \leq \phi) = \frac{\phi}{\tau} \tag{A.115}$$

Case $W_1' > 0$ **and** $W_2' < 0$

In that case we have :

$$\Phi = \arctan\left(\frac{W_1'}{W_2'}\right) + \frac{\tau}{2} \tag{A.116}$$

Let $\mathcal{W}_2$ be the proposition $W_1' > 0, W_2' < 0$. Such restrictions on W_1' and W_2' implies restrictions on Φ :

$$\mathcal{W}_2 \iff \Phi \in \left[\frac{\tau}{4}, \frac{\tau}{2}\right] \tag{A.117}$$

And for $\phi \in \left[\frac{\tau}{4}, \frac{\tau}{2}\right]$

$$\mathbb{P}(\Phi \leq \phi) = \mathbb{P}\Big(\Phi \leq \frac{\tau}{4}\Big) + \mathbb{P}\Big(\Gamma + \frac{\tau}{2} \leq \phi \mid \mathcal{W}_2\Big)\,\mathbb{P}(\mathcal{W}_2) \tag{A.118}$$

$$\mathbb{P}(\Phi \leq \phi) = \frac{1}{4} + \mathbb{P}\Big(\Gamma \leq \phi - \frac{\tau}{2} \mid \mathcal{W}_2\Big)\,\frac{1}{4} \tag{A.119}$$

$$\mathbb{P}(\Phi \leq \phi) = \frac{1}{4} + \frac{1}{4}\Big(2\mathbb{P}\Big(\Gamma \leq \phi - \frac{\tau}{2}\Big)\Big) \tag{A.120}$$

$$\mathbb{P}(\Phi \leq \phi) = \frac{1}{4} + \frac{1}{4}\Big(\frac{4\phi}{\tau} - 1\Big) \tag{A.121}$$

$$\mathbb{P}(\Phi \leq \phi) = \frac{\phi}{\tau} \tag{A.122}$$

From Equations (A.117) and (A.122) we have :

$$\forall \phi \in \Big[\frac{\tau}{4}, \frac{\tau}{2}\Big], \mathbb{P}(\Phi \leq \phi) = \frac{\phi}{\tau} \tag{A.123}$$

Case, $W_1' < 0$ **and** $W_2' < 0$

In that case we have :

$$\Phi = \arctan\Big(\frac{W_1'}{W_2'}\Big) + \frac{\tau}{2} \tag{A.124}$$

Let $\mathcal{W}_3$ be the proposition $W_1' < 0, W_2' < 0$. Such restrictions on W_1' and W_2' implies restrictions on Φ :

$$\mathcal{W}_3 \iff \Phi \in \Big[\frac{\tau}{2}, \frac{3\tau}{4}\Big] \tag{A.125}$$

And for $\phi \in \left[\frac{\tau}{2}, \frac{3\tau}{4}\right]$

$$\mathbb{P}(\Phi \leq \phi) = \mathbb{P}\Big(\Phi \leq \frac{\tau}{2}\Big) + \mathbb{P}\Big(\Gamma + \frac{\tau}{2} \leq \phi \mid \mathcal{W}_3\Big)\,\mathbb{P}(\mathcal{W}_3) \tag{A.126}$$

$$\mathbb{P}(\Phi \leq \phi) = \frac{1}{2} + \mathbb{P}\Big(\Gamma \leq \phi - \frac{\tau}{2} \mid \mathcal{W}_3\Big)\,\frac{1}{4} \tag{A.127}$$

$$\mathbb{P}(\Phi \leq \phi) = \frac{1}{2} + \frac{1}{4}\Big(2\mathbb{P}\Big(0 \leq \Gamma \leq \phi - \frac{\tau}{2}\Big)\Big) \tag{A.128}$$

$$\mathbb{P}(\Phi \leq \phi) = \frac{1}{2} + \frac{1}{2}\Big(\mathbb{P}\Big(\Gamma \leq \phi - \frac{\tau}{2}\Big) - \mathbb{P}(\Gamma \leq 0)\Big) \tag{A.129}$$

$$\mathbb{P}(\Phi \leq \phi) = \frac{1}{2} + \frac{1}{2}\Big(\frac{2\phi}{\tau} - 1\Big) \tag{A.130}$$

$$\mathbb{P}(\Phi \leq \phi) = \frac{\phi}{\tau} \tag{A.131}$$

From Equations (A.125) and (A.131) we have :

$$\forall \phi \in \left[\frac{\tau}{2}, \frac{3\tau}{4}\right], \mathbb{P}(\Phi \leq \phi) = \frac{\phi}{\tau} \tag{A.132}$$

Case, $W_1' < 0$ **and** $W_2' > 0$

In that case we have :

$$\Phi = \arctan\left(\frac{W_1'}{W_2'}\right) + \tau \tag{A.133}$$

Let $\mathcal{W}_4$ be the proposition $W_1' < 0, W_2' > 0$. Such restrictions on W_1' and W_2' implies restrictions on Φ :

$$\mathcal{W}_4 \iff \Phi \in \left[\frac{3\tau}{4}, \tau\right] \tag{A.134}$$

And for $\phi \in \left[\frac{3\tau}{4}, \tau\right]$

$$\mathbb{P}(\Phi \leq \phi) = \mathbb{P}\left(\Phi \leq \frac{3\tau}{4}\right) + \mathbb{P}(\Gamma + \tau \leq \phi \mid \mathcal{W}_4)\,\mathbb{P}(\mathcal{W}_4) \tag{A.135}$$

$$\mathbb{P}(\Phi \leq \phi) = \frac{3}{4} + \mathbb{P}(\Gamma \leq \phi - \tau \mid \mathcal{W}_4)\,\frac{1}{4} \tag{A.136}$$

$$\mathbb{P}(\Phi \leq \phi) = \frac{3}{4} + \frac{1}{4}(2\mathbb{P}(\Gamma \leq \phi - \tau)) \tag{A.137}$$

$$\mathbb{P}(\Phi \leq \phi) = \frac{3}{4} + \frac{1}{4}\left(\frac{4\phi}{\tau} - 3\right) \tag{A.138}$$

$$\mathbb{P}(\Phi \leq \phi) = \frac{\phi}{\tau} \tag{A.139}$$

From Equations (A.134) and (A.139) we have :

$$\forall \phi \in \left[\frac{3\tau}{4}, \tau\right], \mathbb{P}(\Phi \leq \phi) = \frac{\phi}{\tau} \tag{A.140}$$

Finally we proved that :

$$\forall \phi \in [0, \tau], \mathbb{P}(\Phi \leq \phi) = \frac{\phi}{\tau} \tag{A.141}$$

Thus the cumulative distribution function of Φ is :

$$F_{\Phi}(\phi) = \frac{\phi}{\tau} \tag{A.142}$$

$$\tag{A.143}$$

and the probability density function is :

$$f_{\Phi}(\phi) = \frac{1}{\tau} \tag{A.144}$$

and Φ is uniformly distributed in $[0, \tau]$

$$\Phi \sim \mathcal{U}(0, \tau) \tag{A.145}$$

Proving Theorem 3

□

A.3 Unconstrained angular edge loss

Developing equation (6.14) :

$$
\begin{aligned}
& R\sin\psi = w_0\sqrt{1+\left(\frac{\lambda\left(R\cos\psi - R_{w_0}\right)}{\pi w_0^2}\right)^2} \\
\iff & R^2\sin^2\psi = w_0^2 + \frac{\lambda^2\left(R\cos\psi - R_{w_0}\right)^2}{\pi^2 w_0^2} \\
\iff & R^2\left(1-\cos^2\psi\right) = w_0^2 + \frac{\lambda^2}{\pi^2 w_0^2}\left(R^2\cos^2\psi - 2R_{w_0}R\cos\psi + R_{w_0}^2\right) \\
\iff & \left(1+\frac{\lambda^2}{\pi^2 w_0^2}\right)R^2\cos^2\psi - 2\frac{\lambda^2 R_{w_0}R}{\pi^2 w_0^2}\cos\psi - R^2 + w_0^2 + \frac{\lambda^2 R_{w_0}^2}{\pi^2 w_0^2} = 0
\end{aligned}
$$

Let :

$$K = \frac{\lambda}{\pi w_0}$$

Let δ be the reduced discriminant of the polynomial in $\cos\psi$, then :

$$\delta = K^4 R^2 R_{w_0}^2 - \left(1+K^2\right)R^2\left(-R^2 + w_0^2 + K^2 R_{w_0}^2\right)$$

and finally :

$$\cos\psi = \frac{K^2 R_{w_0} \pm \sqrt{K^4 R_{w_0}^2 + (1+K^2)\left(R^2 - {w_0}^2 - K^2 R_{w_0}^2\right)}}{(1+K^2)R}$$

We must now discuss which polynomial solution must be chosen. Since we are in a paraxial approximation we must have :

$$\lambda \ll w_0 \tag{A.146}$$

From Equation (A.146) we deduce :

$$K \ll 1 \tag{A.147}$$

For TLS devices the minimal beam radius will be in the order of millimeters and the targets to be studied will be at least a few meters from the laser exit, it follows that :

$$ {w_0}^2 \ll R^2 \tag{A.148} $$

We also know that, for TLS devices, the laser focus distance R_{w_0} will be, at most, one order of magnitude higher than the distance to the targets, therefore :

$$ K^2 R_{w_0}^2 \ll R^2 \tag{A.149} $$

From Equations (A.147), (A.148) and (A.149) we have :

$$ \left(1 + K^2\right) \left(R^2 - {w_0}^2 - K^2 R_{w_0}^2\right) > 0 \tag{A.150} $$

Equation (A.150) implies :

$$ \sqrt{K^4 R_{w_0}^2 + \left(1 + K^2\right) \left(R^2 - {w_0}^2 - K^2 R_{w_0}^2\right)} > K^2 R_{w_0} \tag{A.151} $$

From Equation (A.151) and since we must have $0 \leq \psi \leq \frac{\tau}{4}$ (i.e. $\cos\psi \geq 0$) we conclude that :

$$ \cos\psi = \frac{K^2 R_{w_0} + \sqrt{K^4 R_{w_0}^2 + \left(1 + K^2\right) \left(R^2 - {w_0}^2 - K^2 R_{w_0}^2\right)}}{\left(1 + K^2\right) R} $$

Appendix B

Communications

We present here the extended abstracts of the different communications of that work

B.1 2016 IEEE International Conference on Functional-Structural Plant Growth Modeling, Simulation, Visualization and Applications (FSPMA 2016, Qingdao, China)

A point-cloud classification method to assess biases in tLiDAR-based forest canopy gap fraction estimates

Romain Rombourg[1,2], *Eric Casella*[2], *Franck Hétroy-Wheeler*[1] *and Helen Mckay*[2]

[1] Université Grenoble Alpes and Inria, Laboratoire Jean Kuntzmann, Montbonnot-Saint-Martin, 38330, France

[2] Forest Research, Centre for Sustainable Forestry and Climate Change, Farnham, GU10 4LH, UK

Corresponding author: romain.rombourg@gmail.com

New ground-based monitoring techniques are required for reporting of forest carbon stocks and fluxes at largest spatial and temporal scales. Terrestrial laser (TLS) scanning technologies have recently been tested in several forest inventories and were reported as alternative tools to rapidly provide more accurate and more detailed biometrics parameters and structural characteristics of vegetation than traditional methods. More than stem forms, tree heights and crown volumes; estimates for e.g., total above-ground volumes, branching patterns and the characteristics of

the leaf area display in space have been reported for isolated plants and forest canopies from TLS readings. Nevertheless, TLS are also subject to measurement uncertainties taking place at the range-finder step-process during a point-cloud acquisition. Scans and TLS characteristics, spatial heterogeneity in the geometrical and physical properties of vegetation and environmental factors all contribute to signal-to-noise and ranging artifacts observed in TLS point-cloud data, which influence the resolving power of the techniques in providing relevant information to forest managers. This study considers the development of point classification and correction algorithms tuned to TLS vegetation assessment in forest environments to address limits in the single return phase-shift laser technology. Our development activities were based on raw TLS data. Sky points (occurring wherever the laser beam is not reflected) and mixed points (occurring at spatial discontinuities wherever the laser beam footprint lies partially on more than one component) were classified after computing depth and intensity images from a point-cloud. The recorded range (depth) and its returning intensity value were then allocated to the pixel underlying the path of the fired laser beam. High variance found in the depth image was used to detect isolated sky points. An intensity threshold was then computed according to their intensity value. All points in the intensity image under this threshold were then classified as sky points and filtered. A point was classified as a mixed point from the depth image by computing the angles between the laser beam direction and the normal to the triangles formed by the point and its neighbors, if more than half on these angles are above a given threshold the point is labeled as a mixed point. In order to correct the location of the detected mixed points, we proved that their position is driven by a small set of equations. For each mixed point, we used the distances from the TLS to the components hit, the intensity of the neighboring points and our mixed point model to compute which component intercepted most of the laser beam at this point, and move it on this component. Any uncorrected mixed point is filtered at the end of the procedure. Algorithms were developed from data collected under controlled conditions (i.e., considering scans and TLS characteristics and the spatial complexity of vegetation) and assessed against TLS readings recorded in forest environments. Overall, we were able to detect all the noise in the point-cloud with a limited number of wrong detection. First results show that the model may allow us to correct up to 80% of the mixed point, significantly increasing the point cloud quality.

B.2 2016 IEEE International Conference on Functional-Structural Plant Growth Modeling, Simulation, Visualization and Applications (2016, Qingdao, China)

A comprehensive sensitivity analysis of forest tree mock-up reconstruction methods from phase-shift based tLiDAR point-cloud data

Eric Casella[1], *Pasi Raumonen*[2], *Romain Rombourg*[1,3], *Franck Hétroy-Wheeler*[3], *Helen McKay*[1]

[1] Forest Research, Centre for Sustainable Forestry and Climate Change, Farnham, GU10 4LH, UK

[2] Department of Mathematics, Tampere University of Technology, P.O. Box 553, Tampere 33101, Finland

[3] Université Grenoble Alpes and Inria, Laboratoire Jean Kuntzmann, Montbonnot-Saint-Martin, 38330, France

Corresponding author: eric.casella@forestresearch.gov.uk

New ground-based monitoring techniques are required for reporting of forest carbon stocks and fluxes at largest spatial and temporal scales. Terrestrial laser scanning (TLS) technologies have recently been tested in several forest inventories to provide tree mock-ups from recorded point-cloud data (see e.g., Raumonen et al., 2015). For this purpose, geometrical reconstruction methods have been proposed and reported results have shown that TLS technologies can overcome limitations from traditional methods in estimating biometric parameters, standing biomasses and the structural characteristics of vegetation (see e.g., Casella et al., 2013). Nevertheless, the quality of the post-processing routines used to filter noise and ranging artefacts, generally reported in point-cloud data, may influence the resolving power of these reconstruction methods.

This study considers a comprehensive analysis of the effects of vegetation, scans and TLS characteristics, point-cloud filtering techniques and model parameterisation on the quality of the reconstructed mock-ups from point-cloud data.

Our analysis was based on raw point-clouds recorded by a single-return phase-shift Leica HDS-6100 TLS on four 80-year-old temperate deciduous tree species (Birch, Hornbeam, Larch and Oak). Scans were performed during winter-time in dried and low wind speed (less than 1 m s-1) conditions. Three trees were recorded per spp. from six scan positions around each tree and with three TLS sampling resolution levels (0.018-0.072) at each scan position. Trees were then harvested and their

dry mass was measured. An empirical function describing the vertical profile in over-bark wood density was described from each single tree. Point-clouds were filtered using both a commercial and an alternative filtering method developed for this study (see Rombourg et al., 2016) before point-cloud co-registrations were applied. Tree mock-ups were then computed by the method described in Raumonen et al. (2013) and Raumonen et al. (2015) and standing biomasses estimated.

Filtering options provided by the commercial software were sub-optimal, yielding overestimations in biomass estimates (up to 2 fold) for coarse and fine branches (diameters less than 7 cm). The number of scan positions, the TLS sampling resolution and the tested model parameters all influenced the quality of the reconstructed mock-ups. After applying our filtering method to the point-clouds, neither the TLS sampling resolution, nor the model parameters have any influence on the quality of the reconstructed mock-ups. Biomass estimates were generally underestimated, but gradually reached less than 5% difference to actual values with increasing the number of TLS positions around the trees. The quality of the resulting tree mock-ups was finally assessed throughout the hemispherical photography technique using the method of Casella et al. (2013).

Casella, E. et al. (2013). tLiDAR methodologies can overcome limitations in estimating forest canopy LAI from conventional hemispherical photograph analyses. 7th International Conference on FSPM, Saariselk, Finland.

Raumonen, P. et al. (2013) Fast automatic precision tree models from terrestrial laser scanner data. Remote Sens. 5, 491520.

Raumonen, P. et al. (2015) Massive-scale tree modelling from TLS data. ISPRS Annals of the Photogrammetry, Remote Sensing and Spatial Information Sciences, Volume II-3/W4, 2015.

Rombourg, R. et al. (2016) A point-cloud classification method to assess biases in tLiDAR-based forest canopy gap fraction estimates. 1st International conference on FSPMA, Qingdao, China

B.3 6^{ieme} édition de l'atelier T-LiDAR pour la communauté francophone (2016, Avignon, France)

Une suite de méthodes de détection de bruit pour les scanners laser à modulation damplitude

Romain Rombourg[1,2], *Eric Casella*[2] *and Franck Hétroy-Wheeler*[1]

[1] Université Grenoble Alpes and Inria, Laboratoire Jean Kuntzmann, Montbonnot-Saint-Martin, 38330, France

[2] Forest Research, Centre for Sustainable Forestry and Climate Change, Farnham, GU10 4LH, UK

Corresponding author: romain.rombourg@gmail.com

De nouvelles méthodes sont requises pour estimer les flux et stocks de carbone à de plus grandes échelles. Les scanners laser terrestres (TLS), testés sur plusieurs inventaires forestiers, ont montré quils étaient capables de fournir rapidement des paramètres biométriques et structurels de la végétation de manière plus précise que les méthodes traditionnelles. Cependant, ces scanners sont sujets à de nombreuses sources derreurs dues à lintéraction entre le processus dacquisition et les hétérogénéités physiques et spatiales de la végétation. Ces facteurs créent des artefacts dans la mesure de distance, entravant les méthodes mentionnées précédemment. Cette étude se focalise sur le développent dalgorithmes de classification adaptés aux scènes forestières acquises via un scanner laser à modulation damplitude. Notre développement sest basé sur les scans bruts. Les points de "ciel" (pas de retour laser) et les points "mixtes" (tir laser intercepté par plusieurs objets) ont été classifiés à partir dimages de profondeur et dintensité obtenues à partir dun scan. Dans ces images, la position dun pixel représente la direction de tir du laser et sa valeur la profondeur ou intensité. Les pixels présentant les plus hautes variances locales dans limage de profondeur permettent disoler un échantillon de points de ciel. Ces points permettent de calculer un seuil dintensité. Tous les points sous ce seuil sont marqués comme points de ciel et filtrés. Un point est classifié comme point mixte en calculant les angles entre la direction du tir laser et les normales aux triangles formés par ce point et ses voisins dans limage de profondeur. Si plus de la moitié des angles calculés sont au dessus dun seuil donné, le point est marqué comme mixte. Les algorithmes ont été développés, testés et évalués sur des scans forestiers et sur des scans en conditions contrlées (définies en considérant les propriétés physiques et spatiales des environnements forestiers). Nous avons été capable de détecter tout le bruit dans la majorité des cas avec

une nombre limité de fausses détections. Ce travail sera suivi par le développement dune méthode de correction des points mixtes basée sur un modèle mathématique du phénomène.

B.4 3D Tree Models For Forest Dynamics meeting (2020, Helsinki, Finland)

Sensitivity analysis of an automated processing chain and uncertainty in the prediction of tree above ground biomass from TLS data

Eric Casella[1], *Romain Rombourg*[1,2], *Pasi Raumonen*[3], *Franck Hétroy-Wheeler*[4] *and Markku Åkerblom*[3]

[1] Forest Research, Centre for Sustainable Forestry and Climate Change, Farnham, GU10 4LH, UK

[2] Université Grenoble Alpes and Inria, Laboratoire Jean Kuntzmann, Montbonnot-Saint-Martin, 38330, France

[3] Mathematics, Tampere University, Korkeakoulunkatu 10, 33720 Tampere, Finland

[4] Department of Computer Science, University of Strasbourg, 67081, France

Corresponding author: eric.casella@forestresearch.gov.uk

The above ground volume (AGV) measurement of a sampled tree is a fundamental input to provide predictions of forest, woodland and urban resources, but it is generally biased by country-specific merchantable thresholds. Terrestrial laser scanners (TLS) have been demonstrated to be promising for non-destructive and accurate measurements. Actually, there have been recent procedural approaches to develop automated processing chains for extracting tree metrics from TLS data. A sensitivity analysis of an automated chain on 12 parameters is presented here to report effects of TLS and scan acquisition characteristics and routines used for data filtering and volume estimates on AGBiomass predictions. This analysis was based on data recorded by a Leica HDS-6100 on Oak, Hornbeam, Birch and Larch during winters 2014-16. Three trees were recorded per *spp.* from six scan positions around each tree and with three TLS sampling resolutions (0.072-0.018°) per position. Scanned trees were felled, then measured in detail and stratified into lower stem (Ls), coarse (Cb, diameter ge 7 cm) and small (Sb, lt 7 cm) branch sections. When compared against ground data, this analysis indicated a consistent pattern across all trees for DBH ($r^2 = 0.98$, $bias < 0.001m$), tree height ($r^2 = 0.89$, $bias > -0.63m$) or AGBs ($r^2 = 0.98$, $bias < 4$; $r^2 = 0.99$, $bias > -34$; $r^2 = 0.96$, $bias < 8kg$ for Ls, Cb and Sb, respectively) with a TLS resolution of 0.018° driving improved fits for h (+5%), AGB_{Cb} (+13%) and AGB_{Sb} (+27%) and 6 scan positions driving improved fits for AGB_{Cb} (+56%) and AGB_{Sb} (+36%). The

quality of the filter routine was found to be the most critical parameter (up-to ±65% for Sb). All other parameters had a relatively little effect.

B.5 Video communication

Forest Research, Tampere University of Technology and Université Grenoble Alpes have been working together to optimize measurements from forest sample plots using terrestrial LiDAR in order to produce more accurate, more detailed, timely and harmonised information that can be fed into national and international forest information systems. This animation shows details of our data processing chain for tree volume and biomass assessments. See the video at :

https://www.youtube.com/watch?v=jjtVhjx8-3Q